Gasoil

Biofuel from hydrocracking of *Cerbera manghas* oil over Ni-Zn/HZSM-5 catalyst

Photocatalyst

Photoperoxidation of ciprofloxacin antibiotic in aqueous medium using $Fe_{3-x}O_{4-y}$-TiO_2 particles as catalysty

Optoelectronic

Theoretically studying the optoelectronic properties of oligomers based on 2.7-divinyl-cabazole

Mechanochemistry

Screening of coformers for quercetin cocrystals through mechanochemical methods

unesp

UNIVERSIDADE ESTADUAL PAULISTA

Reitor

Pasqual Barretti

Vice-Reitora

Maysa Furlan

Pró-Reitora de Graduação

Celia Maria Giacheti

Pró-Reitora de Pós-Graduação

Maria Valnice Boldrin

Pró-Reitor de Pesquisa

Edson Cocchieri Botelho

Pró-Reitor de Extensão Universitária e Cultura

Raul Borges Guimarães

Pró-Reitor de Planejamento Estratégico e Gestão

Estevão Tomomitsu Kimpara

INSTITUTO DE QUÍMICA

Diretor

Sidney José Lima Ribeiro

Vice-Diretora

Denise Bevilaqua

Editorial Team

EDITORIAL PRODUCTION

Editorial

The Editor of Eclética Química Journal, Editorial Board and Staff proudly announce the first issue of vol. 47 of 2022 in the hope that we can all live a milder year in terms of pandemic which should allow us to dedicate even more intensely to scientific research. Opens the issue a study describing the effect of temperature on the relative hydrocarbon concentrations in the biofuel obtained from hydrocracking of *Cerbera manghas* oil using Ni-Zn/HZSM-5 as catalyst. The main properties of the catalysts were investigated, and the hydrocracking process was conducted in a pressure batch reactor. The predominant products in the biofuel were pentadecane and heptadecane with different proportions depending on the reaction temperature. Thus, the gasoil produced from *Cerbera manghas* oil could be an alternative promising transportation fuel. Follows, a theoretical study of the electronic and optical properties of PCrV oligomers, since the best compound can be chosen among different ones objecting to increase the efficiency of the organic photovoltaic cell. Different R radicals were added to derivatives of 2.7-divynil-carbazole to reduce the HOMO-LUMO gap energy and the calculations allowed to suggest the PCrV-BiTTP, PCrV-TTP, PCrV-TTN molecules as good candidates for applications in organic solar cells. It is well known that conventional treatments are generally not effective for removing micropollutants as antibiotics and other classes of drugs present in wastewater. In the next paper, the degradation of the ciprofloxacin antimicrobial in aqueous solution is described applying degradation advanced processes such as direct photocatalysis and photoperoxidation using $Fe_{3-x}O_{4-y}$-TiO_2 particles as catalyst. The readers can find details about catalyst preparation and characterization, and kinetics of the micropollutant degradation process with greater degradation percentages. Some nutraceutical compound may exhibit many pharmacological properties, but its efficacy is limited due to low solubility, for instance, quercetin. So, a possible way to improve the solubility is the cocrystallization screening using different cocrystal formers as described in the last article of this issue. Mechanochemical method afforded cocrystals of quercetin with picolinamide and isonicotinamide while benzamide and pyrazinoic acid gave physical mixtures with quercetin.

The Editor and members of Editorial Board of Eclética Química Journal want to pay a tribute to the effort developed by Authors and Reviewers during the last year and we hope and trust that in the 2022nd year the mutual collaboration will lead to everyone's progress.

Assis Vicente Benedetti
Editor-in-Chief of EQJ

Citation databases: Ecletica Quim. J. is indexed

SciFinder
A **CAS** SOLUTION

Scopus

DOAJ DIRECTORY OF
OPEN ACCESS
JOURNALS

evisa.

Google
Scholar

REDIB

redalyc
LA HEMEROTECA CIENTÍFICA EN LÍNEA

latindex

EBSCO
Discovery Service

biblat
Bibliografía Latinoamericana
en revistas de investigación científica y social

IAEA | INIS

International
Nuclear
Information
System

*Click on the images to follow the links.
EBSCO has no link available. The address is for subscribers only.

INSTRUCTIONS FOR AUTHORS

BEFORE YOU SUBMIT

1. Check Eclet. Quim. J.'s focus and scope

Eclética Química Journal is a peer-reviewed quarterly publication of the Institute of Chemistry of São Paulo State University (UNESP). It publishes original researches as articles, reviews and short reviews in **all areas of Chemistry**.

2. Types of papers

    a. Original articles
    b. Reviews
    c. Short reviews
    d. Communications
    e. Technical notes
    f. Articles in education in chemistry and chemistry-related areas

Manuscripts submitted for publication as full articles and communications must contain original and unpublished results and should not have been submitted elsewhere either partially or whole.

a. Original articles

The manuscript must be organized in sections as follows:

1. Introduction
2. Experimental
3. Results and Discussion
4. Conclusions
References

Sections titles must be written in bold and sequentially numbered; only the first letter should be in uppercase letter. Subsections, numbered as exemplified, should be written in normal and italic letters; only the first letter should be in uppercase letter.

Example:

1. Introduction
1.1 History

2. Experimental
2.1 Surface characterization
2.1.1 Morphological analysis

b. Reviews

Review articles should be original and present state-of-the-art overviews in a coherent and concise form covering the most relevant aspects of the topic that is being revised and indicate the likely future directions of the field. Therefore,

before beginning the preparation of a Review manuscript, send a letter (one page maximum) to the Editor with the subject of interest and the main topics that would be covered in the Review manuscript. The Editor will communicate his decision in two weeks. Receiving this type of manuscript does not imply acceptance to be published in **Eclet. Quím. J.** It will be peer-reviewed.

c. Short reviews

Short reviews should present an overview of the state-of-the-art in a specific topic within the scope of the Journal and limited to 5,000 words. Consider a table or image as corresponding to 100 words. Before beginning the preparation of a Short Review manuscript, send a letter (one page maximum) to the Editor with the subject of interest and the main topics that would be covered in the Short Review manuscript.

d. Communications

Communications should cover relevant scientific results and are limited to 1,500 words or three pages of the Journal, not including the title, authors' names, figures, tables and references. However, Communications suggesting fragmentation of complete contributions are strongly discouraged by Editors.

e. Technical notes

Descriptions of methods, techniques, equipment or accessories developed in the authors' laboratory, as long as they present chemical content of interest. They should follow the usual form of presentation, according to the peculiarities of each work. They should have a maximum of 25 pages, including figures, tables, diagrams, etc.

f. Articles in education in chemistry and chemistry-correlated areas

Research manuscript related to undergraduate teaching in Chemistry and innovative experiences in undergraduate and graduate education. They should have a maximum of 25 pages, including figures, tables, diagrams, and other elements.

3. Special issues

Special issues with complete articles dedicated to Symposia and Congresses and to special themes or in honor of scientists with relevant contributions in Chemistry and correlate areas can be published by **Eclet. Quim. J.** under the condition that a previous agreement with Editors is established. All the guides of the journal must be followed by the authors.

4. Approval

Ensure all authors have seen and approved the final version of the article prior to submission. All authors must also approve the journal you are submitting to.

ETHICAL GUIDELINES

Before starting the submission process, please be sure that **all ethical aspects mentioned below were followed**. Violation of these ethical aspects may preclude authors from submitting or publishing articles in **Eclet. Quim. J.**

  a. Coauthorship: The corresponding author is responsible for listing as coauthors only researchers who have really taken part in the work, for informing them about the entire manuscript content and for obtaining their permission to submit and publish it.

b. Nonauthors: Explicit permission of a nonauthor who has collaborated with personal communication or discussion to the manuscript being submitted to **Eclet. Quím. J.** must be obtained before being cited.

c. Unbiased research: Authors are responsible for carefully searching for all the scientific work relevant to their reasoning irrespective of whether they agree or not with the presented information.

d. Citation: Authors are responsible for correctly citing and crediting all data taken from other sources. This requirement is not necessary only when the information is a result of the research presented in the manuscript being submitted to **Eclet. Chem. J.**

e. Direct quotations: The word-for-word reproduction of data or sentences as long as placed between quotation marks and correctly cited is not considered ethical deviation when indispensable for the discussion of a specific set of data or a hypothesis.

f. Do not cite: Master's Degree dissertations and PhD theses are not accepted; instead, you must cite the publications resulted from them.

g. Plagiarism: Plagiarism, self-plagiarism, and the suggestion of novelty when the material was already published are unaccepted by **Eclet. Quim. J.** Before reviewing a manuscript, the **Turnitin antiplagiarism software** will be used to detect any ethical deviation.

h. Simultaneous submissions of the same manuscript to more than one journal is considered an ethical deviation and is conflicted to the declaration has been done below by the authors.

i. Studies with humans or other animals: Before submitting manuscripts involving human beings, materials from human or animals, the authors need to confirm that the procedures established, respectively, by the institutional committee on human experimentation and Helsinki's declaration, and the recommendations of the animal care institutional committee were followed. Editors may request complementary information on ethical aspects.

COPYRIGHT NOTICE

The corresponding author transfers the copyright of the submitted manuscript and all its versions to **Eclet. Quim. J.**, after having the consent of all authors, which ceases if the manuscript is rejected or withdrawn during the review process.

When a published manuscript in Eclet. Quim. J. is also published in other Journal, it will be immediately withdrawn from Eclet. Quim. J. and the authors informed of the Editor decision.

Self-archive to institutional, thematic repositories or personal webpage is permitted just after publication. The articles published by **Eclet. Quim. J.** are licensed under the **Creative Commons Attribution 4.0 International License**.

PUBLICATION CHARGES

Eclética Química Journal is supported by the Institute of Chemistry/UNESP and publication is free of charge for authors.

MANUSCRIPT PREPARATION

COVER LETTER

We provide a template to help you prepare your cover letter. To download it, click **here**.

The cover letter MUST include:

1. Identification of authors

    a. The authors' full names (they must be written in full and complete, separated by comma)

~~João M. José~~	Incorrect
~~J. M. José~~	Incorrect
João Maria José	Correct!

    b. E-mail addresses and affiliations (**neither more nor less than two instances**) of all authors;
    c. ORCID ID links;
    d. A plus sign (+) indicating the corresponding author.

Example:

Author Full Name[1+], Author Full Name[2]

1. University, Faculty or Institute, City, Country.
2. Company, Division or Sector or Laboratory, City, Country.

+ Author 1: address@mail.com, ORCID: https://orcid.org/xxxx-xxxx-xxxx-xxxx
Author 2: address@mail.com, ORCID: https://orcid.org/xxxx-xxxx-xxxx-xxxx

2. Authors' contribution

We request authors to include author contributions according to CRediT taxonomy standardized contribution descriptions. CRediT (Contributor Roles Taxonomy) is a high-level taxonomy, including 14 roles, that can be used to represent the roles typically played by contributors to scientific scholarly output. The roles describe each contributor's specific contribution to the scholarly output.

    a. Please, visit this link (https://casrai.org/credit/) to find out which role(s) the authors fit into;
    b. Do not modify the role names; do not write "all authors" in any role. Do not combine two or more roles in one line.
    c. If there are any roles that no author has engaged in (such as funding in papers that were not funded), write "Not applicable" in front of the name of the role;
    d. Write the authors' names according to the **American Chemistry Society (ACS) citation style**.

Example:

Conceptualization: Foster, J. C.; O'Reilly, R. K.
Data curation: Varlas, S.; Couturaud, B.; Coe, J.; O'Reilly, R. K.
Formal Analysis: Foster, J. C.; Varlas, S.
Funding acquisition: Not applicable.

Investigation: Foster, J. C.; O'Reilly, R. K.
Methodology: Coe, J.; O'Reilly, R. K.
Project administration: O'Reilly, R. K.
Resources: Coe, J.
Software: Not applicable.
Supervision: O'Reilly, R. K.
Validation: Varlas, S.; Couturaud, B.
Visualization: Foster, J. C.
Writing – original draft: Foster, J. C.; Varlas, S.; Couturaud, B.; Coe, J.; O'Reilly, R. K.
Writing – review & editing: Foster, J. C.; Varlas, S.; Couturaud, B.; Coe, J.; O'Reilly, R. K.

4. Indication of reviewers

We kindly ask the authors to suggest **five** suitable reviewers, providing full name, affiliation, and email.

5. Other information

a. The authors must write one paragraph remarking the novelty and relevance of the work;
b. The corresponding author must declare, on behalf of the other authors, that the manuscript being submitted is original and its content has not been published previously and is not under consideration for publication elsewhere;
c. The authors must inform if there is any conflict of interest.

6. Acknowledgements and funding

Acknowledgements and funding information will be requested after the article is accepted for publication.

7. Data availability statement

A data availability statement informs the reader where the data associated with your published work is available, and under what conditions they can be accessed. Therefore, authors must inform if:

Data will be available upon request;
All dataset were generated or analyzed in the current study; or
Data sharing is not applicable.

MANUSCRIPT

We provide a template to help you prepare your manuscript. To download it, click **here**.

1. General rules

Only manuscripts written in English will be accepted. British or American usage is acceptable, but they should not be mixed. Non-native English speakers are encouraged to have their manuscripts professionally revised before submission.

Manuscripts must be sent in editable files as *.doc, *.docx or *.odt. The text must be typed using font style Times New Roman and size 12. Space between lines should be 1.5 mm and paper size A4, top and bottom margins 2.5 cm, left and right margins 2.0 cm.

All contributions must include an **abstract** (170 words maximum), **three to five keywords** and a **graphical abstract** (8 cm wide × 8 cm high).

Supplementary information: all type of articles accepts supplementary information (SI) that aims at complementing the main text with material that, for any reason, cannot be included in the article.

TITLE

The title should be concise, explanatory and represent the content of the work. The title must have only the first letter of the sentence in uppercase. The following are not allowed: acronyms, abbreviations, geographical location of the research, en or em dashes (which must be replaced by a colon). Titles do not have full point.

ABSTRACT

Abstract is the summary of the article. The abstract must be written as a running text not as structured topics, but its content should present background, objectives, methods, results, and conclusion. It cannot contain citations. The text should be written in a single paragraph with a **maximum of 170 words**.

KEYWORDS

Keywords are intended to make it easier for readers to find the content of your text. As fundamental tools for database indexing, they act as a gateway to the text. The correct selection of keywords significantly increases the chances that a document will be found by researchers on the topic, and consequently helps to promote the visibility of an article within a myriad of publications.

FIGURES, TABLES AND EQUATIONS

Figures, tables and equations must be written with initial capital letter followed by their respective number and period, in bold, without adding zero "**Table 1**", preceding an explanatory title. Tables, Figures and Equations should appear after the first citation and should be numbered according to the ascending order of appearance in the text (1, 2, 3...).

Figures, tables, schemes and photographs already published by the same or different authors in other publications may be reproduced in manuscripts of **Eclet. Quim. J.** only with permission from the editor house that holds the copyright.

Nomenclature, abbreviations, and symbols should follow IUPAC recommendations.

DATA AVAILABILITY STATEMENT

The data availability statement informs the reader where the data associated with your work is available, and under what conditions they can be accessed. They also include links (where applicable) to the data set.

    a. The data are available in a data repository (cite repository and the DOI of the deposited data);
    b. The data will be available upon request;
    c. All data sets were generated or analyzed in the current study;
    d. Data sharing is not applicable (in cases where no data sets have been generated or analyzed during the current study, it should be declared).

GRAPHICAL ABSTRACT

The graphical abstract must summarize the manuscript in an interesting way to catch the attention of the readers. As already stated, it must be designed with 8 cm wide × 8 cm high, and a 900-dpi resolution is mandatory for this journal. It must be submitted as *.jpg, *.jpeg, *.tif or *.ppt files as supplementary file.

We provide a template to help you prepare your GA. To download it, click **here**.

SUPPLEMENTARY INFORMATION

When appropriate, important data to complement and a better comprehension of the article can be submitted as Supplementary File, which will be published online and will be made available as links in the original article. This might include additional figures, tables, text, equations, videos or other materials that are necessary to fully document the research contained in the paper or to facilitate the readers' ability to understand the work.

Supplementary material should be presented in appropriate .docx file for text, tables, figures and graphics. All supplementary figures, tables and videos should be referred in the manuscript body as "Table S1, S2…", "Fig. S1, S2…" and "Video S1, S2 …".

At the end of the main text the authors must inform: This article has supplementary information.

Supplementary information will be located following the article with a different DOI number from that of the article, but easily related to it.

CITATION STYLE GUIDE

From 2021 on, the **Eclet. Quim. J.** will follow the **ACS citation style**.

Indication of the sources is made by authorship and date. So, the reference list is organized alphabetically by author.

Each citation consists of two parts: the in-text citation, which provides brief identifying information within the text, and the reference list, a list of sources that provides full bibliographic information.

We encourage the citation of primary research over review articles, where appropriate, in order to give credit to those who first reported a finding. Find out more about our commitments to the principles of San Francisco Declaration on Research Assessment (DORA).

What information you must cite?

   a. Exact wording taken from any source, including freely available websites;
   b. Paraphrases of passages;
   c. Summaries of another person's work;
   d. Indebtedness to another person for an idea;
   e. Use of another researchers' work;
   f. Use of your own previous work.

You do not need to cite **common knowledge**.

Example:

Water is a tasteless and odorless liquid at room temperature (common knowledge, no citation needed)

In-text citations

You can choose the cite your references within or at the end of the phrase, as showed below.

Within the cited information:

One author: Finnegan states that the primary structure of this enzyme has also been determined (2004).
Two authors: Finnegan and Roman state that the structure of this enzyme has also been determined (2004).
Three or more authors: Finnegan et al. state that the structure of this enzyme has also been determined (2004).

At the end of the cited information:

One author: The primary structure of this enzyme has also been determined (Finnegan, 2004).
Two authors: The primary structure of this enzyme has also been determined (Finnegan and Roman, 2004).
Three or more authors: The primary structure of this enzyme has also been determined (Finnegan et al., 2004).

If you need to cite more than one reference in the same brackets, separate them with semicolon and write them in alphabetic order:

The primary structure of this enzyme was determined (Abel et al., 2011; Borges, 2004; Castro et al., 2021).

Bibliographic references

Article from scientific journals
Foster, J. C.; Varlas, S.; Couturaud, B.; Coe, J.; O'Reilly, R. K. Getting into Shape: Reflections on a New Generation of Cylindrical Nanostructures' Self-Assembly Using Polymer Building Block. *J. Am. Chem. Soc*. **2019**, *141* (7), 2742−2753. https://doi/10.1021/jacs.8b08648

Book
Hammond, C. *The Basics of Crystallography and Diffraction*, 4th ed.; International Union of Crystallography Texts on Crystallography, Vol. 21; Oxford University Press, 2015.

Book chapter
Hammond, C. Crystal Symmetry. In *The Basics of Crystallography and Diffraction*, 4th ed.; International Union of Crystallography Texts on Crystallography, Vol. 21; Oxford University Press, 2015; pp 99−134.

Book with editors
Mom the Chemistry Professor: Personal Accounts and Advice from Chemistry Professors Who Are Mothers, 2nd ed.; Woznack, K., Charlebois, A., Cole, R. S., Marzabadi, C. H., Webster, G., Eds.; Springer, 2018.

Website
ACS Publications Home Page. https://pubs.acs.org/ (accessed 2019-02-21).

Document from a website
American Chemical Society, Committee on Chemical Safety, Task Force for Safety Education Guidelines. *Guidelines for Chemical Laboratory Safety in Academic Institutions*. American Chemical Society, 2016. https://www.acs.org/content/dam/acsorg/about/governance/committees/chemicalsafety/publications/acs-safety-guidelines-academic.pdf (accessed 2019-02-21).

Conference proceedings
Nilsson, A.; Petersson, F.; Persson, H. W.; Jönsson, H. Manipulation of Suspended Particles in a Laminar Flow. In Micro Total Analysis Systems 2002, Proceedings of the µTAS 2002 Symposium, Nara, Japan, November 3−7, 2002; The Netherlands, 2002; pp 751−753. https://doi.org/10.1007/978-94-010-0504-3_50

Governmental and legislation information
Department of Commerce, United States Patent and Trademark Office. Section 706.02 Rejection of Prior Art [R-

07.2015]. *Manual of Patent Examining Procedure (MPEP)*, 9th ed., rev. 08.2017, last revised January 2018. https://www.uspto.gov/web/offices/pac/mpep/s706.html#d0e58220 (accessed 2019-03-20).

Patent
Lois-Caballe, C.; Baltimore, D.; Qin, X.-F. Method for Expression of Small RNA Molecules within a Cell. US 7 732 193 B2, 2010.

Streaming data
American Chemical Society. Game of Thrones Science: Sword Making and Valyrian Steel. *Reactions*. YouTube, April 15, 2015. https://www.youtube.com/watch?v=cHRcGoje4j4 (accessed 2019-02-28).

For more information, you can access the ACS Style Quick Guide and the Williams College LibGuides.

SUBMITTING YOUR MANUSCRIPT

The corresponding author should submit the manuscript online by clicking **here**. If you are a user, register by clicking **here**.

At the **User home** page, click in **New submission**.

In Step 1, select a section for your manuscript, verify one more time if you followed all these rules in **Submission checklist**, add Comments for the Editor if you want to, and click Save and continue.

In Step 2, you will **upload your manuscript**. Remember it will pass through a double-blind review process. So, do not provide any information on the authorship.

In Step 3, enter **submission's metadata**: authors' full names, valid e-mail addresses and ORCID ID links (with "http" not "https"). Add title, abstract, contributors and supporting agencies, and the list of references.

In Step 4, upload the **cover letter**, the **graphical abstract** and other **supplementary material** you want to include in your manuscript.

In Step 5, you will be able to check all submitted documents in the **File summary**. If you are certain that you have followed all the rules until here, click in **Finish submission**.

REVIEW PROCESS

The time elapsed between the submission and the first response of the reviewers is around three months. The average time elapsed between submission and publication is around seven months.

Resubmission (manuscripts "rejected in the present form" or subjected to "revision") must contain a letter with the responses to the comments/criticism and suggestions of reviewers/editors should accompany the revised manuscript. All modifications made to the original manuscript must be highlighted.

If you want to check our Editorial process, click **here**.

EDITOR'S REQUIREMENTS

Authors who have a manuscript accepted in **Eclet. Quim. J.** may be invited to act as reviewers.

Only the authors are responsible for the correctness of all information, data and content of the manuscript submitted to **Eclet. Quim. J.** Thus, the Editors and the Editorial Board cannot accept responsibility for the correctness of the material published in **Eclet. Quim. J.**

Proofs
After accepting the manuscript, **Eclet. Quim. J.** technical assistants will contact you regarding your manuscript page proofs to correct printing errors only, i.e., other corrections or content improvement are not permitted. The proofs shall be returned in three working days (72 h) via email.

Appeal
Authors may only appeal once about the decision regarding a manuscript. To appeal against the Editorial decision on your manuscript, the corresponding author can send a rebuttal letter to the editor, including a detailed response to any comments made by the reviewers/editor. The editor will consider the rebuttal letter, and if dimmed appropriate, the manuscript will be sent to a new reviewer. The Editor decision is final.

Contact

If you have any question, please contact our team:

Prof. Assis Vicente Benedetti
Editor-in-Chief
ecletica@journal.iq.unesp.br

Letícia Amanda Miguel and Jéssica Odoni
Technical support
ecletica@ctrlk.com.br

SUMMARY

ORIGINAL ARTICLES

Eclética Química Journal

Biofuel from hydrocracking of *Cerbera manghas* oil over Ni-Zn/HZSM-5 catalyst

Lenny Marlinda[1+] , Danawati Hari Prajitno[2] , Achmad Roesyadi[2] , Ignatius Gunardi[2] , Yustia Wulandari Mirzayanti[3] , Muhammad Al Muttaqii[4] , Agus Budianto[3]

1. University of Jambi, Department of Chemistry, Jambi, Indonesia.
2. Sepuluh Nopember Institute of Technology, Department of Chemical Engineering, Surabaya, Indonesia.
3. Adhi Tama Institute of Technology, Department of Chemical Engineering, Surabaya, Indonesia.
4. Indonesian Institute of Sciences, Research Center for Chemistry, Tangerang Selatan, Indonesia.

+Corresponding author: Lenny Marlinda, Phone: +62 81366079067, Email address: marlindalenny@unja.ac.id

ABSTRACT: The effects of reaction temperature on the hydrocarbon composition of biofuel produced in hydrocracking of *Cerbera manghas* oil with Ni-Zn/HZSM-5 catalyst were investigated. The incipient wetness impregnation method was applied to prepare the Ni-Zn/HZSM-5 catalysts. Furthermore, the properties of catalysts were measured by X-ray diffraction, atomic absorption spectrometry, and nitrogen physisorption. Hydrocracking process was carried out in Parr USA pressure batch reactor at pressure of 20 ± 5 bar after flowing H_2 for 1 h. The reaction with a catalyst/oil ratio of 1 g/150 mL proceeded at various temperatures of 350, 375 and 400 °C for 2 h. Gas chromatography-mass spectrometry was used to analyze biofuel. The most abundant hydrocarbon compounds in biofuel were identified as pentadecane and heptadecane (a major diesel fuel compound) with a different amount at different reaction temperatures. It can be said that the hydrodecarboxylation/decarbonylation routes were the predominant reaction pathways and oxygen removal occurred during hydrocracking. The *Cerbera manghas* oil can be recommended as a promising biofeed to produce the gasoil as an alternative transportation fuel.
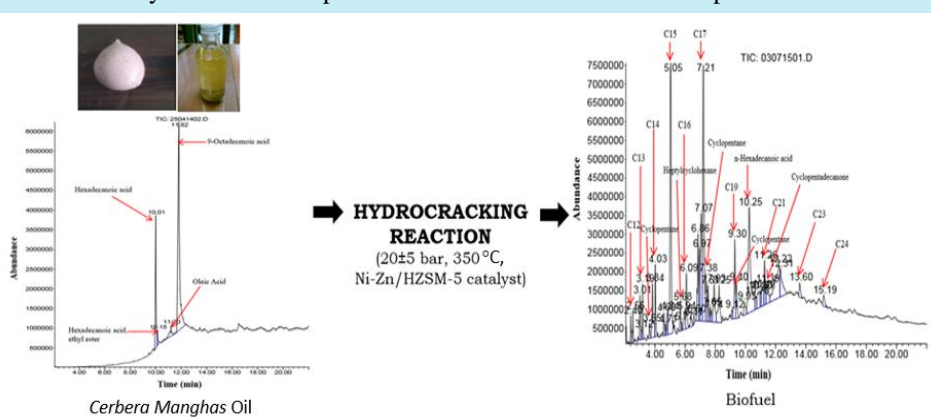
1. Introduction

When liquid fuel from fossil sources was applied as transportation fuel, the increasing CO_2 emission rapidly increased. The use of biofuel will be the right step to achieve zero waste. Hydrocarbon compounds in biofuel are similar with petroleum diesel fuel so that biofuel can be a substitute for diesel fuel. Development of biofuel production technology continues to evolve concurrently with the exploration of vegetable oil as raw materials while maintaining the sustainability of food security. Biofuel was already used both in pure form and blending is fatty acid methyl esters (FAMEs), also known as oxygenated biofuels, as reported by Romero et al. (2015). The oxygenated biofuel is also known as biodiesel. Bio-oil and biodiesel can be grouped as biofuels, which are environmentally friendly alternative fuels that can replace petroleum. However, they both have different hydrocarbon compositions. Biodiesel contains hydrocarbon compounds with oxygen atoms in esters. The bio-oil contains a large number of organic compounds, namely alkanes, aromatic hydrocarbons, and phenol derivatives. Small amounts of ketones, esters, ethers, sugars, amines and alcohols with an H/C molar ratio higher than 1.5 were identified in bio-oil (Lu et al., 2009; Wu et al., 2009). The method of high thermal decomposition (pyrolysis) without the addition of O_2/air was used to produce it (Isahak et al., 2012).

Fatty acid methyl esters or biodiesel were produced by transesterification of the extracted seed-derived vegetable oils (e.g., rapeseed oil, cotton oil, palm oil, soybean oil, and jatropha seed) and methanol. It was still having the properties that have not been profitable for diesel engines (Ayodele et al., 2015; Chen et al., 2016; Kim et al., 2013; Pinto et al., 2013; Šimáček et al., 2009; Wang et al., 2014). Some phenomena, such as blockages in some parts of the fuel system, the appearance of deposit and sludge on the storage system, corrosion on metal parts due to the relatively high-water solubility in FAMEs, causing swelling of rubber components, can be a factor causing engine damage (Kim et al., 2013; Šimáček et al., 2009; 2011). The limiting properties of FAMEs for the application directly as a fuel in vehicle engines are low energy density, poor oxidation stability of FAMEs (Ayodele et al., 2015; Chen et al., 2016; Kim et al., 2013), which is caused by excess oxygen incorporated in carboxyl or carbonyl groups (Chen et al., 2016; Kim et al., 2013; Romero et al., 2015; Wang et al., 2014), the high value of viscosity and pour point, poor calorific value (Wang et al., 2014), poor storage stability, and glycerol by-product menace (Ayodele et al., 2015). Therefore,

FAMEs composed of the different chemical compounds can damage the engine combustion and reduce the engine performance (Pinto et al., 2013).

The other method for converting vegetable oil to biofuel is hydrocracking applied before in crude oil refinery unit with heterogeneous catalyst. Some of the catalysts have been applied in vegetable oils processing into biofuel through the catalytic cracking and hydrocracking. The CoMoS and NiMoS catalysts (Kim et al., 2013; Zhang et al., 2014), NiMo/ZSM-5-alumina (Ishihara et al., 2014), CoMo/γ-Al_2O_3 (Bezergianni et al., 2014; Pinto et al., 2014; Rasyid et al., 2015), ultra-stable Y (USY) zeolite (Li et al., 2014), HZSM-5 based catalyst, e.g., Ni or Zn supported on HZSM-5 (Budianto et al., 2014a; Roesyadi et al., 2013), Pt, Pd, or Au supported on H-ZSM-5 (Budianto et al., 2014b), Ni-Zn/HZSM-5 (Prajitno et al., 2015), Ni or Ga supported on HZSM-5 (Tamiyakul et al., 2016) were typical catalysts for catalytic cracking or hydrocracking of triglycerides to obtain biofuel. However, the mesoporous zeolite is preferred to support diffusion of the reactants and produce alkane isomers with relatively high yields (Chen et al., 2016).

Wang et al. (2014) deoxygenated soybean oil with the Ni/HZSM-5 catalyst through a single-step hydrotreatment process combining deoxygenation of fatty acid into n-paraffin as the main hydrocarbon product and isomerization to obtain isoparaffin. Apparently, catalytic activity of Ni/SAPO-11 is higher than Ni/HZSM-5 catalyst in a single-step hydrotreatment process based on the amount of n-paraffin produced and oxygenated compounds remaining. Hierarchical pore structure becomes a good solution to obtain the size of micropores-mesopores on HZSM-5 in an effort to increase the activity of catalyst, as suggested by Liu et al. (2015). With the Ni/HZSM-5 catalyst, Chen et al. (2016) promoted long-chain unsaturated FAMEs through one-step catalytic hydroprocessing (including deoxygenation and decarboxylation or decarbonylation, followed by isomerization). With the Ni/HZSM-5 catalyst (silica to alumina ratio of 25) and metal loading of 10 wt.%, it was found that high selectivity of C5-C18 n-paraffins and isomerization selectivity were 88.2 and 27.0%, respectively (Chen et al., 2016). In this case, changes in the Si/Al ratio affect the acidity of the zeolite and have an impact on variations in the composition of hydrocarbon compounds in the liquid product. Based on this, it is remarkably interesting for impregnating double promoter of Ni and Zn metal into HZSM-5 zeolite. This prepared catalyst is expected to improve the degree of triglycerides hydrocracking when compared to using one active metal only.

So far, the fuel produced has characteristics which can maintain the machine durability and do not require substantial modification of conventional machines. Problems resulted from the use of FAMEs are resolved through the removal of oxygen atoms in the fatty acid by reaction hydrocracking, i.e., hydrodecarbonylation/decarboxylation (HDC) and hydrodeoxygenation (HDO) (Arun *et al*., 2015; Ishihara *et al*., 2014; Kim *et al*., 2013; Silva and Sousa, 2013; Zhang *et al*., 2014) and then followed by isomerization. Kim *et al*. (2013) stated it is especially important to understand and control the reactions (i.e., dehydrogenation, isomerization, cyclization, and aromatization) related to the oxygen removal on triglycerides in hydrocracking process to produce biofuel with fuel properties (including cloud point and cetane number). The fuel properties were influenced by hydrocarbon composition, such as (normal, iso-) paraffin, olefins, cycloparaffin, and aromatic. These reaction routes may lead to the formation of hydrocarbons such as n-paraffins, isoparaffins, cycloparaffins, aromatics, and olefins (Kim *et al*., 2013; Ishihara *et al*., 2014; Zhang *et al*., 2014). It is very important to keep the hydrogen partial pressure not too high during the hydrocracking process because it resulted in a low yield of hydrocarbons, as stated by Santillan-Jimenez and Crocker (2012).

Biofuel derived from nonedible vegetable oil through hydrocracking process is becoming a promising renewable alternative fuel in sustainable energy production. The candlenut, jatropha, rubber seed, *Cerbera manghas* seed, *Calophyllum inophyllum* have been used as sources of nonedible vegetable oils. Seeds from these plants contain toxic substances which humans cannot consume, e.g., cerberin is found in *Cerbera manghas* seed. Carlier *et al*. (2014) also reported that dry seeds of *Cerbera manghas* contained a number of compounds: cerberin, deacetyltanghinin, neriifolin, and tanghinin. *Cerbera manghas* trees, part of the ecosystem of the mangrove forests, can reach a height of 12 m. These plants can be found as urban greening plants. Their seeds contained a high level of crude Cerbera oil of approximately 46–64%.

In this work, the influence of reaction temperature for two different composition ratios of metals impregnated on HZSM-5 on the hydrocarbon composition in biofuels by hydrocracking of *Cerbera manghas* oil is discussed. It is expected that characteristics of hydrocarbon composition in the biofuel produced are similar to petroleum-based fuels. Based on gas chromatography-mass spectrometry (GC-MS) analysis, decarboxylation/decarbonylation occurred during hydrocracking was also discussed.

2. Materials and Methods

2.1 Extraction of Cerbera manghas

Dried fruits of *Cerbera manghas* were obtained from plant that grows in Keputih, Surabaya, Indonesia. It is also known as Bintaro plant in Java Island. *Cerbera manghas* oil was extracted from seeds through the process steps that according to previous literature, as shown in Fig. 1 (Roesyadi, 2016). At first the fruit was split and the seeds were removed from the fruit. These seeds were cleaned from the skin and obtained white oval-shaped seeds. Furthermore, the seeds were dried in the sun for 7 days. After drying, the dry seeds were chopped and extracted by hydraulic press to produce oil. Oil was stored in an airtight container to prevent oxidation, which can increase free fatty acid levels. *Cerbera manghas* oil from the hydraulic extraction process was obtained as much as 2.5 L from 6 kg of seeds. It can be said that 2 kg of Bintaro seeds produce about 0.8 L of oil. Figure 2 specify the different conditions of the seed and the obtained oil.

Figure 1. Extraction process of *Cerbera manghas* seeds. **(a)** the fruit was split into two parts, **(b)** the seeds were removed from the fruit, **(c)** the seeds were dried in the sun, **(d)** the dry seeds were chopped, finally **(e, f)** the seeds were extracted by hydraulic press.
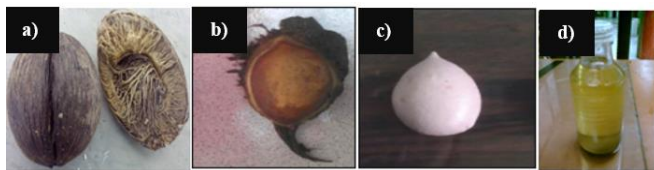**Source:** Adapted from Roesyadi (2016).

Figure 2. Different condition of *Cerbera manghas* fruit and the obtained oil. **(a)** a dried fruit, **(b)** seed with skin, **(c)** white oval-shaped seeds seed, **(d)** oil.
Source: Adapted from Roesyadi (2016).

2.2 Catalyst preparation

ZSM-5 zeolite in ammonium form (CBV 8014, SiO_2/Al_2O_3 ratio of 25, surface area of 400 m^2 g^{-1}, Na$_2$O of 0.05 wt.%) was provided from Zeolyst International. Meanwhile, Ni(NO$_3$)$_2$.6H$_2$O and Zn(NO$_3$)$_2$.6H$_2$O as the metal precursor were obtained from Merck with 98% purity. The calcination process on NH$_4$-ZSM-5 zeolite was applied to obtain HZSM-5 zeolite at temperature of 550 °C for 5 h (Sartipi *et al.*, 2013). By incipient wetness impregnation method (Haber *et al.*, 1995; Marlinda *et al.*, 2016; Sartipi *et al.*, 2013), HZSM-5 after calcined was impregnated with nickel and zinc to obtain Ni-Zn/HZSM-5 catalyst. Before impregnation, the HZSM-5 zeolite was dried overnight at a temperature of 120 °C. The amount of aqueous metal solutions was calculated according to the total pore volume of HZSM-5 as support, which was obtained from Brunauer–Emmett–Teller (BET) analysis, as shown in Table 1. After preparing aqueous metal solutions, firstly the amount of aqueous Ni(NO$_3$)$_2$.6H$_2$O solution of 1.81 mol L^{-1} was sprayed slowly to HZSM-5 zeolite while stirring and then kept overnight in a desiccator. Finally, this catalyst was dried at 120 °C for 12 h. Furthermore, in the same way as before, the amount of aqueous Zn(NO$_3$)$_2$.6H$_2$O solution of 1.62 mol L^{-1} was sprayed slowly to HZSM-5 zeolite while stirring. Before drying at temperature of 120 °C for 12 h, the catalyst was kept overnight in a desiccator. Catalysts containing Ni and Zn salt solution were calcined with air at temperature of 400 °C for 2 h. After calcination, active metal usually exists as a form of metal oxide (Kim *et al.*, 2013; Romero *et al.*, 1998). The metallic phases of Ni and Zn were obtained by reducing the metal oxides under flowing hydrogen at a temperature of 450 °C for 3 h. By atomic absorption spectrometry, the metal content was 5.43 wt.% of Ni and 1.23 wt.% of Zn of the total catalyst weight. The catalyst is denoted as Ni(5.43%)-Zn(1.23%)/HZSM-5 catalyst. Other prepared catalyst is Ni(5.42%)-Zn(1.11%)/HZSM-5.

Table 1. The characterization of H-ZSM-5 and Ni-Zn/HZSM-5 catalyst.

Catalyst	Surface area (m^2 g^{-1})			Volume (cm^3 g^{-1})			D^f (nm)	Actual metal content^g (wt.%)		References
	Total^a	Micro	Meso	Total^c	Micro^d	Meso^e		Ni	Zn	
HZSM-5	362.77	315.13	47.64	0.245	0.156	0.089	2.709	-	-	Present study
Ni(5.43%)-Zn(1.23%)/HZSM-5	-	-	-	-	-	-	-	5.43	1.23	Present study
Ni(5.42%)-Zn(1.11%)/HZSM-5	246.06	205.52	40.54	0.191	0.101	0.090	3.109	5.42	1.11	(Roesyadi *et al.*, 2016)

a = total surface area BET; b = the surface area mesoporous and microporous obtained from the t-plot; c = total pore volume; d = micropore volume obtained from the t – plot; e = mesoporous volume = V$_{meso}$ = V$_{total}$ − V$_{mikro}$; f = average pore diameter; g = atomic absorption spectrometry (AAS) analysis.
Source: Elaborated by the authors using data from Roesyadi *et al.* (2016).

2.3 Characterization of catalyst

The various techniques used to characterize catalysts were X-ray diffraction (XRD), atomic absorption spectrometry (AAS) and N$_2$ adsorption-desorption. The metal contents of Ni dan Zn were confirmed with AAS. In principle, the distribution of metal on ZSM-5 is influenced by the preparation method used (Chen *et al.*, 2015). X-ray diffraction was applied to identify phase analysis and the Ni-Zn/HZSM-5 catalyst crystallinity. X-ray diffraction patterns of the solid catalyst (Phillip X-Pert diffractometer with Cu radiation Kα) were collected from 2θ of 5–90° to identify the peak of crystalline zeolite ZSM-5. The existence of the crystalline phase of NiO, ZnO, Ni and Zn particles was confirmed from the diffraction patterns recorded on 2θ = 30–80°.

The catalyst surface area was measured by BET calculation on Quantachrome NovaWin Version 10.0 according to the adsorption data with the relative pressure (P/Po) in range from 0.095 to 0.297 through the recording process of isotherm BET on five points. Before the measurement of nitrogen adsorption and desorption isotherms at a temperature of 77 K, the sample was outgassed for 16 h at 300 °C. The pore size

distributions were calculated using adsorption model of Barrett–Joyner–Halenda (BJH). Micropores volumes were obtained from the t-plot analysis. Total pore volumes were obtained according to the amount of nitrogen adsorbed at relative pressure about 0.99034. Mesoporous volumes were obtained from the reduction of the total pore volume by the volume of micropore.

2.4 Hydrocracking reaction

Hydrocracking reactions were carried out in the Parr USA pressure batch reactor equipped with a mechanical stirrer. *Cerbera manghas* oil of 150 mL and catalysts of 1 g were transferred in the reactor. To remove air, nitrogen was flowed into the reactor at least 30 min for purging. Depending on temperature condition, reaction pressure was changed between 15 and 25 bar after flowing H_2 for at least 1 h, as reported in previous study (Marlinda *et al.*, 2016). The reaction proceeded at various temperatures, i.e., 350, 375 and 400 °C for 2 h. After a reaction time was reached, the reactor temperature was allowed to reach room temperature. Furthermore, biofuel was analyzed by GC-MS, i.e., Agilent HP 6890 GC equipped with a capillary column, model Agilent 19091S-433 (HP–5MS, phenylmethylsiloxane of 5%). The column dimensions used have an internal diameter of 0.25 mm, film thickness of 0.25 μm and a length of 30 m. All

hydrocarbon components are identified using the Wiley275 and NIST02 mass spectral library of data. Based on GC-MS analysis, it is possible to estimate the relative percentages of hydrocarbon composition and distribution of products to their carbon numbers. According to Barrón *et al.* (2011), hydrocarbon compounds (including n-paraffin, isoparaffin, cycloparaffin, aromatic, olefin) were grouped in gasoline-like hydrocarbon (C5-C9), kerosene-like hydrocarbon (C10-C13), and gasoil-like hydrocarbon (C14-C22).

3. Results and discussion

3.1 Oil characterization

The clear yellow color of *Cerbera manghas* oil without purification was analyzed by GC-MS. Table 2 indicated that the most abundant compound in *Cerbera manghas* oil is oleic acid at 77.76 area%, which agrees with that obtained by Marlinda *et al.* (2016). Oleic acid is also the largest constituent of *Calophyllum inophyllum* oil, *Jatropha curcas* oil (Chuah *et al.*, 2016) and *Pongamia pinnata* oil (Dwivedi and Sharma, 2015), as much as 39.8 ± 0.4, 51.2 ± 0.6 and 65.3 wt.%, respectively.

Table 2. Compounds of *Cerbera manghas* oil tested by GC-MS.

Compound	Chemical name	Molecular formula	Content (%)
Palmitic acid; C16:0	Hexadecanoic acid	$C_{15}H_{31}COOH$	20.29
Oleic acid; C18:1	9-Octadecenoic acid	$C_{17}H_{33}COOH$	77.76
Ethyl palmitate	Hexadecanoic acid, ethyl ester	$C_{18}H_{36}O_2$	1.95

Source: Elaborated by the authors using data from Prajitno *et al.* (2015).

3.2 Catalysts characterization

Some different techniques were used to obtain the textural properties and metal content of the Ni-Zn/HZSM-5 catalyst. Figure 3 shows the type of adsorption isotherms classified by International of Pure Applied Chemistry (IUPAC) for HZSM-5 and Ni-Zn/HZSM-5 catalyst. It was clear that a combined pattern of type I and type IV was exhibited in Fig. 3b. The type of microporous solids owned by HZSM-5 is type I isotherm, as shown in Fig. 3a. It shows an initial curve that rises sharply at very low relative pressure, as reported in previous studies (Hao *et al.*, 2012; Sartipi *et*

al., 2013; Wang *et al.*, 2013). The mesopores and the pore size distribution calculated from the sorption isotherm can be called hysteresis. The presence of hysteresis exhibited with type IV isotherm was seen on high relative pressure of 0.65 towards 0.85, at which N_2 desorption does not pass through the adsorption original path (Hao *et al.*, 2012; Vitale *et al.*, 2013; Wang *et al.*, 2013). Nickel and zinc impregnated on support can create mesoporous sites in catalyst, so that bulky molecules can diffuse easily to the pores of catalyst, as reported in previous studies (Hao *et al.*, 2012; Vitale *et al.*, 2013; Wang *et al.*, 2013).
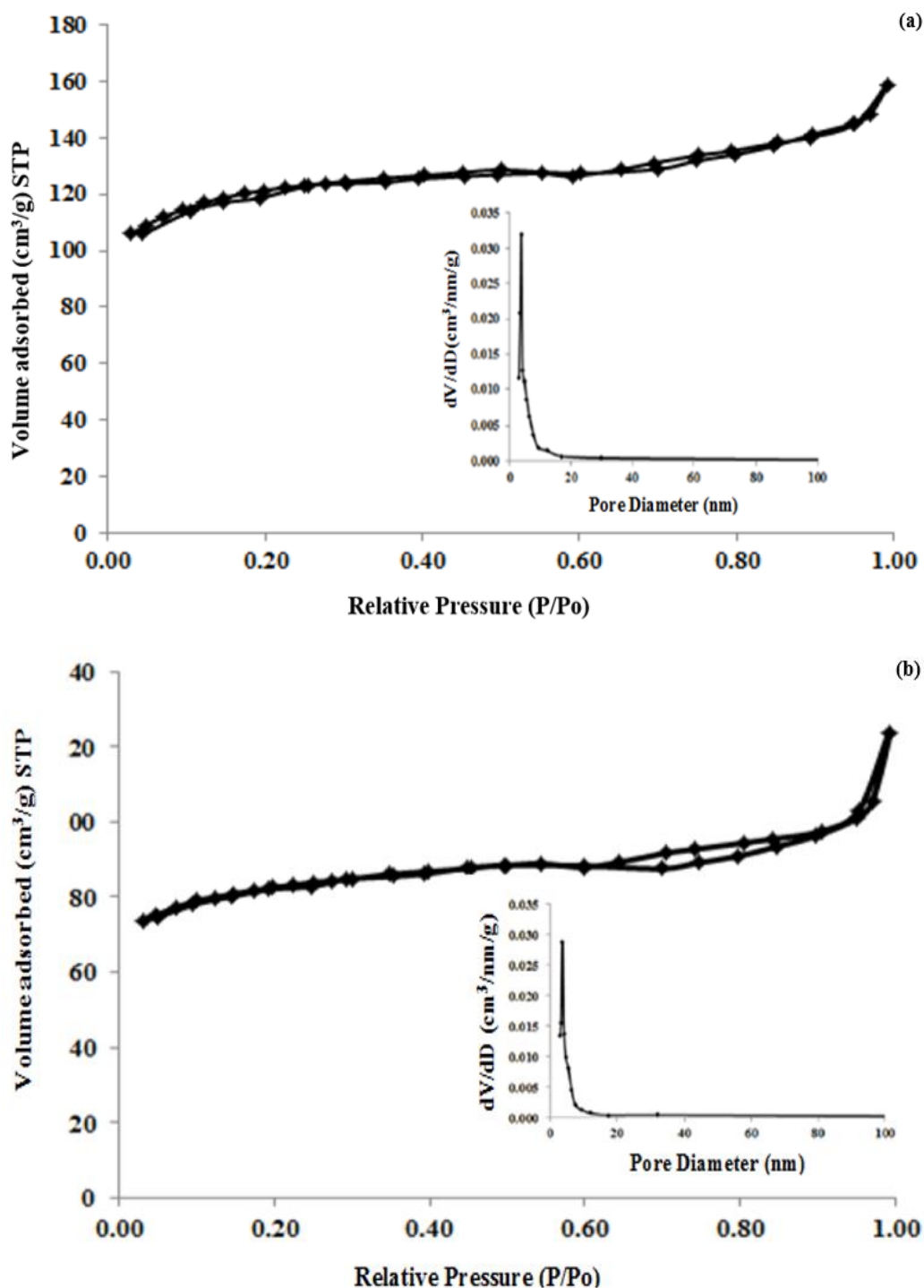
Figure 3. Nitrogen adsorption and desorption and BJH pore size distribution of catalyst. **(a)** HZSM-5; **(b)** Ni(5.42%)-Zn(1.11%)/HZSM-5 catalyst.

The pore size distributions of the two types of the catalyst were centered at 3.8 nm. However, the slightly narrower pore size distribution and lower peak height were seen on Ni–Zn impregnated on HZSM-5. Reduction of peak height on the catalyst showed that the presence of Ni and Zn had a considerable influence on the pore structure of HZSM-5. Both of the catalysts have a mesoporous structure as the result of the interparticle voids. This pore structure will greatly affect the increase of reactivity of the catalysts, as reported by Wang *et al.* (2013).

Table 1 shows that micropores volume decreased from 0.156 to 0.101 cm^3 g^{-1}, while pore diameter increased from 2.709 to 3.109 nm after Ni–Zn metals were impregnated on HZSM-5. Nevertheless, Chen *et al*. (2016) stated that the internal nickel particles can inhibit the nitrogen molecules into the pore by blocking the micropores of HZSM-5. However, the increase of pore diameter and the presence of mesopores size distribution indicated that fatty acids had a significant probability to diffuse into the pores successfully and react on the active sites. According to Bockisch (1998), assuming a typical triglyceride molecule to have a spherical form, its diameter would be 1.5 nm. Therefore, if the fatty acids cannot diffuse and react with the active sites located in micropores channel, then these fatty acids will diffuse and react with the active sites located in mesopores channel. While the actual metals content obtained were shown in Table 1.

X-ray diffraction data of catalyst system shows that the full diffractograms were recorded in the range 2θ° of 5–90 to see the diffraction peak of NiO, ZnO, Ni and Zn in the catalyst samples. The characteristic of diffraction peaks of commercial HZSM-5, as shown in Fig. 4a, located at 2θ of 7.9, 8.8, 23.09, 23.31, 23.69, 23.9 and 24.4°, which indicated a structure type mordenite framework inverted (MFI), as reported by a previous study (Marlinda *et al*., 2016). As shown in Fig. 4b and c, diffractograms of catalyst used for the hydrocracking on *Cerbera manghas* oil were almost similar to those of commercial HZSM-5.
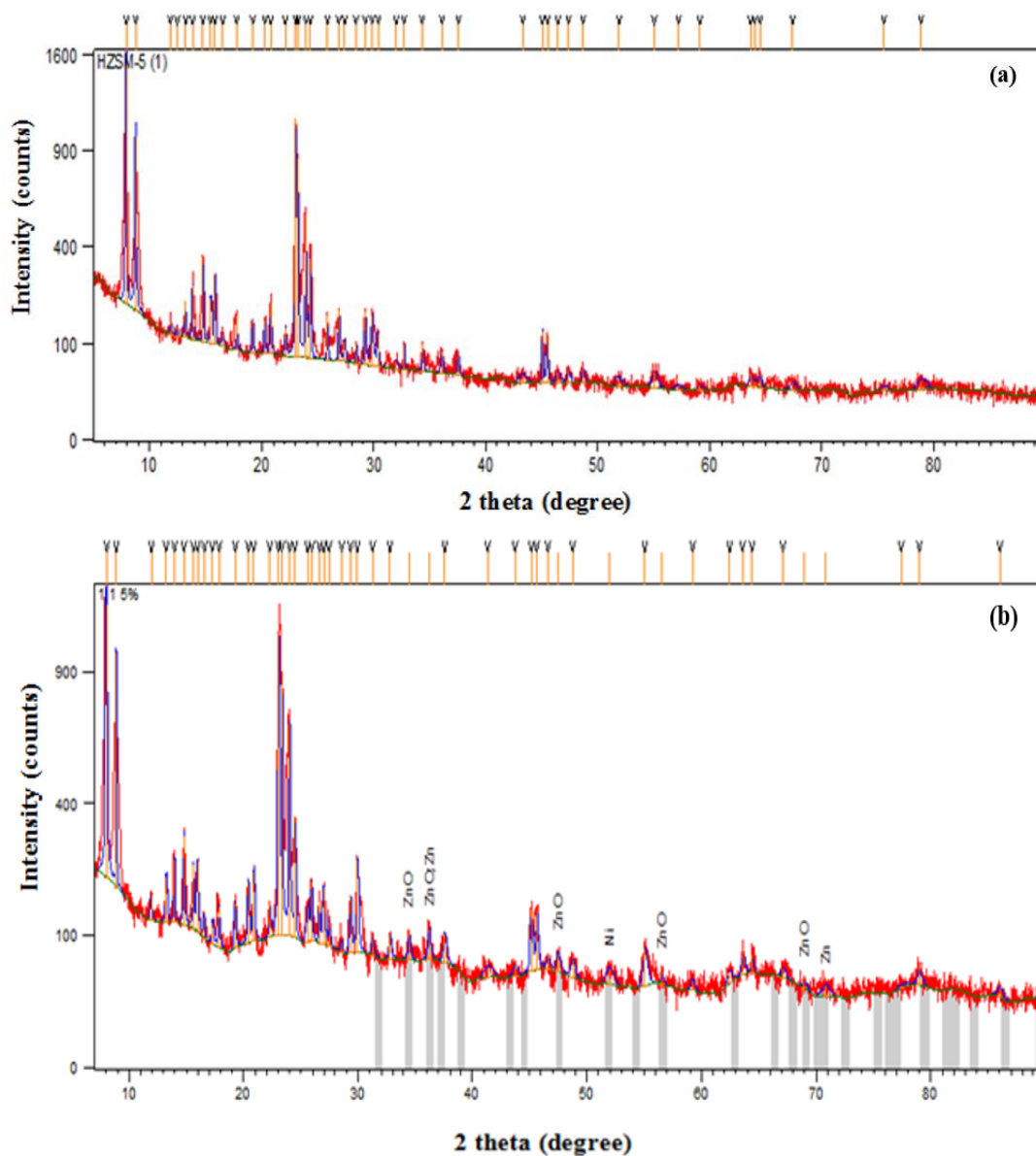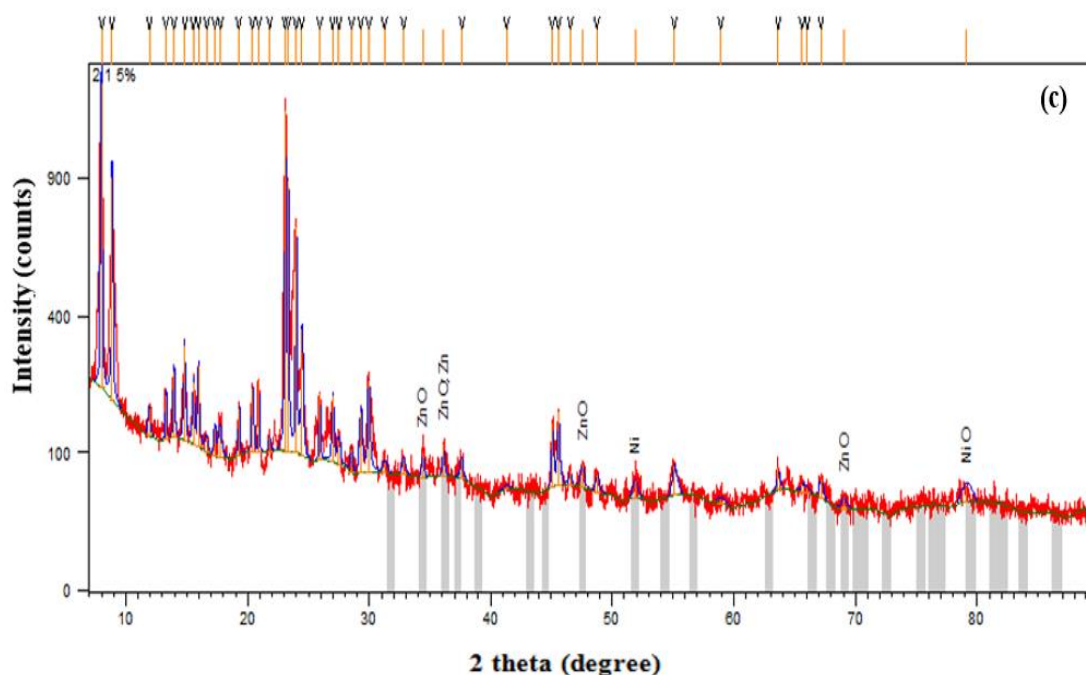
Figure 4. X-ray diffraction pattern of catalysts. **(a)** Commercial HZSM-5 after calcined (Marlinda *et al.*, 2016), **(b)** Ni(5.43%)-Zn(1.23%)/HZSM-5 catalyst, **(c)** Ni(5.42%)-Zn(1.11%)/HZSM-5 catalyst.

After impregnation with Ni–Zn, the HZSM-5 framework structure was almost unchanged, but only the intensity of each diffraction peak decreased (Chen *et al.*, 2016; Niu *et al.*, 2014; Wang *et al.*, 2013). Figure 4b shows that a small intensity diffraction peak of ZnO crystallites was observed at 2θ of 34.55, 36.32, 47.56, 56.66 and 69.08°. The Zn and Ni particles were also observed at 2θ of 70.94 and 52.06° with low intensity, respectively. While the presence of NiO crystallite was not found. Figure 4c shows that a small peak diffraction intensity of ZnO crystallites were observed at 2θ of 34.53, 36.19, 47.58 and 69.10°. NiO crystallite and Ni particle were observed at 2θ of 79.23 and 51.96° with low intensity, respectively. While the presence of Zn metal was not detected. When incipient wetness impregnation method was applied by means of physical mixing, diffraction peak for ZnO was obtained at 2θ of 36.21°, as observed by Niu *et al.* (2014). In principle, the reduction of ZnO and NiO crystallites with hydrogen will lead to the formation of proton ions (H$^+$), as the Bronsted acid. As reported by Chen *et al.* (2016), after reduction of NiO with hydrogen, proton ion (H$^+$)

was formed (Ni^{2+} + H$_2$→Ni + 2H$^+$) so that the catalysts which contained Bronsted acid sites (weak strength sites) have contributed to direct isomerization reaction. While Lewis acid sites (strong acid sites) may direct the ability of cracking.

3.3 Biofuel analysis

Biofuel produced from hydrocracking of *Cerbera manghas* oil at a temperature of 400 °C with a Ni-Zn(2%)/HZSM-5 catalyst and Ni-Zn(4%)/HZSM-5 (Prajitno *et al.*, 2015) still contained many carboxylic acids and compounds containing more oxygen, i.e., 9-octadecenal in the range of 5.35–6.11% and ethenone in the range of 0.20–0.37%. Table 3 shows that olefins are found in very small quantities while the n-paraffins and cycloparaffins can only be obtained from catalyst with metal loading of 4%. It indicated that the metals impregnated on HZSM-5 have not been able to hydrogenate fatty acid. The GC-MS spectra of biofuel is shown in Fig. 5.
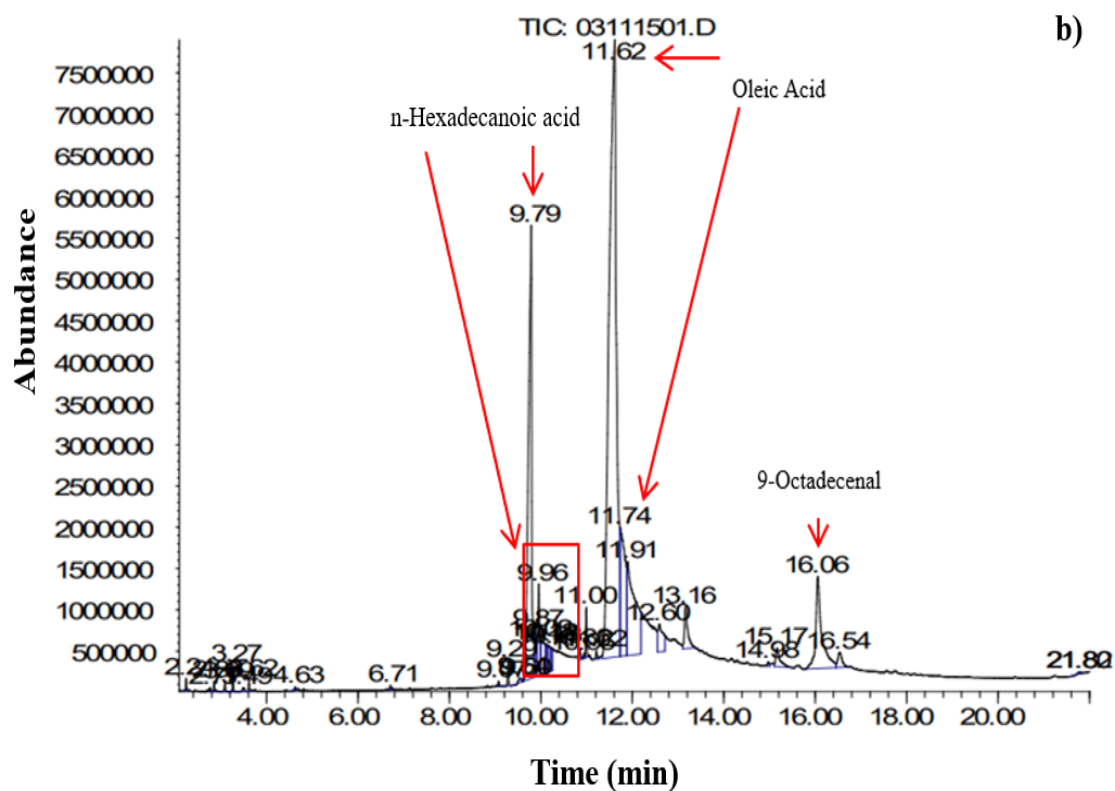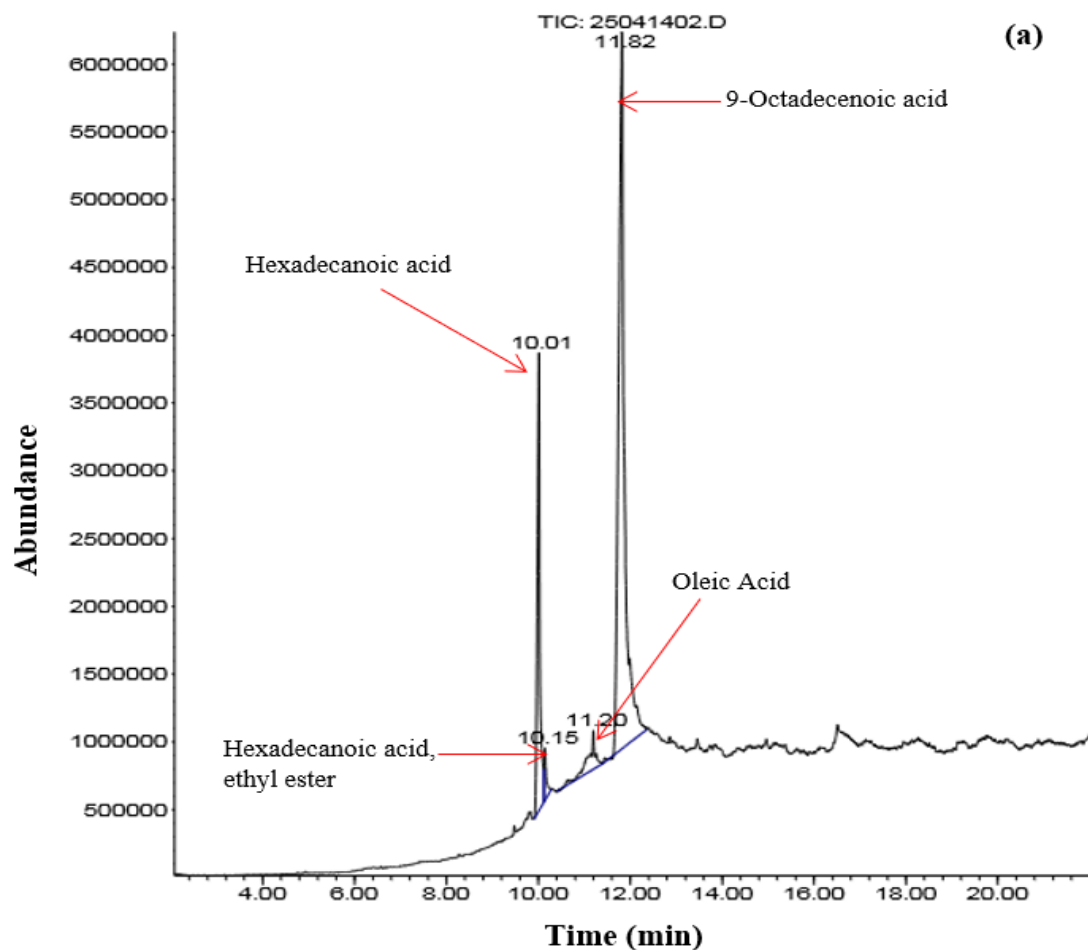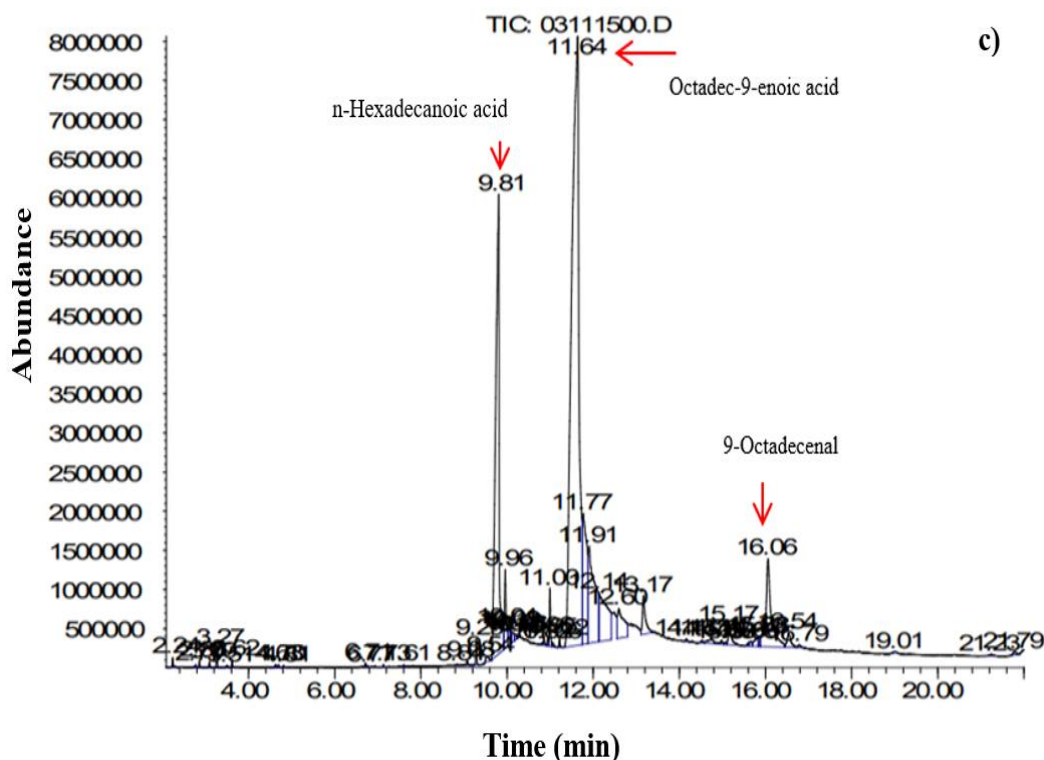
Figure 5. Gas chromatography-mass spectrometry spectra of **(a)** *Cerbera manghas* oil (Prajitno *et al.*, 2015), and liquid products produced at 400 °C with **(b)** Ni-Zn(2%)/HZSM-5 catalyst, **(c)** Ni-Zn(4%)/HZSM-5 catalyst, under pressure 20 ± 5 bar in the batch reactor.

Table 3. Hydrocarbon composition of biofuel produced by hydrocracking at temperature of 400 °C under pressure 20 bar in batch reactor, tested GC-MS.

Catalyst	Hydrocarbon composition of biofuel (area%)					
	n-paraffin	cycloparaffin	aromatic	olefin	carboxylic acid	Compound containing oxygen
Ni-Zn(2%)/HZSM-5	0	0	0	0.05	93.09	6.74
Ni-Zn(4%)/HZSM-5	0.02	0.06	0	0.07	92.99	6.67

Gas chromatography-mass spectrometry spectra of *Cerbera manghas* oil and biofuel produced in the various reaction temperatures and metal loading of 5% are shown in Fig. 6 and 7, respectively. When Fig. 6 and 7 are compared, it can be seen that the compounds with retention time of 10–18 min in GC-MS spectra of *Cerbera manghas* oil disappear after reaction, as reported by a previous study (Marlinda *et al.*, 2016). It indicated that the triglycerides containing long chain molecules were converted into short chain molecules by hydroprocessing (including cracking, deoxygenation, and isomerization reaction) with HZSM-5 catalyst, as reported by a previous study (Zheng *et al.*, 2015). Meanwhile, the number of different compounds with retention time of 0–9 min increased, as shown in Fig. 7. The presence of Ni and Zn metals have contributed to the hydrogenation process of unsaturated fatty acids into n-paraffins.
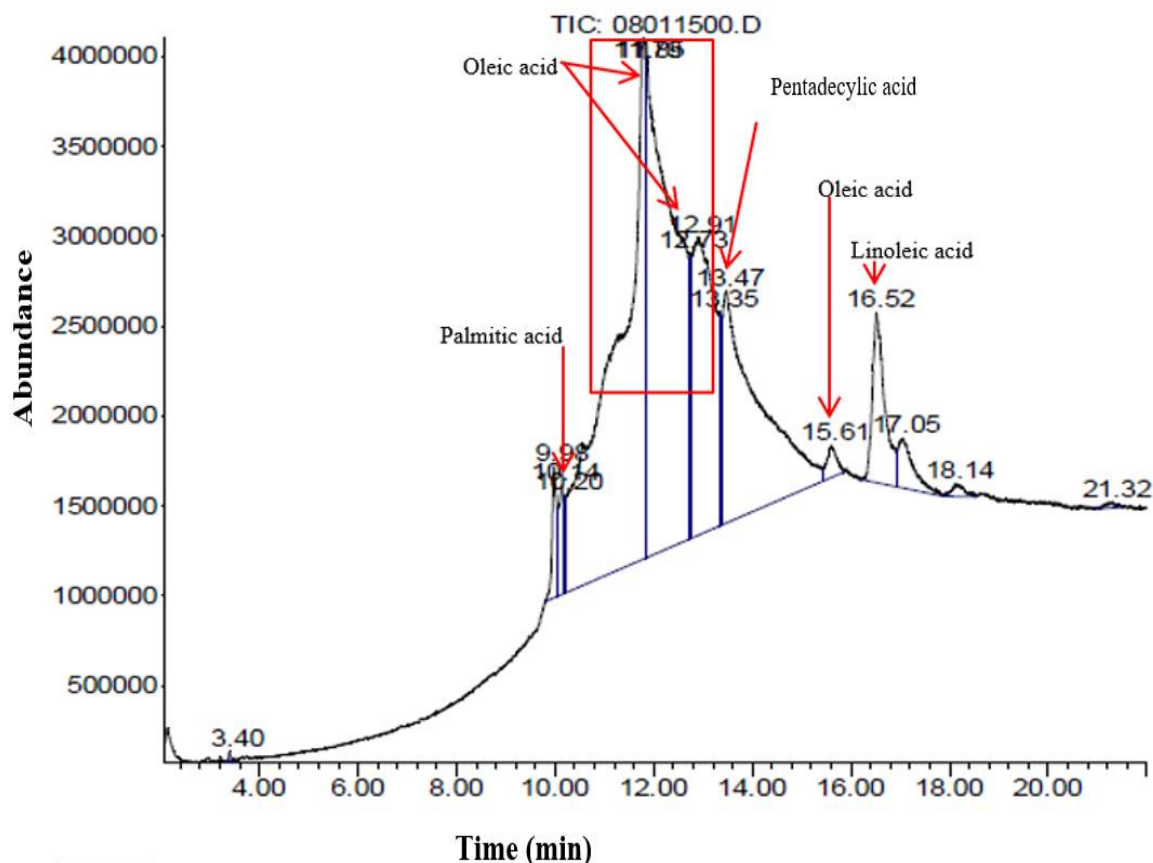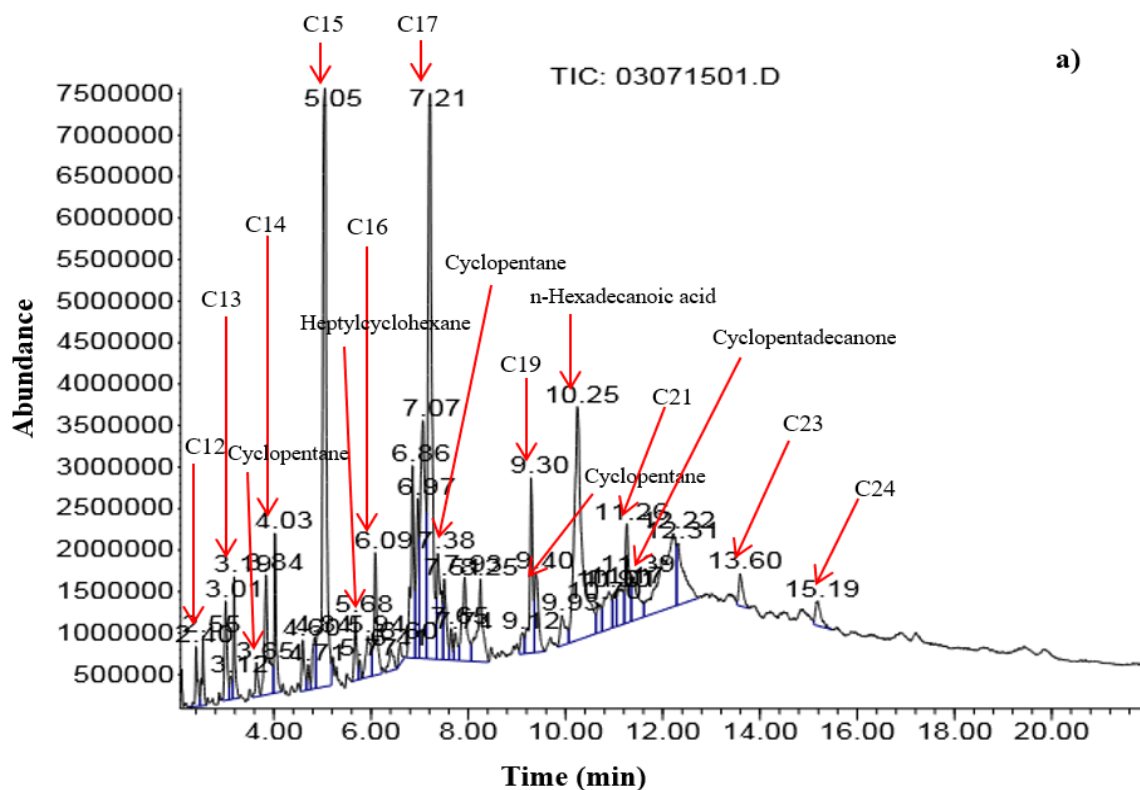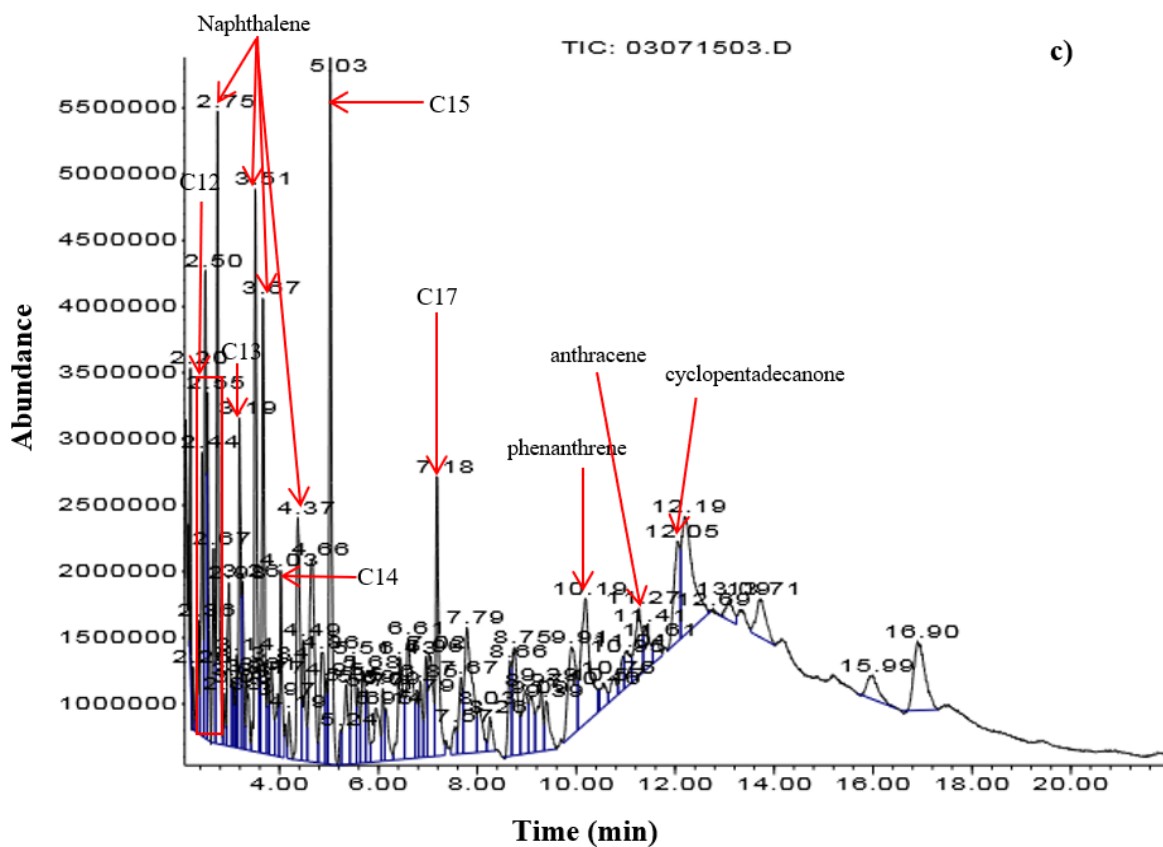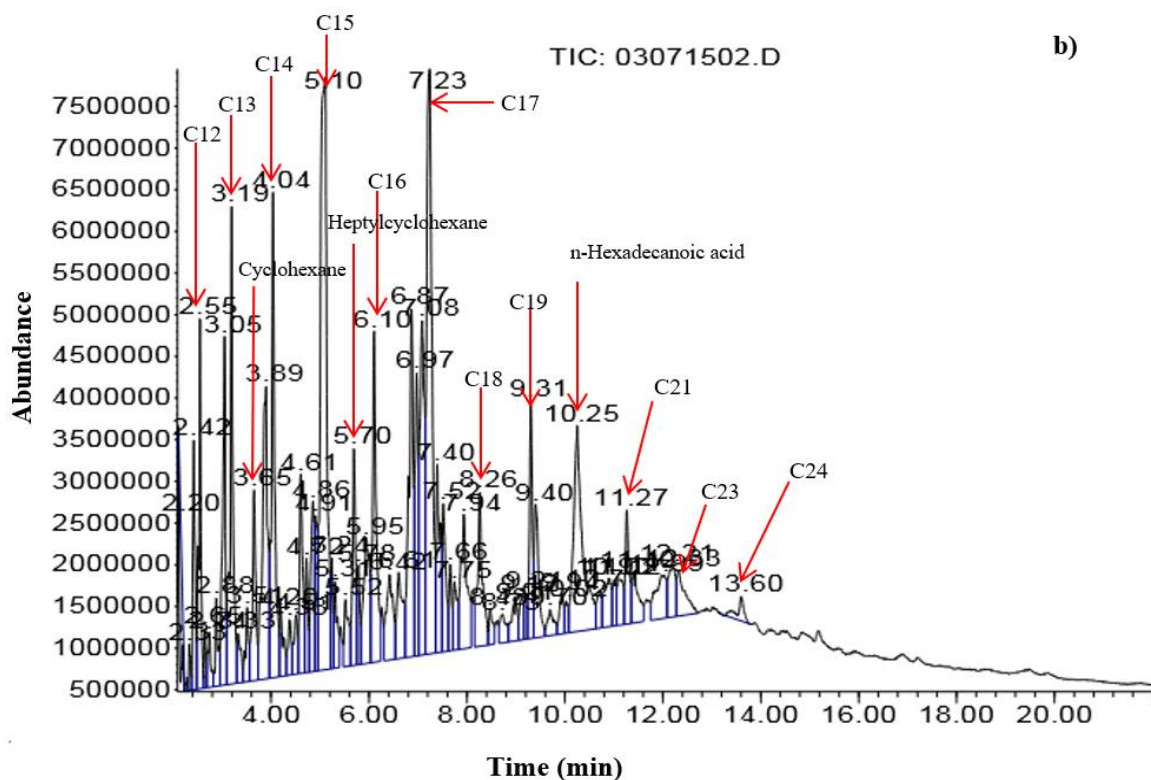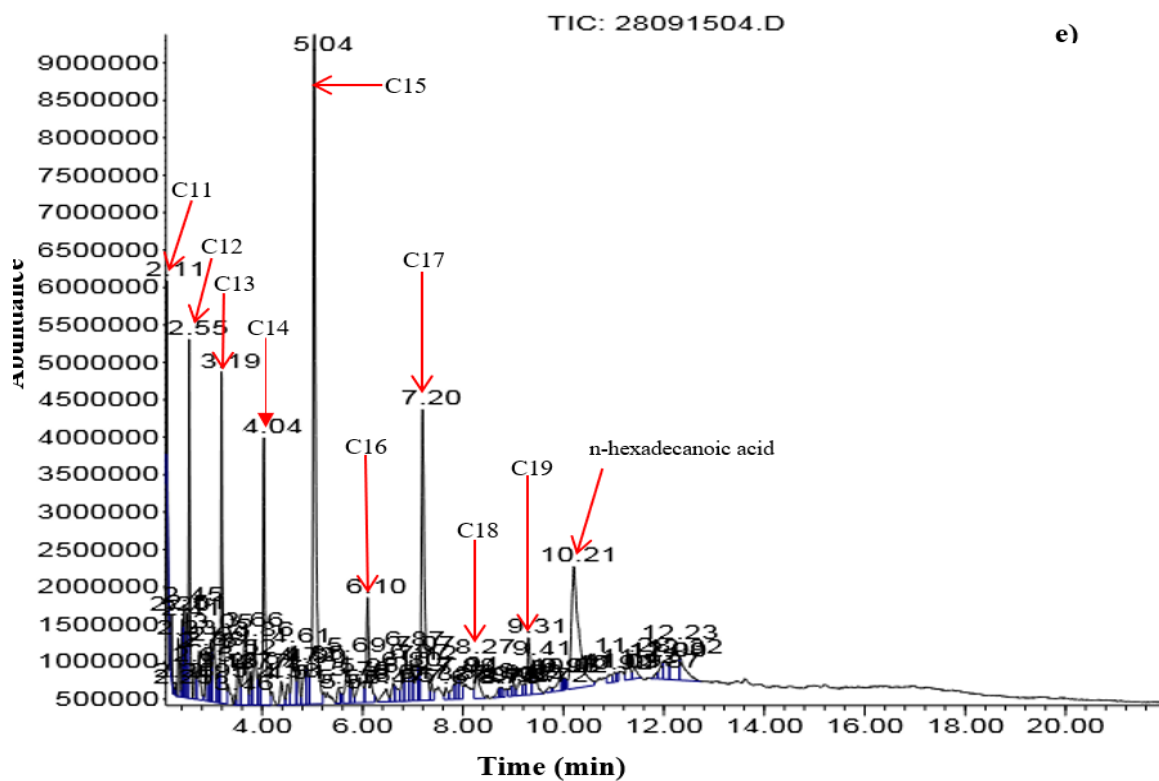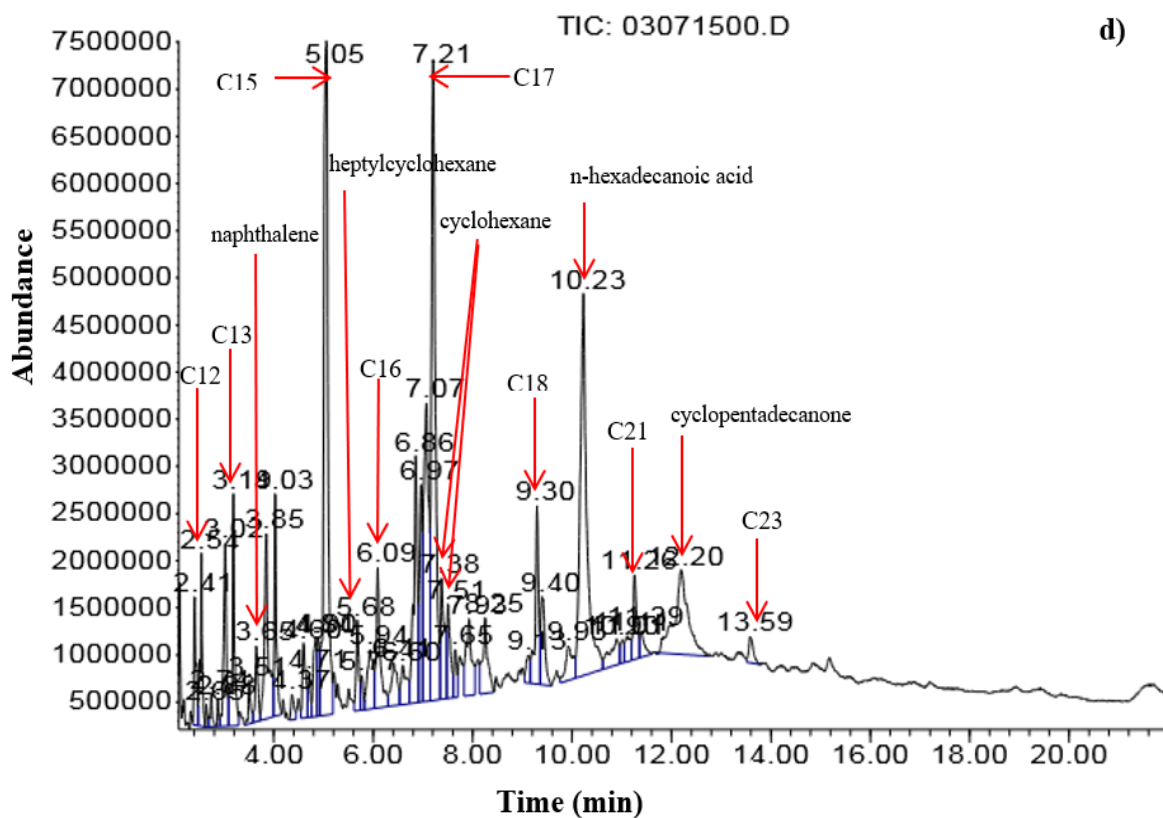
Figure 6. Gas chromatography-mass spectrometry spectra of *Cerbera manghas* oil.
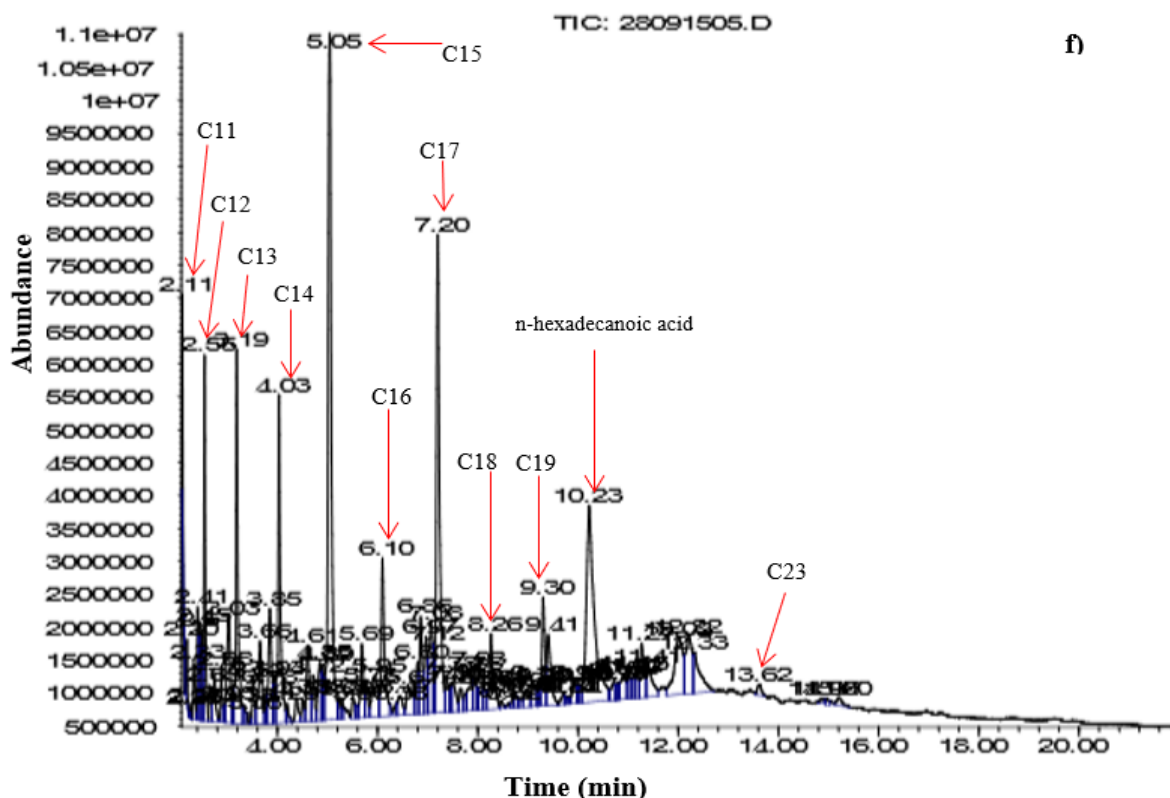**Source:** Adapted from Marlinda *et al*. (2016).

Figure 7. Gas chromatography-mass spectrometry spectra of biofuel produced at **(a)** 350 °C, **(b)** 375 °C, **(c)** 400 °C with Ni(5.43%)-Zn(1.23%)/HZSM-5 catalyst, and GC-MS spectra of biofuel produced at **(d)** 350 °C, **(e)** 375 °C, **(f)** 400 °C using Ni(5.42%)-Zn(1.11%)/HZSM-5 catalyst, under pressure 20 ± 5 bar in the batch reactor. Saturated chain hydrocarbons (n-paraffins) have the number of carbon atom from C12 to C24.

3.3.1 Effect of temperature on hydrocarbon composition

Figure 8a shows that biofuel contains a different hydrocarbon composition for each temperature of hydrocracking reactions with Ni(5.43%)-Zn(1.23%)/HZSM-5 catalyst. It can be seen that, at temperature of 350 °C, biofuel contained n-paraffins of 42.03 area%, but carboxylic acids of merely 15.48 area%, and compounds containing oxygen of 8.69 area%, i.e., octacosanol, were still found. Meanwhile, biofuel containing olefins of 20.31 area% and cycloparaffins of 12.48 area% was produced more at temperature of 375 °C. On the other hand, polycyclic aromatic hydrocarbons (PAHs) and aromatic are obtained at temperature of 400 °C, i.e., 21.32 and 35.47 area%, respectively. The existence of PAHs compounds

(including 1-methyl fluorene, phenanthrene, and anthracene) showed that the heating of vegetable oil was not complete. These compounds were not expected to present in biofuel. As reported by Vichaphund *et al.* (2015), deactivation occurred on HZSM-5 surface because of coke derived from PAHs compounds. Coke on the catalyst surface can be inhibited in the presence of hydrogen during hydrocracking reaction. However, overall, the compounds containing oxygen were still found in biofuel produced at all temperature variables. In principle, this compound should no longer exist in biofuel because the presence of oxygen atoms affects the viscosity and heating value, as reported by a previous study (Zheng *et al.*, 2015). Furthermore, isoparaffins were not found in biofuel for each reaction temperatures.
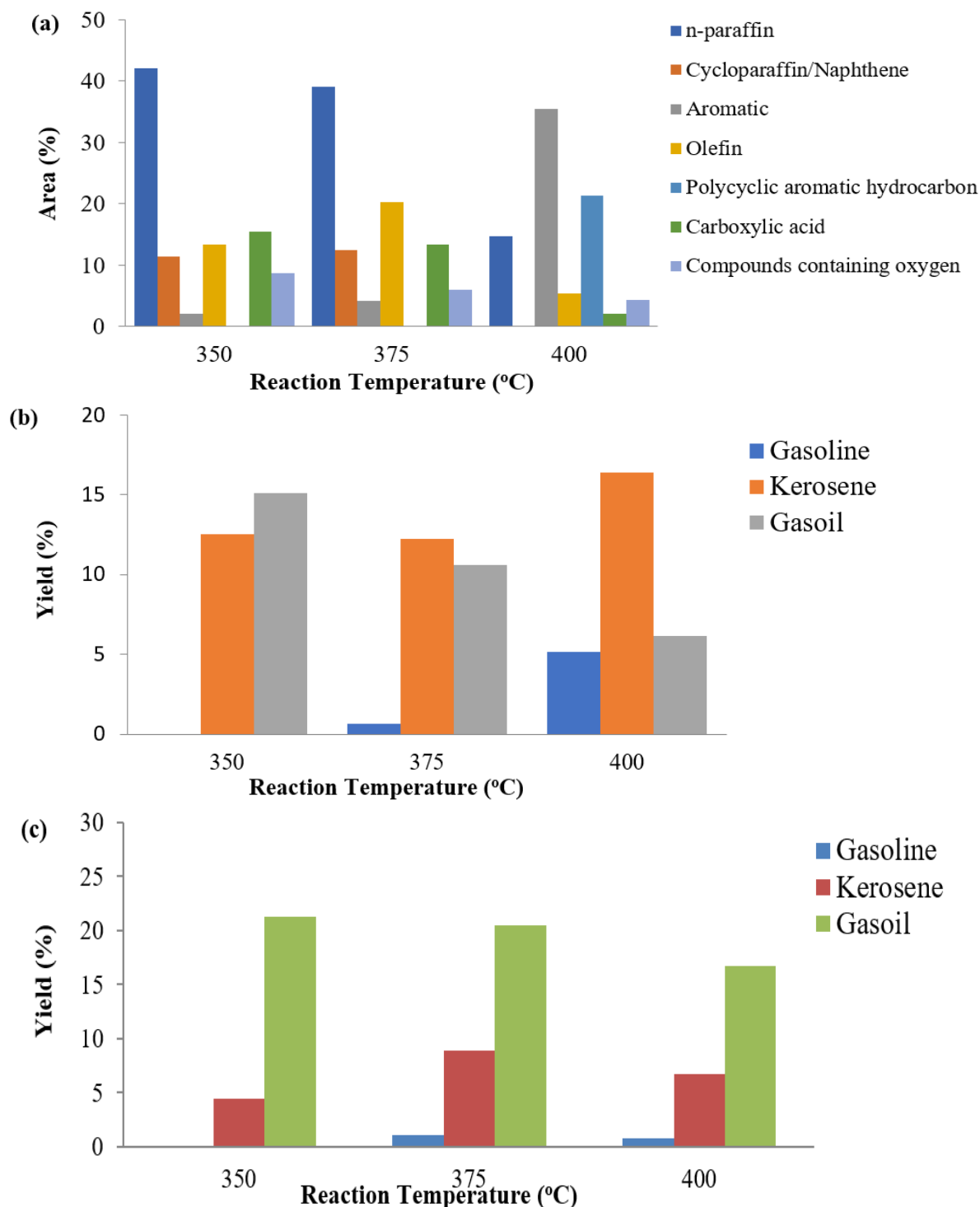
Figure 8. Effect of reaction temperature on **(a)** the hydrocarbon composition, **(b)** gasoline/kerosene/gasoil yields of liquid hydrocarbon fuel produced using Ni(5.43%)-Zn(1.23%)/HZSM-5 catalyst; **(c)** gasoline/kerosene/gasoil yields of liquid hydrocarbon fuel produced using Ni(5.42%)-Zn(1.11%)/HZSM-5 catalyst, under 20 bar in the batch reactor (**"c"** is elaborated by a previous study (Roesyadi *et al.*, 2016)).

The cracking of olefins into lighter hydrocarbon compounds was shown by the decrease of olefin at temperatures from 350 to 400 °C, as reported by Kim *et al.* (2013). On the other hand, aromatic hydrocarbon compounds, i.e., 1-methyl-2-(2-propenyl) benzene of 4.5 area%, 1-Methylnaphthalene of 4.79 area%, 1,6-dimethylnaphthalene of 3.39 area%, 1-ethyl-naphthalene of 2.64 area% were found at a temperature
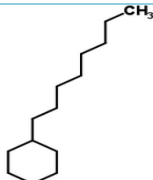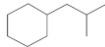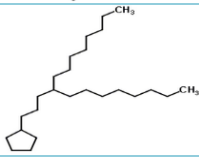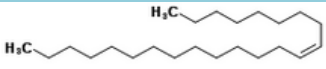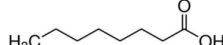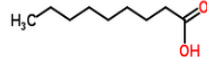
of 400 °C. In fact, aromatics increased with the increasing reaction temperature. This suggests that aromatization reaction on olefin occurred with the presence of HZSM-5 zeolite, as reported by Pinto *et al.* (2014). The cycloparaffins also indicated the functionality of acidic site on HZSM-5. As stated by a previous study (Chen *et al.*, 2016), the acidity of HZSM-5 zeolite decreased with the increase of active metal loading and Si/Al ratio. In addition, the H_2 to oil ratio would help the process of hydrogenation on olefins to n-paraffins. The determination of hydrocarbon composition and the degree of isomerization is useful to provide information to evaluate the properties of biofuel, such as cetane number (Kim *et al.*, 2013), freezing point, flash point and viscosity (Liu *et al.*, 2015).

Table 4 shows the components containing abundant compounds in biofuel based on group of hydrocarbons at a temperature of 350 °C. The main compound of cycloparaffin was cyclohexane with branched chain resulting in hydrogenation reaction of unsaturated hydrocarbon compounds, as found by Zheng *et al.* (2015). The n-hexadecanoic acid was formed greatly. It was indicated that the saturation of the double bond occurr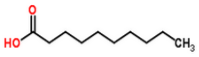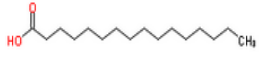ed quite well. The presence of oxygen-containing compounds showed that it would be better for hydrodeoxygenation reaction to occur at temperatures above 350 °C. Oxygen-containing compounds decreased from 8.69 to 4.33% at 350 and 400 °C, respectively. The increase of temperature led to the increasing cracking activity.

Table 4. Several abundant compounds in each group for biofuel produced at 350 °C, under 20 bar in the batch reactor* with Ni(5.43%)-Zn(1.23%)/HZSM-5 catalyst.

Compounds	Area%	Structure
Saturated chain hydrocarbon/n-paraffin		
Dodecane/$C_{12}H_{26}$	0.72	
Tridecane/$C_{13}H_{28}$	1.09	
Tetradecane/$C_{14}H_{30}$	1.78	
Pentadecane/$C_{15}H_{32}$	14.14	
Hexadecane/$C_{16}H_{34}$	2.06	
Heptadecane/$C_{17}H_{34}$	13.06	
Octadecane/$C_{18}H_{38}$	2.47	
Nonadecane/$C_{19}H_{40}$	3.05	
Heneicosane/$C_{21}H_{44}$	2.13	
Tricosane	0.76	
Tetracosane	0.77	
Aromatic hydrocarbon		
n-octylbenzene	0.89	
(5-Methyloctyl) benzene	1.13	
Cycloparaffin/Saturated naphthene		
1,1,3-trimethylcyclohexane	2.36	
Heptylcyclohexane	3.18	
1-(cyclohexylmethyl)-2-methylcyclohexane	0,5	
Cyclohexane, 1-(1,5-dimethylhex.	0.54	
		Continue…

n-octylcyclohexane	0.76	
(2-metyhlpropyl) cyclohexana	0.48	
(4-octyldodecyl) cyclopentane	1.81	
Cyclotetradecane	0.22	
1,7,11-trimet cyclotetradecane	1.27	
Cyclopentadecane	0.3	
Olefin		
8-Heptadecene	9.78	
1-Heptadecene	2.44	
9-Tricosene	0.42	
1-Hexacosene	0.64	
Carboxylic acid		
Octanoic Acid	0.72	
Nonanoic acid	1.44	
9-Octadecenoic acid	0.34	
n-Decanoic Acid/ $C_{10}H_{20}O_2$	2.7	
n-Hexadecanoic acid	10.28	
Compounds containing oxygen		
3-methyl-2,6-dioxo-4-hexenoic acid	0.9	
Cyclopentadecanone	1.59	
Octacosanol	6.2	

*Adopted from table format in literature Zheng *et al.* (2015).

As shown in Tab. 4, the presence of pentadecane (C15) and heptadecane (C17) indicated that HDC was the more dominant reaction pathway than HDO. Although two of these reactions allowed the formation of n-paraffin, but the H_2 supplied for both reaction routes was different so that n-paraffin produced was different based on the number of carbons (Pinto *et al.*, 2014; Sotelo-Boyás *et al.*, 2012; Zheng *et al.*, 2015). Hydrogenation process on *Cerbera manghas* oil containing tripalmitin proceeded to obtain three palmitic acids and propane. By following the route of decarboxylation and/or decarbonylation without going through the saturation of the first double bond by hydrogenation reaction, pentadecane ($C_{15}H_{32}$) was

immediately produced. In fact, the highest triglycerides in *Cerbera manghas* oil were triolein. Triolein was hydrogenated to obtain three oleic acids and propane. It still contained a double bond, so the hydrogenation process on oleic acid into stearic acid occurred. By following the route of decarboxylation and/or decarbonylation, stearic acid was converted into heptadecane ($C_{17}H_{36}$). Furthermore, the aromatic compounds were produced through dehydrogenation process on olefin, i.e., the cracking and aromatization reactions as reported by Zheng *et al.* (2015).

With Ni(5.42%)-Zn(1.11%)/HZSM-5 catalyst, the highest yield for n-paraffin was found at a temperature of 375 °C. On the other hand, isoparaffin reaches the

highest value of 4.58 area% at 400 °C (Roesyadi *et al.*, 2016). A single type of methyl isomer was obtained as isomerization product at 400 °C, as shown in Tab. 5. This is similar to the result obtained by Chen *et al.* (2016), who reported that the short-branched isoparaffins were formed because methyl alkanes can pass easily through the HZSM-5 pore. Ethyl isomers cannot be found because the molecular size of ethyl alkanes is larger than that of methyl alkanes. Isoparaffin increased significantly with the increasing reaction temperature because the literature (Chen *et al.*, 2016) stated that isomerization reaction proceeded in endothermic condition.

Table 5. Several abundant compounds in each group for biofuel produced at 400 ºC, under 20 bar in the batch reactor*, using Ni(5.42%)-Zn(1.11%)/HZSM-5 catalyst.

Compounds	Area%	Structure
Saturated chain hydrocarbon/n-paraffin		
Undecane/$C_{11}H_{24}$	0.48	
Dodecane/$C_{12}H_{26}$	2.84	
Tridecane/$C_{13}H_{28}$	4.2	
Tetradecane/$C_{14}H_{30}$	4.45	
Pentadecane/$C_{15}H_{32}$	13.17	
Hexadecane/$C_{16}H_{34}$	2.91	
Heptadecane/$C_{17}H_{34}$	8.85	
Octadecane/$C_{18}H_{38}$	1.7	
Nonadecane/$C_{19}H_{40}$	1.42	
Tricosane	0.27	
Isoparaffin		
3-Methylheptadecane	1.72	
6,9-Dimethyltetradecane	0.9	
2,6,10,14-Tetramethyloctadecane	1.58	
3,8-Dimethyldecane	0.38	
Aromatic hydrocarbon		
Phenyloctane /N-Octylbenzene	1.03	
Nonylbenzene	1.31	
Pentylbenzene	0.78	
(1,3-Dimethylbutyl) Benzene	0.31	
1-Methyl-2-N-Hexylbenzene	0.57	
1-Methylnaphthalene	2.22	
2-Ethylnaphthalene	0.66	
1-Ethyl-2,3-dimethylbenzene/o-Xylene	0.05	

Continue…

2-methyl-1-propenylbenzene	0.39	
Cycloparaffin/Saturated naphthene		
n-Nonylcyclohexane	1.26	
1-(1,5-Dimethylhexyl)-4-(4-methyl pentyl) cyclohexane	3.42	
1-Hexyl-3-methylcyclopentane	0.54	
(4-Methylpentyl) cyclohexane	0.46	
1,2-Dicyclohexylethane	1.35	
1,1,3-Trimethylcyclohexane	0.62	
7-cyclohexyltridecane	0.11	
Dicyclohexylmethane	0.68	
2,3-Dihydro-4-methyl-1H-indene	0.7	
Olefin		
8-Heptadecene	4.66	
1-Heptadecene	0.48	
1-Docosene	0.13	
Carboxylic acid		
Octanoic Acid	0.95	
Nonanoic acid	2.12	
n-Decanoic Acid/ $C_{10}H_{20}O_2$	2	
n-Hexadecanoic acid/palmitat acid	8.74	
Tetradecanoic acid	2.09	
Compounds containing oxygen		
2-Nonadecanone	1	
2-hydroxydodecanoic acid ethyl ester	0.35	
2-Heptadecanone/Methyl pentadecyl ketone	1.66	
beta-octyl acrolein	0.7	
1-Oxa-2-cyclohexadecanone	0.37	

*Adopted from table format in literature Zheng *et al.* (2015).

With the increasing reaction temperature, aromatics increased significantly so that n-paraffin (including C15 and C17) and cycloparaffins also decreased for Ni(5.43%)-Zn(1.23%)/HZSM-5 catalyst (Fig. 8a). It indicated that aromatization and cyclization reaction were favored at temperatures over 350 °C (Rocha Filho

et al., 1993). According to Šimáček *et al.* (2009; 2011), aromatics also increased because of the increasing cyclization reactions rate. Tamiyakul *et al.* (2016) also reported that the presence of Zn^{2+} and ZnO detected in HZSM-5 was responsible for n-paraffins dehydrogenation and oxygenates decarboxylation, respectively. As a result, more aromatic yield was produced.

3.3.2 Effect of temperature on gasoline/kerosene/gasoil yields

Gas chromatography-mass spectrometry spectra of biofuel produced was compared to the GC-MS spectra of petroleum fuel (Rasyid *et al.*, 2015). The liquid product was identified based on hydrocarbon compounds obtained from the GC-MS analysis. Then, the identified hydrocarbon was grouped as gasoline-like hydrocarbon (C5-C9), kerosene-like hydrocarbon (C10-C13), and gasoil-like hydrocarbon (C14-C22), as reported by Barrón *et al.* (2011). Figure 8b shows gasoline/kerosene/gasoil yields for biofuel produced over Ni(5.43%)-Zn(1.23%)/HZSM-5 catalyst, with reaction temperatures in the range of 350–400 °C.

As confirmed by Fig. 8b data, the various reaction temperatures will affect gasoil/kerosene yields. As a result, gasoil yield decreased, and kerosene yield increased with the increase of temperature. This suggests that the decline in the yield of gasoil due to hydrocracking of long chain hydrocarbons into shorter chain was random reaction mechanism, as reported in a previous study (Kim *et al.*, 2013). It is also presented in Fig. 8b that the highest gasoline and kerosene yields were obtained at 400 °C at 5.13 and 16.42%, respectively. Meanwhile, gasoil yield of 15.12% was obtained at 350 °C. Gasoil decreased with the increase of reaction temperature for two type catalyst, which can be seen in Fig. 8b and c.

If Fig. 8b and c are compared based on the yield of gasoil, the characteristic performance of the Ni(5.42%)-Zn(1.11%)/HZSM-5 catalyst is higher than that of the Ni(5.43%)-Zn(1.23%)/HZSM-5 catalyst. The Ni(5.43%)-Zn(1.23%)/HZSM-5 catalyst leads to the formation of gasoline and kerosene with increasing temperature. For the Ni(5.43%)-Zn(1.23%)/HZSM-5 catalyst, liquid hydrocarbon products in the kerosene range have been produced at 350 °C with several abundant compounds shown in Tab. 4. For Ni(5.42%)-Zn(1.11%)/HZSM-5, liquid hydrocarbon products in the kerosene/gasoline range were only produced at 400 °C with several abundant compounds, as shown in Tab. 5.

Differences in reaction temperature affect the constituent of hydrocarbons in biofuel produced. With Ni(5.43%)-Zn(1.23%)/HZSM-5 catalyst, at a temperature of 350 °C kerosene contained n-paraffin, i.e., dodecane, n-octylcyclohexane, n-octylbenzene, and pentadecane, while gasoil contained hydrocarbon compound, i.e., heptadecane, octadecane, nonadecane, heneicosane, (5-Methyloctyl) benzene, heptylcyclohexane, 1-(cyclohexylmethyl)-2-methylcyclohexane, and cyclopentadecane. Meanwhile, at reaction temperature of 400 °C, the higher gasoline yield was obtained with composition, i.e., 1,3-diethyl-5-methylbenzene, 1-methyl-2-(2-propenyl) benzene, 1,4-dimethyl-dihydro-azulene, and 1-methyl-3-(1-methylethyl) benzene. In principle, the presence of aromatics increases octane number in gasoline. Previously, the hydrocracking of *Calophyllum inophyllum* oil has been done to produce gasoline of 25.63%, kerosene of 17.31% and gasoil of 38.59% with CoMo(10%)/γ-Al$_2$O$_3$ catalyst at 350 °C under pressure of 30 bar (Rasyid *et al.*, 2015).

4. Conclusions

The influence of the reaction temperature in hydrocracking on *Cerbera manghas* oil into biofuel with a catalyst Ni-Zn/HZSM-5 has been studied. The amount of n-paraffin decreased with the increasing temperature and followed by the increase of cycloparaffins and aromatics. This increasing reaction temperature led to an increase in the activity of cracking on a longer carbon chain molecule into a shorter carbon chain molecule. With Ni(5.43%)-Zn(1.23%)/HZSM-5 catalyst, highest kerosene was obtained at a temperature of 400 °C. At the same temperature, the higher isoparaffins contained the short-branched isoalkanes in gasoil were detected when the Ni(5.42%)-Zn(1.11%)/HZSM-5 catalyst was used. Therefore, reaction routes during hydrocracking are influenced by the reaction temperature and catalyst composition of Ni-Zn/HZSM-5, which provides acid function and metal function.

Authors' contribution

Conceptualization: Marlinda, L.; Danawati, H. P.
Data curation: Marlinda, L.
Formal Analysis: Marlinda, L.
Funding acquisition: Marlinda, L.; Danawati, H. P.
Investigation: Marlinda, L.; Danawati, H. P.; Roesyadi, A.; Gunardi, I.; Mirzayanti, Y. W.; Al Muttaqii, M.; Budianto, A.

Data availability statement

All data sets were generated or analyzed in the current study.

Funding

Acknowledgments

References

Arun, N.; Sharma, R. V.; Dalai, A. K. Green diesel synthesis by hydrodeoxygenation of bio-based feedstocks: Strategies for catalyst design and development. *Renew. Sustain. Energy Rev.* **2015**, *48*, 240–255. https://doi.org/10.1016/j.rser.2015.03.074

Ayodele, O. B.; Farouk, H. U.; Mohammed, J.; Uemura, Y.; Daud W. M. A. W. Hydrodeoxygenation of oleic acid into n- and iso-paraffin biofuel using zeolite supported fluor-oxalate modified molybdenum catalyst: Kinetics study. *J. Taiwan Inst. Chem. Eng.* **2015**, *50*, 142–152. https://doi.org/10.1016/j.jtice.2014.12.014

Barrón, C. A. E.; Melo-Banda, J. A.; Dominguez, J. M. E.; Hernández, M. E.; Silva, R. R.; Reyes, T. A. I.; Meraz, M. M. A. Catalytic hydrocracking of vegetable oil for agrofuels production using Ni–Mo, Ni–W, Pt and TFA catalysts supported on SBA-15. *Catal. Today* **2011**, *166* (1), 102–110. https://doi.org/10.1016/j.cattod.2011.01.026

Bezergianni, S.; Dimitriadis, A.; Meletidis, G. Effectiveness of CoMo and NiMo catalysts on co-hydroprocessing of heavy atmospheric gas oil–waste cooking oil mixtures. *Fuel* **2014**, *125*, 129–136. https://doi.org/10.1016/j.fuel.2014.02.010

Bockisch, M. *Fats and Oils Handbook*; AOCS Press, **1998**. https://doi.org/10.1016/B978-0-9818936-0-0.50003-2

Budianto, A.; Prajitno, D. H.; Budhikarjono, K. Biofuel production from candlenut oil using catalytic cracking process with Zn/HZSM-5 catalyst. *ARPN J. Eng. Appl. Sci.* **2014a**, *9* (11), 2121–2124.

Budianto, A.; Danawati H. P.; Roesyadi, A.; Budhikarjono, K. HZSM-5 catalyst for cracking palm oil to biodiesel: A Comparative study with and without Pt and Pd impregnation. *Scientific Study & Research: Chemistry & Chemical Engineering, Biotechnology, Food Industry* **2014b**, *15* (1): 81–90.

Carlier, J.; Guitton, J.; Bévalot, F.; Fanton, L.; Gaillard. Y. The principal toxic glycosidic steroids in *Cerbera manghas* L. seeds: Identification of cerberin, neriifolin, tanghinin and deacetyltanghinin by UHPLC–HRMS/MS, quantification by UHPLC–PDA-MS. *J. Chromatogr. B* **2014**, *962*, 1–8. https://doi.org/10.1016/j.jchromb.2014.05.014

Chen, X.; Dong, M.; Niu, X.; Wang, K.; Chen, G.; Fan, W.; Wang, J.; Qin, Z. Influence of Zn species in HZSM-5 on ethylene aromatization. *Chin. J. Catal.* **2015**, *36* (6), 880–888. https://doi.org/10.1016/S1872-2067(14)60289-8

Chen, L.; Li, H.; Fu, J.; Miao, C.; Lv, P.; Yuan, Z. Catalytic hydroprocessing of fatty acid methyl esters to renewable alkane fuels over Ni/HZSM-5 catalyst. *Catal. Today* **2016**, *259* (Part 2), 266–276. https://doi.org/10.1016/j.cattod.2015.08.023

Chuah, L. F.; Yusup, S.; Aziz, A. R. A.; Klemeš, J. J.; Bokhari, A.; Abdullah, M. Z. Influence of fatty acids content in non-edible oil for biodiesel properties. *Clean Techn. Environ. Policy* **2016**, *18*, 473–482. https://doi.org/10.1007/s10098-015-1022-x

Dwivedi, G.; Sharma, M. P. Application of Box-Behnken design in optimization of biodiesel yield from Pongamia oil and its stability analysis. *Fuel* **2015**, *145*, 256–262. https://doi.org/10.1016/j.jiec.2012.03.019

Haber, J.; Block, J. H.; Delmon, B. Manual of methods and procedures for catalyst characterization. *Pure & Appl. Chem.* **1995**, *67* (Nos 8/9), 1257–1306. https://doi.org/10.1351/pac199567081257

Hao, K.; Shen, B.; Wang, Y.; Ren, J. Influence of combined alkaline treatment and Fe–Ti-loading modification on ZSM-5 zeolite and its catalytic performance in light olefin production. *J. Ind. Eng. Chem.* **2012**, *18* (5), 1736–1740. https://doi.org/10.1016/j.jiec.2012.03.019

Isahak, W. N. R. W.; Hisham, M. W. M.; Yarmo, M. A.; Hin, T.-y. Y. A review on bio-oil production from biomass by using pyrolysis method. *Renew. Sustain. Energy Rev.* **2012**, *16* (8), 5910–5923. https://doi.org/10.1016/j.rser.2012.05.039

Ishihara, A.; Fukui, N.; Nasu, H.; Hashimoto, T. Hydrocracking of soybean oil using zeolite-alumina composite supported NiMo catalyst. *Fuel* **2014**, *134*, 611–617. https://doi.org/10.1016/j.fuel.2014.06.004

Kim, S. K.; Brand, S.; Lee, H.-s.; Kim, Y.; Kim, J. Production of renewable diesel by hydrotreatment of soybean oil: Effect of reaction parameters. *Chem. Eng. J.* **2013**, *228*, 114–123. https://doi.org/10.1016/j.cej.2013.04.095

Li, L.; Quan, K.; Xu, J.; Liu, F.; Liu, S.; Yu, S.; Xie, C.; Zhang, B.; Ge, X. Liquid hydrocarbon fuels from catalytic cracking of rubber seed oil using USY as catalyst. *Fuel* **2014**, *123*, 189–193. https://doi.org/10.1016/j.fuel.2014.01.049

Liu, S.; Zhu, Q.; Guan, Q.; He, L.; Li, W. Bio-aviation fuel production from hydroprocessing castor oil promoted by the nickel-based bifunctional catalysts. *Bioresour. Technol.* **2015**, *183*, 93–100. https://doi.org/10.1016/j.biortech.2015.02.056

Lu, Q.; Li, W.-Z.; Zhu, X.-F. Overview of fuel properties of biomass fast pyrolysis oils. *Energy Convers. Manag.* **2009**, *50* (5), 1376–1383. https://doi.org/10.1016/j.enconman.2009.01.001

Marlinda, L.; Al-Muttaqii, M.; Roesyadi, A.; Prajitno, D. H. Production of biofuel by hydrocracking of *Cerbera Manghas* oil using Co-Ni/HZSM-5 catalyst: Effect of reaction temperature. *J. Pure App. Chem. Res.* **2016**, *5* (3), 189–195. https://doi.org/10.21776/ub.jpacr.2016.005.03.254

Niu, X.; Gao, J.; Miao, Q.; Dong, M.; Wang, G.; Fan, W.; Qin, Z.; Wang, J. Influence of preparation method on the performance of Zn-containing HZSM-5 catalysts in methanol-to-aromatics. *Microporous Mesoporous Mater.* **2014**, *197*, 252–261. https://doi.org/10.1016/j.micromeso.2014.06.027

Pinto, F.; Martins, S.; Gonçalves, M.; Costa, P.; Gulyurtlu, I.; Alves, A.; Mendes, B. Hydrogenation of rapeseed oil for production of liquid bio-chemicals. *Appl. Energy* **2013**, *102*, 272–282. https://doi.org/10.1016/j.apenergy.2012.04.008

Pinto, F.; Varela, F. T.; Gonçalves, M.; André Neto, R.; Costa, P.; Mendes, B. Production of bio-hydrocarbons by hydrotreating of pomace oil. *Fuel* **2014**, *116*, 84–93. https://doi.org/10.1016/j.fuel.2013.07.116

Prajitno, D. H.; Roesyadi, A.; Budianto, A.; Iqbal, M.; Purnomo, V. Modification of Ni-Zn/HZSM-5 double promoted catalyst for biofuel production from *Cerbera manghas* oil. In Green Chemistry Section 1: Material Chemistry, *Proceedings of the 9th Joint Conference on Chemistry*, Semarang, Indonesia, November 12–13, 2014; Prajitno, D. H.; Roesyadi, A.; Budianto, A.; Iqbal, M.; Purnomo, V., Eds.; Diponegoro University: Semarang, **2015**; pp 25–28.

Rasyid, R.; Prihartantyo, A.; Mahfud, M.; Roesyadi, A. Hydrocracking of *Calophyllum inophyllum* oil with non-sulfide CoMo catalysts. *Bull. Chem. React. Eng. Catal.* **2015**, *10* (1), 61–69. https://doi.org/10.9767/bcrec.10.1.6597.61-69

Rocha Filho, G. N.; Brodzki, D.; Djéga-Mariadassou, G. Formation of alkanes alkylcykloalkanes and alkylbenzenes during the catalytic hydrocracking of vegetable oils. *Fuel* **1993**, *72* (4), 543–549. https://doi.org/10.1016/0016-2361(93)90114-H

Roesyadi, A.; Hariprajitno, D.; Nurjannah, N.; Savitri, S. D. HZSM-5 Catalyst for cracking palm oil to gasoline: A comparative study with and without impregnation. *Bull. Chem. React. Eng. Catal.* **2013**, *7* (3), 185–190. https://doi.org/10.9767/bcrec.7.3.4045.185-190

Roesyadi, A. *Pembuatan Biofuel dari Minyak Nabati*; PT. Revka Petra Media, **2016**.

Roesyadi, A.; Budianto, A.; Prajitno, D. H.; Gunardi, I.; Marlinda, L. Metode Pembuatan Katalis Ni-Zn/HZSM-5 untuk Produksi Biofuel dari Minyak Bintaro (*Cerbera Manghas* Oil). ID, P00201607714**, 2016**. https://pdki-indonesia.dgip.go.id/detail/P00201607714?type=patent&keyword=bintaro (accessed 2021-12-19).

Romero, M. D.; Calles, J. A.; Rodríguez, A.; Cabanelas, J. C. The influence of calcination treatment over bifunctional Ni/HZSM-5 catalysts. *Ind. Eng. Chem. Res.* **1998**, *37* (10), 3846–3852. https://doi.org/10.1021/ie980143i

Romero, M.; Pizzi, A.; Toscano, G.; Casazza, A. A.; Busca, G.; Bosio, B.; Arato, E. Preliminary experimental study on biofuel production by deoxygenation of Jatropha oil. *Fuel Process. Technol.* **2015**, *137*, 31–37. https://doi.org/10.1016/j.fuproc.2015.04.002

Santillan-Jimenez E.; Crocker, M. Catalytic deoxygenation of fatty acids and their derivatives to hydrocarbon fuels via decarboxylation/decarbonylation. *J. Chem. Technol. Biotechnol.* **2012**, *87* (8), 1041–1050. https://doi.org/10.1002/jctb.3775

Sartipi, S.; Parashar, K.; Valero-Romero, M. J.; Santos, V. P.; van der Linden, B.; Makkee, M.; Kapteijn, F.; Gascon, J. Hierarchical H-ZSM-5-supported cobalt for direct synthesis of gasoline-range hydrocarbon from syngas: Advantages, limitation, and mechanistic insight. *J. Catal.* **2013**, *305*, 179–190. https://doi.org/10.1016/j.jcat.2013.05.012

Silva, V. T.; Sousa, L. A. Catalytic upgrading of fats and vegetable oils for the production of fuels. In *The role of catalysis for the sustainable production of bio-fuels and bio-chemicals*; Elsevier Science; **2013**, pp 67–92. https://doi.org/10.1016/B978-0-444-56330-9.00003-6

Šimáček, P.; Kubička, D.; Šebor, G.; Pospíšil, M. Hydroprocessed rapeseed oil as a source of hydrocarbon-based biodiesel. *Fuel* **2009**, *88* (3), 456–460. https://doi.org/10.1016/j.fuel.2008.10.022

Šimáček, P.; Kubička, D.; Kubičková, I.; Homola, F.; Pospíšil, M.; Chudoba, J. Premium quality renewable diesel fuel by hydroprocessing of sunflower oil. *Fuel* **2011**, *90*, 2473–2479. https://doi.org/10.1016/j.fuel.2011.03.013

Sotelo-Boyás, R.; Trejo-Zárraga, F.; Hernández-Loyo, F. J. Hydroconversion of triglycerides into green liquid fuels. In *Hydrogenation*; IntechOpen, 2012; pp 187–216. https://doi.org/10.5772/48710

Tamiyakul, S.; Anutamjarikun, S.; Jongpatiwut, S. The effect of Ga and Zn over HZSM-5 on the transformation of palm fatty acid distillate (PFAD) to aromatics. *Catal. Commun.* **2016**, *74*, 49–54. https://doi.org/10.1016/j.catcom.2015.11.002

Vichaphund, S.; Aht-ong, D.; Sricharoenchaikul, V.; Atong, D. Production of aromatic compounds from catalytic fast pyrolysis of Jatropha residues using metal/HZSM-5 prepared by ion-exchange and impregnation methods. *Renew. Energy* **2015**, *79*, 28–37. https://doi.org/10.1016/j.renene.2014.10.013

Vitale, G.; Molero, H.; Hernandez, E.; Aquino, S.; Birss, V.; Pereira-Almao, P. One-pot preparation and characterization of bifunctional Ni-containing ZSM-5 catalyst. *Appl. Catal. A: Gen.* **2013**, *452*, 75–87. https://doi.org/10.1016/j.apcata.2012.11.026

Wang, S.; Yin, Q.; Guo, J.; Ru, B.; Zhu, L. Improved Fischer-Tropsch synthesis for gasoline over Ru, Ni promoted Co/HZSM-5 catalyst. *Fuel* **2013**, *108*, 597-603. https://doi.org/10.1016/j.fuel.2013.02.021

Wang, C.; Liu, Q.; Song, J.; Li, W.; Li, P.; Xu, R.; Ma, H.; Tian, Z. High quality diesel-range alkanes production via a single-step hydrotreatment of vegetable oil over Ni/zeolite catalyst. *Catal. Today* **2014**, *234*, 153–160. https://doi.org/10.1016/j.cattod.2014.02.011

Wu, L.; Guo, S.; Wang, C.; Yang Z. Production of alkanes (C_7–C_{29}) from different part of poplar tree via direct deoxy-liquefaction. *Bioresour. Technol.* **2009**, *100* (6), 2069–2076. https://doi.org/10.1016/j.biortech.2008.10.024

Zhang, H.; Lin, H.; Zheng, Y. The role of cobalt and nickel in deoxygenation of vegetable oils. *Appl. Catal. B: Environ.* **2014**, *160–161*, 415–422. https://doi.org/10.1016/j.apcatb.2014.05.043

Zheng, X.; Chang, J.; Fu, Y. One-pot catalytic hydrocracking of diesel distillate and residual oil fractions obtained from bio-oil to gasoline-range hydrocarbon fuel. *Fuel* **2015**, *157*, 107–114. https://doi.org/10.1016/j.fuel.2015.05.002

Theoretically studying the optoelectronic properties of oligomers based on 2.7-divinyl-cabazole

Mohamed Jabha[1, 2+], Abdellah El Alaoui[3], Abdellah Jarid[2], El Houssine Mabrouk[1,4]

1. University of Moulay Ismail, Faculty of Sciences and Technics, Errachidia, Morocco.
2. University of Cadi Ayyad, Faculty of Sciences Semlalia, Marrakech, Morocco.
3. University of Moulay Ismail, Faculty of Sciences, Meknes, Morocco.
4. Sidi Mohamed Ben Abdellah University, Faculty of Sciences, Fez, Morocco.

+Corresponding author: Mohamed Jabha, Phone: +212614018410, Email address: m.jabha@edu.umi.ac.ma

ABSTRACT: This work consists of theoretically studying the electronic and optical properties of 9-(4-octyloxyphenyl)-2.7-divinyl-carbazole (PCrV) oligomers. This study has been undertaken using the density functional theory (DFT) method at the B3LYP/6-31G (d,p) level and BP86/6-31G (d,p) level of theory. To evaluate the PCrV-basis systems properties, the structural optimization without geometrical restrictions was performed on the total potential energy surface (TPES). In order to ensure good absorption of radiation, the interest was in increasing the efficiency of the organic photovoltaic cell. For this effect, the (HOMO-LUMO) gap energy of such compounds was reduced in terms of geometric and electronic structure. The BP86 functional gives good results at the energy gap level, while other parameters using the B3LYP functional give the best results.
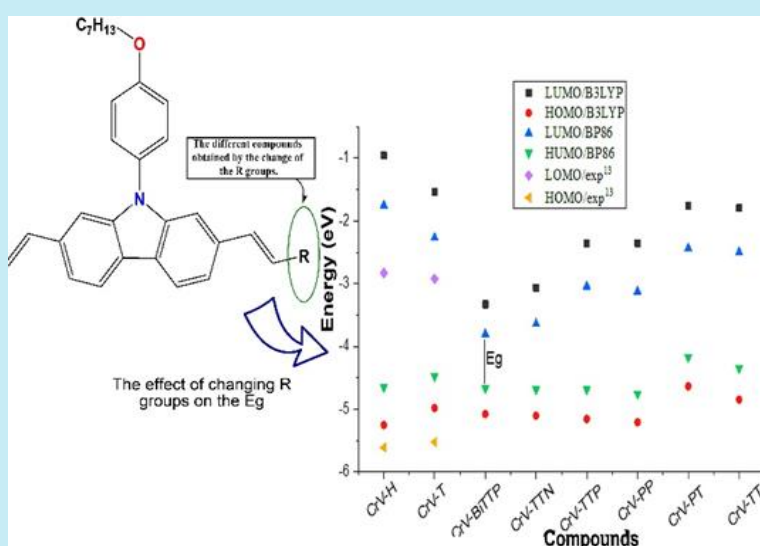
1. Introduction

The growing energy needs of daily lives on the one hand, and the strong growth of the world population on the other are leading to a search for new sources of energy (hydroelectricity, wind, sun), as well as the mastery of materials with new properties (semiconductors, aluminum, composites, rare earths, etc...). In addition to the speed of technological development, especially plastic-based technology, and the development of computational performance, facilitates he realization of new organic materials, the discovery and improvement of new properties of semiconductor organic materials, and the expansion of the field of use, especially in the field of photovoltaic (Baek *et al.*, 2012; Bourass *et al.*, 2017; Toub, 2007).

Polymeric (Fukuta *et al.*, 2015; Huang, 2015; Scharber and Sariciftci, 2013) (organic) solar cells are becoming more and more important in the field of scientific research. These cells have many potential advantages over inorganic solar cells (Koh *et al.*, 2008; Tarascon, 2011; Zeyada *et al.*, 2016), such as relatively low cost, lightweight, interesting electronic properties, good mechanical properties and ease of processing. However, the main limitations of this type are the low power-to-energy conversion efficiency and the relative instability compared to silicon-based solar cells. However, this efficiency depends on highest occupied molecular orbital (HOMO), lowest unoccupied molecular orbital (LUMO), and energy gap properties.

Derivatives of 2.7-carbazole (Blouin *et al.*, 2008; Chen *et al.*, 2014; Zhao *et al.*, 2010) are organic materials (these oligomers) possessing the properties of a semiconductor, known by their high stability due to the presence of nitrogen atoms, by their wide range of industrial applications thanks to their important physicochemical property. The addition of alkyl chains on the nitrogen atom increases the solubility, which facilitates the synthesis of these oligomers.

The interest is in increasing the efficiency of the organic photovoltaic cell, seeking to decrease the gap energy (HOMO-LUMO), to characterize these compounds in terms of geometrical and electronic structures to ensure a good absorption of radiation.

This work consists in theoretically studying the electronic and optical properties of oligomers based on 9-(4-octyloxyphenyl)-2.7-divinylcabazole (PCrV) (Fig. 1) using the density functional theory (DFT) method under two different functionals with the same base (6-31G [d,p]). The optical properties are obtained by the time-dependent density functional theory (TD-DFT) method, in order to show the reliability of one of these functionals, and their fairness with the experimental results (Leclerc *et al.*, 2006).
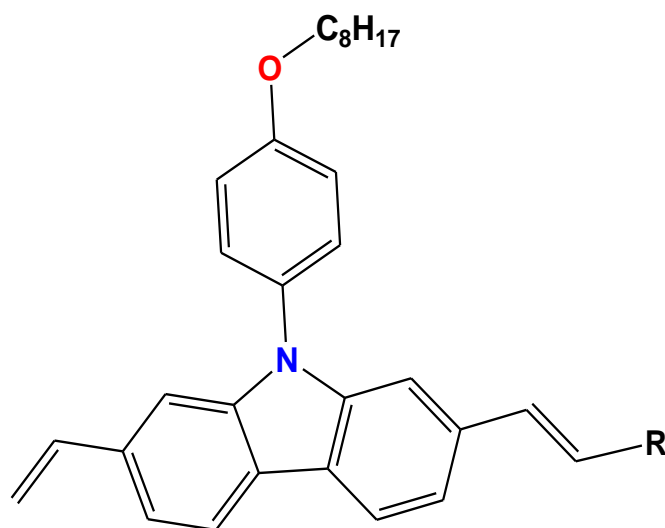

Figure 1. 9-(4-octyloxyphenyl)-2.7-divinylcabazole.

The calculated band gap energy of these oligomers is between 0.87 eV and 2.9 eV at the BP86/6-31G (d,p) base of the DFT method, while at the B3LYP/6-31G (d,p) base of the same method the gap energy is between 1.75 eV and 3.86 eV. However, the experimental gap energy is 2.8 eV. Absorption properties, optical properties and electron density are also studied.

1.1 The studied systems

The basic molecule 9-(4-octyloxyphenyl)-2.7-divinylcabazole was chosen, to which was linked a radical R, which was changed to obtain the different systems studied. The different R groups were introduced to study their effects on the electronic structure and on the optoelectronic properties. Below are the structures of the R groups and the abbreviation of different oligomers (Fig. 2).
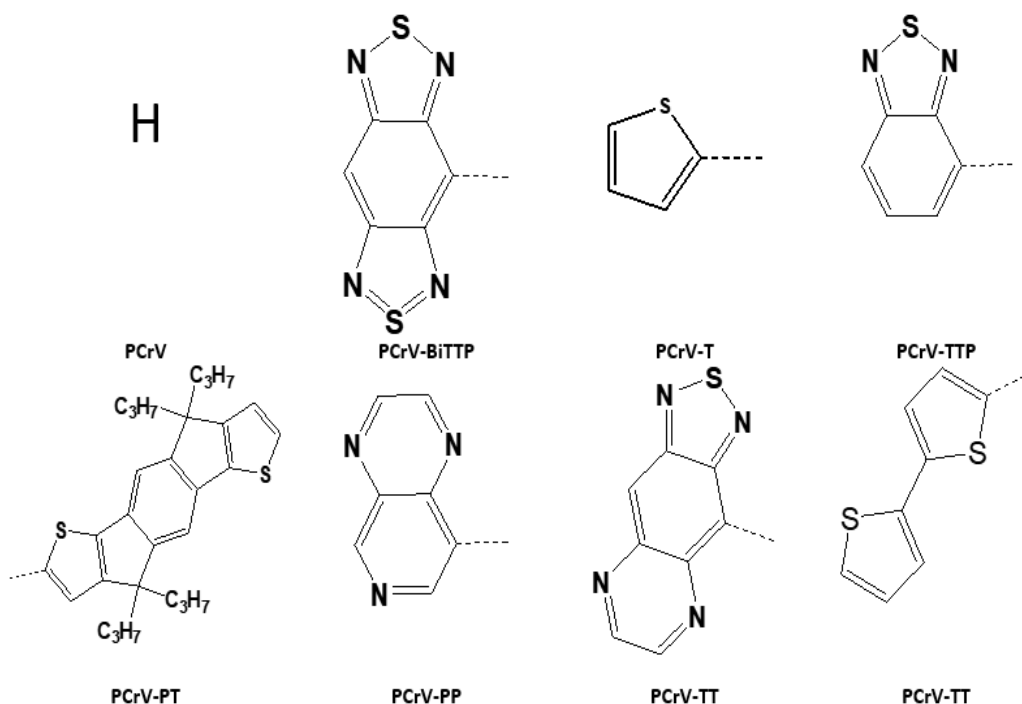
Figure 2. Structures and symbol of the R groups.

2. Methodology and computational details

Theoretical calculations of all oligomers were performed without constraint, using the Gaussian 09 software (Gaussian, 2009). The geometrical study of neutral systems in its fundamental state, optimization and frequency was evaluated using the functional density theory (DFT) (Baseden and Tye, 2014; Ganji *et al.*, 2016; Garrity *et al.*, 2014), under the B3LYP functional (Becke, three-parameter, Lee–Yang–Parr) (Becke, 1988; Gill *et al.*, 1992; Xu and Goddard, 2004) and the Becke Perdew hybrid (BP86) (Cai *et al.*, 2002; Cramer and Truhlar, 2009) functional with the base 6.31G (d, p) (Francl *et al.*, 1982; Mitin *et al.*, 2003; Nishiyama *et al.*, 1975) for all atoms.

The geometrical structures of the neutral molecules were optimized without constraints, the convergence of all calculations was confirmed by the absence of negative frequencies.

The energy levels HOMO, LUMO (gap energy) are calculated from the optimized structures. Photovoltaic parameters are obtained from the optimized geometries. In order to calculate the optical properties by the TD-DFT method (Boussaidi *et al.*, 2016; Jacquemin *et al.*, 2009; Laurent and Jacquemin, 2013), with the two functionals (B3LYP and BP86) at the atomic base 6-31G (d,p) from the optimized structures under the same functionals.

3. Results and discussion

3.1 Geometrical study

The geometrical study of the oligomers carried out at the level of the functionals B3LYP and BP86 of the DFT method under the atomic base 6-31G (d,p). The grafting of the R groups increasing the number of atoms of each oligomer causes the total energy of each system to decrease, i.e., the oligomers stabilize more and more. Table 1 and Fig. 3 describe the structural parameters with the two functionals. Nomenclature, abbreviations, and symbols should follow International Union of Pure Applied Chemistry (IUPAC) recommendations.
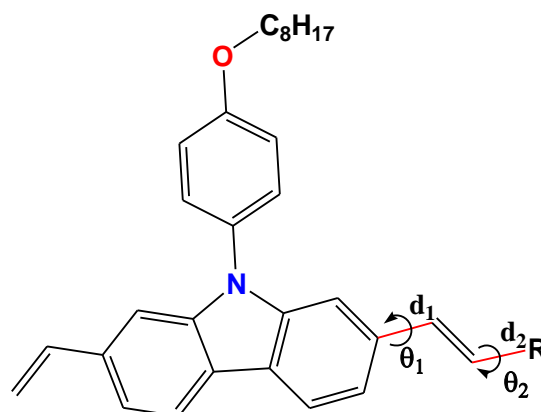

Figure 3. Dihedral angles and distances in the studied oligomers.

Note that the distances d_1 and d_2 represent, respectively, the charge transfer bridge between the donor part (D) and the spacer (vinyl) with the groups R, and q_1 and q_2 are the dihedral angles between the donor (D) and the spacer on the one hand and the groups R and the spacer on the other hand (Fig. 3). The values obtained from the optimization are grouped in Tab. 1.

Table 1. Calculated values of d_1 and d_2 bond lengths (Å) at a B3LYP/6-31G (d,p) levels and BVP86/6-31G (d,p) levels.

Compound	d_1/B3LYP	d_1/BP86	d_2/B3LYP	d_2/BP86
PCrV	1.4708	1.47077	1.08490	1.09265
PCrV-T	1.46102	1.45936	1.45015	1.44789
PCV-BiTTP	1.45462	1.45295	1.43948	1.43839
PCrV-TTN	1.45787	1.45577	1.44906	1.44645
PCrV-TTP	1.46087	1.45906	1.45838	1.45642
PCrV-PP	1.46166	1.45959	1.45938	1.45689
PCrV-PT	1.45922	1.45701	1.44041	1.43745
PCrV-TT	1.45954	1.45736	1.44148	1.43837

According to Tab. 1, it is possible to observe that the values of the bonds obtained from the calculations do not undergo a great change, generally the lengths are close to that of carbon-carbon (1.48 Å). In resonance, especially the values obtained by the B3LYP functional, the d2 bond (Fig. 3) of the PCrV oligomer is a C–H single bond, and the closest value to the experimental one is that obtained by the B3LYP functional.

The introduction of the vinylene bond in the π-conjugate system (Kim *et al.*, 2016; Nazim *et al.*, 2015) is an efficient strategy to modulate the electronic properties of the systems to lower the gap energy. It is also a good method to obtain coplanar molecules due to the relatively small dihedral angle between the vinyl group and the grafted R groups (Fig. 2).

The increase in the value of the dihedral angle contributes to the loss of coplanarity between donor and acceptor. In order to exploit these geometrical and structural parameters of the studied molecules inter-nucleus distances (di) and dihedral angles (θi), the most stable conformations are obtained after optimization in their fundamental state using the DFT method. The results obtained are illustrated in Fig. 4a.
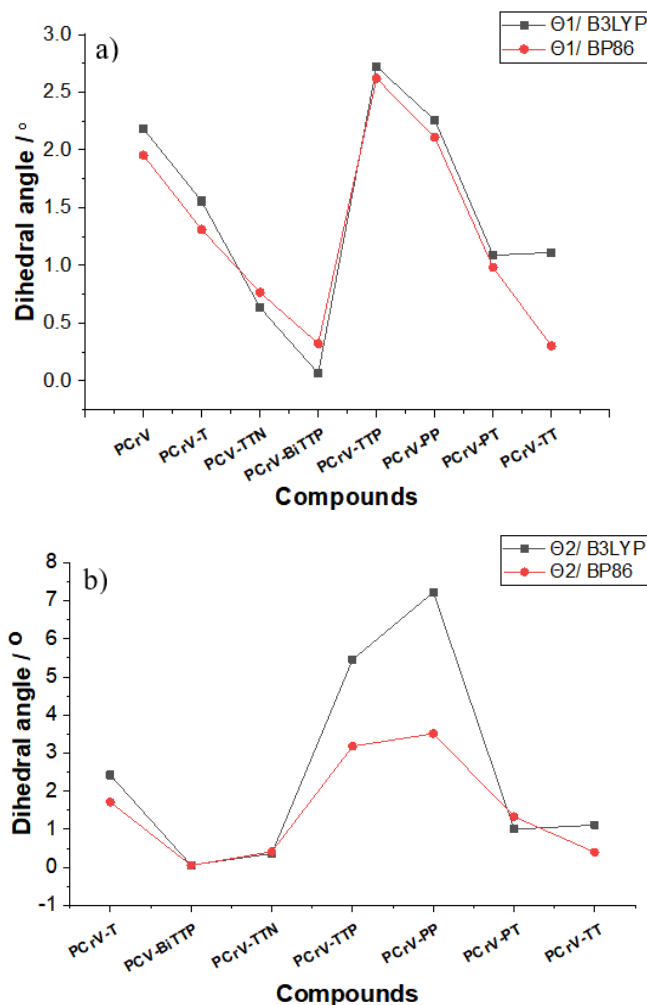

Figure 4. $θ_1$ **(a)** and $θ_2$ **(b)** dihedral angles (°) obtained by B3LYP/6-31G (d, p) levels and BP86/6-31G (d, p) levels.

It is noticed that the dihedral angle $θ_i$ between the electron donor groups and the spacer for all compounds varies between 0.5 and 2.75°. Regardless of the study functional (B3LYP and BP86) except the dihedral angle of the PCrV-BiTTP oligomer for both functionals (0.01° for the B3LYP functional and 0.35° for the BP86 functional), i.e., the PCrV-BiTTP oligomer is almost coplanar, when the geometries are optimized by the B3LYP functional. On the other hand, for both functionals (B3LYP and BP86) the values of the dihedral angle q_2 between the spacer and the R groups for the PCrV-BiTTP oligomer is 0.02° for B3LYP and 0.03 for BP86. The values of the other oligomers show that the compounds studied have a noncoplanar structure especially for compounds having the PP, TTP,

PT groups, this is probably due to the steric effect of the R groups.

3.2 Optimized structures

The optimized molecular structures are shown in Fig. 5. The structures have been optimized in its neutral state by the DFT method under the base 6-31g (d,p) with the functionals B3LYP and BP86 in order to obtain the optoelectronic and photovoltaic properties.
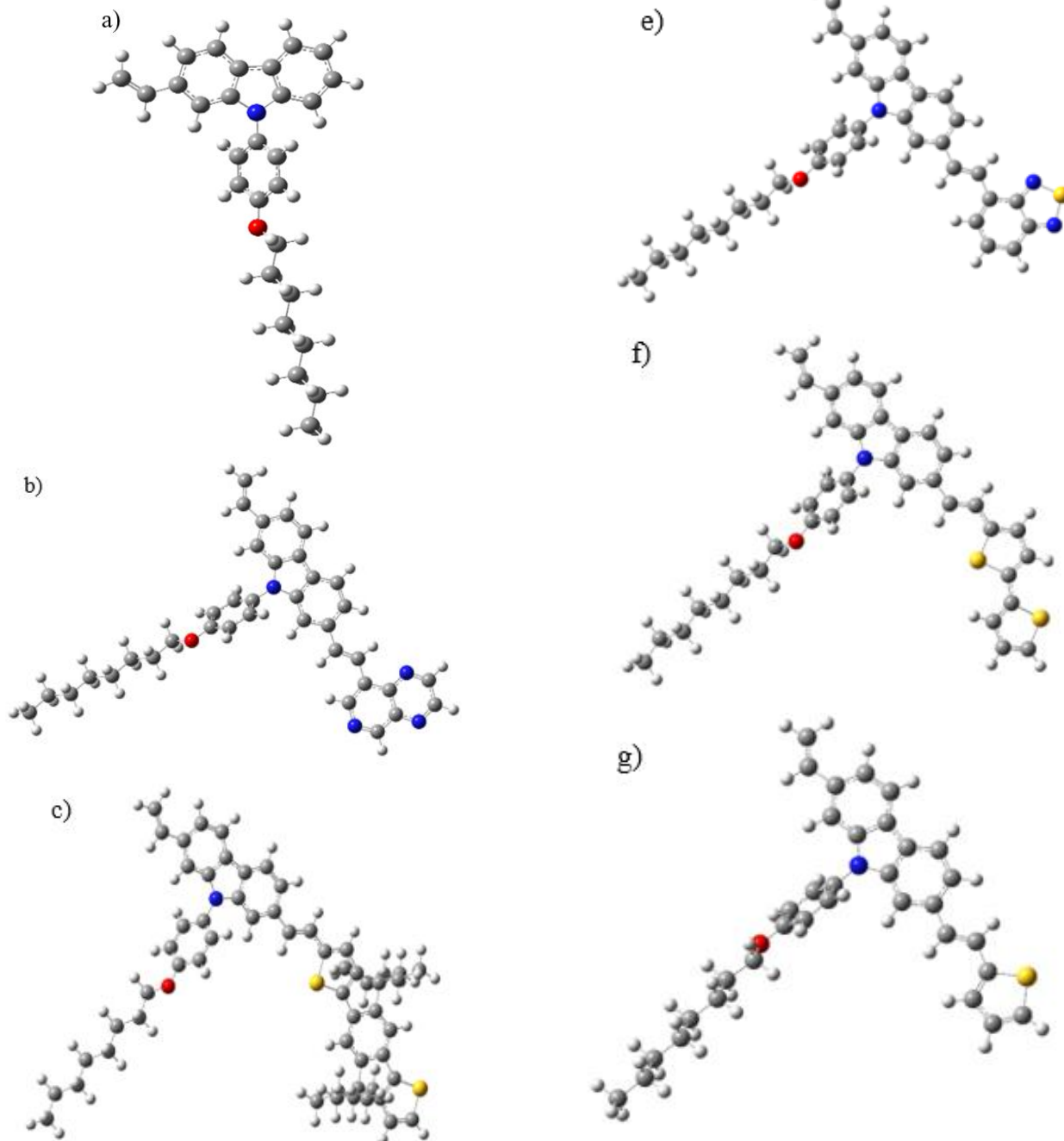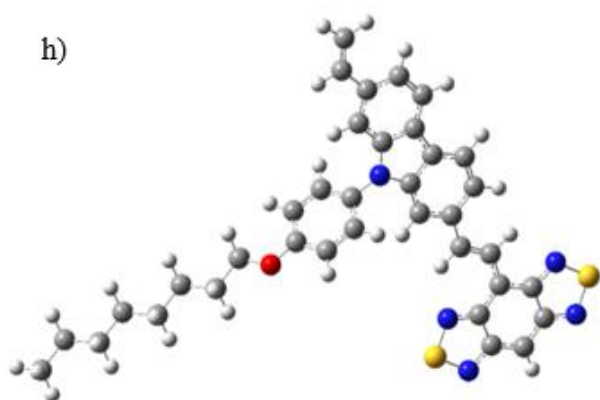
Figure 5. The most stable conformations of oligomers optimized by the DFT method. **(a)** PCrV; **(b)** PCrV-PP; **(c)** PCrV-PT; **(d)** PCrV-TTN; **(e)** PCrV-TTP; **(f)** PCrV-TT; **(g)** PCrV-T; **(h)** PCrV-BiTTP.

3.3 Electronic properties

The theoretical knowledge of the HOMO and LUMO energy levels of the components is fundamental for the study of organic solar cells. Electronic properties are of paramount importance for the study of this type of molecules. Among these properties, it is mentioned the LUMO, HOMO levels, and the energy gap (Davidson *et al.*, 1984; Jabha and Abdellah, 2018; Kato *et al.*, 2014; 2015), the latter being one of the most important factors in the control of physical and photovoltaic properties. The theoretical and experimental gap energy values of the PCrV and PCrV-T oligomers were compared, which are, respectively, 2.78 and 2.6 eV (Leclerc *et al.*, 2006) (Fig. 6).

The values plotted in the graph shown in Fig. 6 demonstrate that the energy gap decreases when the R groupings, R ≠ H, on the carbon skeleton are added. This phenomenon is apparent specifically for R = BiTTP and R = TTN.

One of the most important parameters for determining the quality of π-conjugate compounds is the value of the gap. More than the energy gap close to that of a semiconductor, the more the compose quality is candidate for use in the manufacture of electronic devices. For this reason, the most efficient strategy to have good molecules is to increase the aromaticity of these compounds by introducing R groups. All the calculations made by DTF under the functional B3LYP with the atomic base 6-31G (d,p), show a decrease of the energy gap of the oligomers, but for the oligomers PCrV and PCrV-T a band gap far from the experimental one of these molecules is obtained. On the other hand, the calculations made by the BP86 functional of the DFT method under the atomic base 6-31G (d,p) show a proximity of the calculated gap energy and the experimental band gap, as well as the decrease of the gap energy Eg of the oligomers.
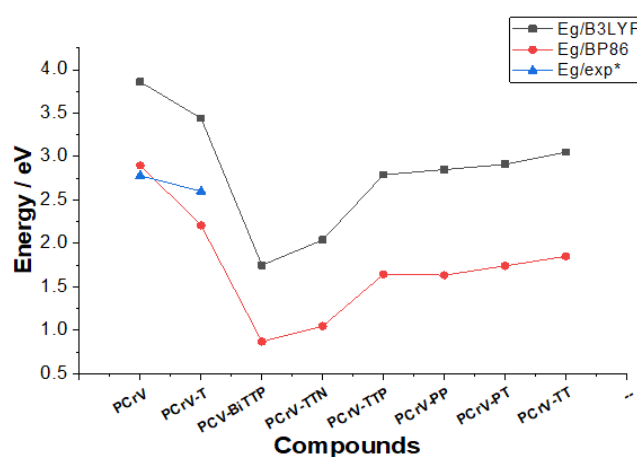
Figure 6. Data of band gap energy of all compounds obtained by B3LYP and BP86 functional.

Figure 7 shows that the band gap is generally low for all systems studied, the observed decrease in the band is due to the addition of the conjugated R group.

These results are confirmed by the propagation of the electron density. This phenomenon appears very clearly below (see Fig. 11). The electron density of LUMO is higher around the R unit for systems with smaller energy gap and precisely for the oligomers PCrV-BiTTP, PCrV-TTN, PCrV-TTP. This feature precisely allows these systems (PCrV-BiTTP, PCrV-TTN, PCrV-TTP) to be used to produce and manufacture electronic devices for photovoltaics.

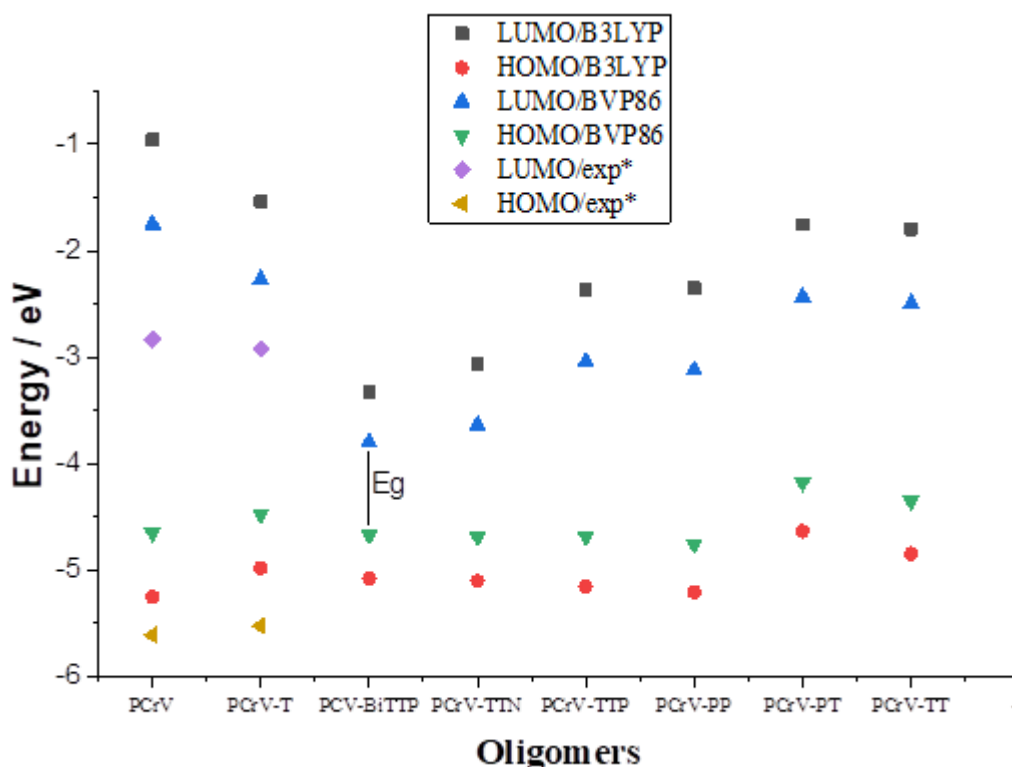**Figure 7.** Data of absolute energy of the frontier orbital HOMO and LUMO for all compounds: obtained at DFT-B3LYP and DFT-BP86 methods.

3.4 Electrochemical properties

According to the optimization of structures by the DFT method with the atomic base 6-31G (d,p) and at the functional levels B3LYP and BP86, several chemical parameters were determined, namely: the electronic chemical potential μ, the electronegativity and the global hardness (Ayers, 2007; Cherkasov *et al.*, 1998; Miranda-Quintana *et al.*, 2016; Zhou and Parr, 1989).

The electronegativity (Eq. 1) is opposite of the chemical electronic potential μ (Eq. 2), the latter and the global hardness (Eq. 3) are calculated from the energies of the molecular orbital boundaries according to the following relationships (Khalid *et al.*, 2020; Parr and Pearson, 1983; Zhou and Parr, 1989):

$$\mu = -\chi \tag{1}$$

$$\mu = \frac{E_{HOMO} + E_{LUMO}}{2} \tag{2}$$

$$\eta = \frac{E_{LUMO} - E_{HOMO}}{2} \tag{3}$$

In Tabs. 2 and 3, the electronic and chemical parameters obtained from the optimized structures are

presented, namely: HOMO and LUMO energies, chemical potential, overall hardness and electronegativity of the compounds (PCrV-R) and the Bis-PCBM acceptor. From these results (Tabs. 2 and 3), it can be seen that the Bis-PCBM compound has the lowest chemical potential value (–4.95 eV) compared to the other compounds.

Table 2. HOMO (eV) and LUMO (eV) energies, chemical potential (eV), overall hardness (eV) and electronegativity (eV) obtained by B3LYP/6-31G (d.p).

Compounds	LUMO (eV)	HOMO (eV)	μ (eV)	η (eV)	χ (eV)
PCrV	–1.38	–5.24	–3.31	1.93	3.31
PCrV-T	–1.54	–4.98	–3.26	1.72	3.26
PCV-BiTTP	–3.33	–5.08	–4.20	0.87	4.20
PCrV-TTN	–3.06	–5.10	–4.08	1.02	4.08
PCrV-TTP	–2.36	–5.15	–3.76	1.40	3.76
PCrV-PP	–2.35	–5.21	–3.78	1.43	3.78
PCrV-PT	–1.75	–4.63	–3.19	1.44	3.19
PCrV-TT	–1.79	–4.85	–3.32	1.53	3.32
Bis-PCBM	–3.80	–6.10	–4.95	3.50	4.95

Table 3. HOMO (eV) and LUMO (eV) energies, chemical potential (eV), overall hardness (eV) and electronegativity (eV) obtained by BP86/6-31G (d.p).

Compounds	LUMO (eV)	HOMO (eV)	μ (eV)	η (eV)	χ (eV)
PCrV	−1.75	−4.65	−3.20	1.45	3.20
PCrV-T	−2.27	−4.47	−3.37	1.10	3.37
PCV-BiTTP	−3.80	−4.67	−4.23	0.43	4.23
PCrV-TTN	−3.64	−4.69	−4.16	0.52	4.16
PCrV-TTP	−3.04	−4.69	−3.86	0.82	3.86
PCrV-PP	−3.12	−4.76	−3.94	0.82	3.94
PCrV-PT	−2.43	−4.17	−3.30	0.87	3.30
PCrV-TT	−2.50	−4.35	−3.42	0.93	3.42
Bis-PCBM	−3.80	−6.10	−4.95	3.50	4.95

3.5 Chemical potential

Figure 8 shows that all systems studied have a donor character with a small difference in the ability to release electrons easily. The passage of electrons will take place from the compounds with the highest chemical potential to the one with the lowest chemical potential, therefore, since the value of the chemical potential of Bis-PCBM is smaller in comparison to the other compounds, it can be deduced that Bis-PCBM will behave as an electron acceptor while the others will behave as electron donors.
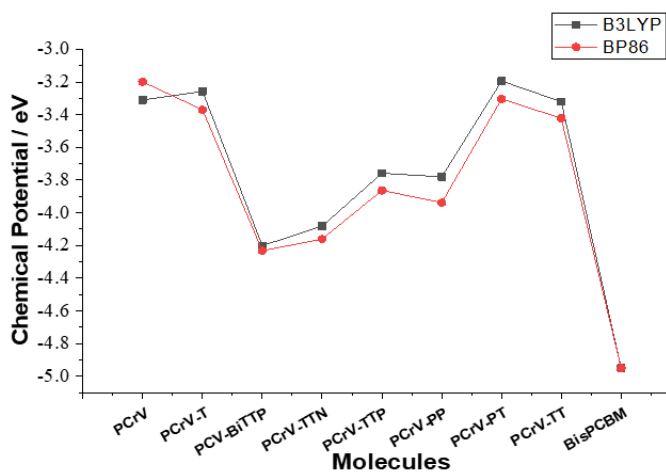

Figure 8. Chemical potential of oligomers studied by the DFT method under the base 6-31G (d,p).

3.6 Electronegativity of the different compounds

Comparing the different values of electronegativity shown in Fig. 9, it can be noticed that Bis-PCBM is the molecule with the highest value of electronegativity (Tabs. 2 and 3). Therefore, the molecule with the highest electronegativity value is likely to attract electrons strongly. Here, Bis-PCBM is the electron accepting molecule.
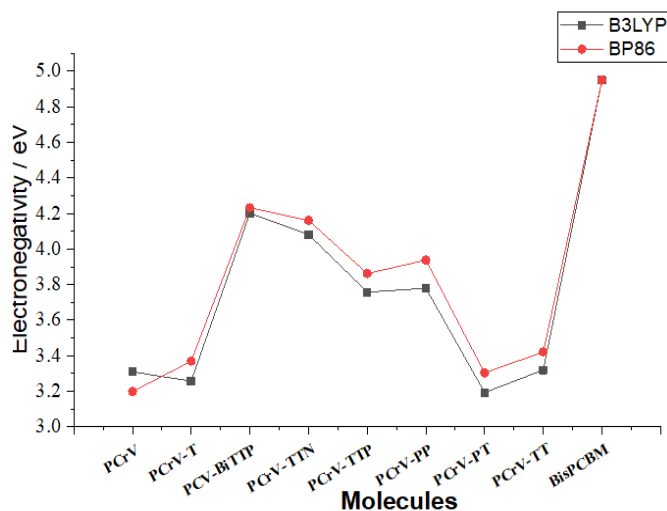

Figure 9. Electronegativities of oligomers obtained by DFT/6-31G (d,p).

3.7 Global hardness of different molecules

According to Fig. 10, the oligomer with the highest global hardness (PCrV and PCrV-T). These molecules hardly undergo any rearrangement of their electronic structure and will have the lowest reactivity.
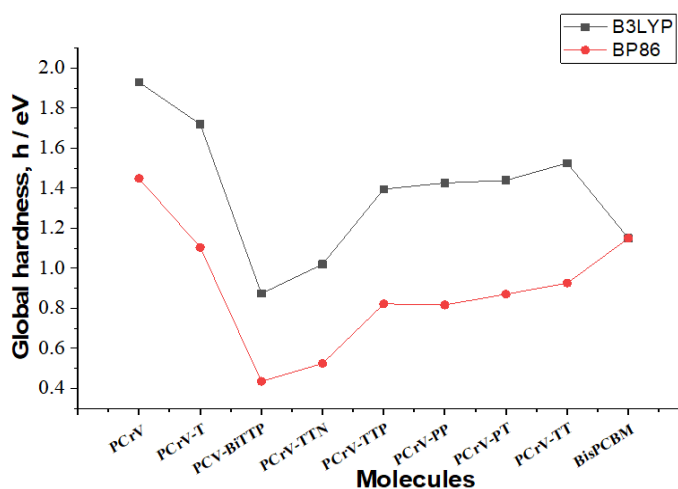
Figure 10. The global hardness obtained by DFT/6-31G (d,p).

The oligomer PCrV-BiTTP can easily undergo a change of their electronic structure by chemical reaction, probably leading to the creation of covalent bonds, so it is easier to polymerize this molecule.

3.8 The frontier orbitals

Figure 11 presents the electron density of the HOMO and LUMO orbitals of the studied oligomers. These give a qualitative and rational indication of the electronic properties of the studied oligomers.

HOMO   LUMO

a) PCrV

b)

c) PCrV-T

d)

e) PCV-BiTTP

f)

g) PCrV-TTN

h)
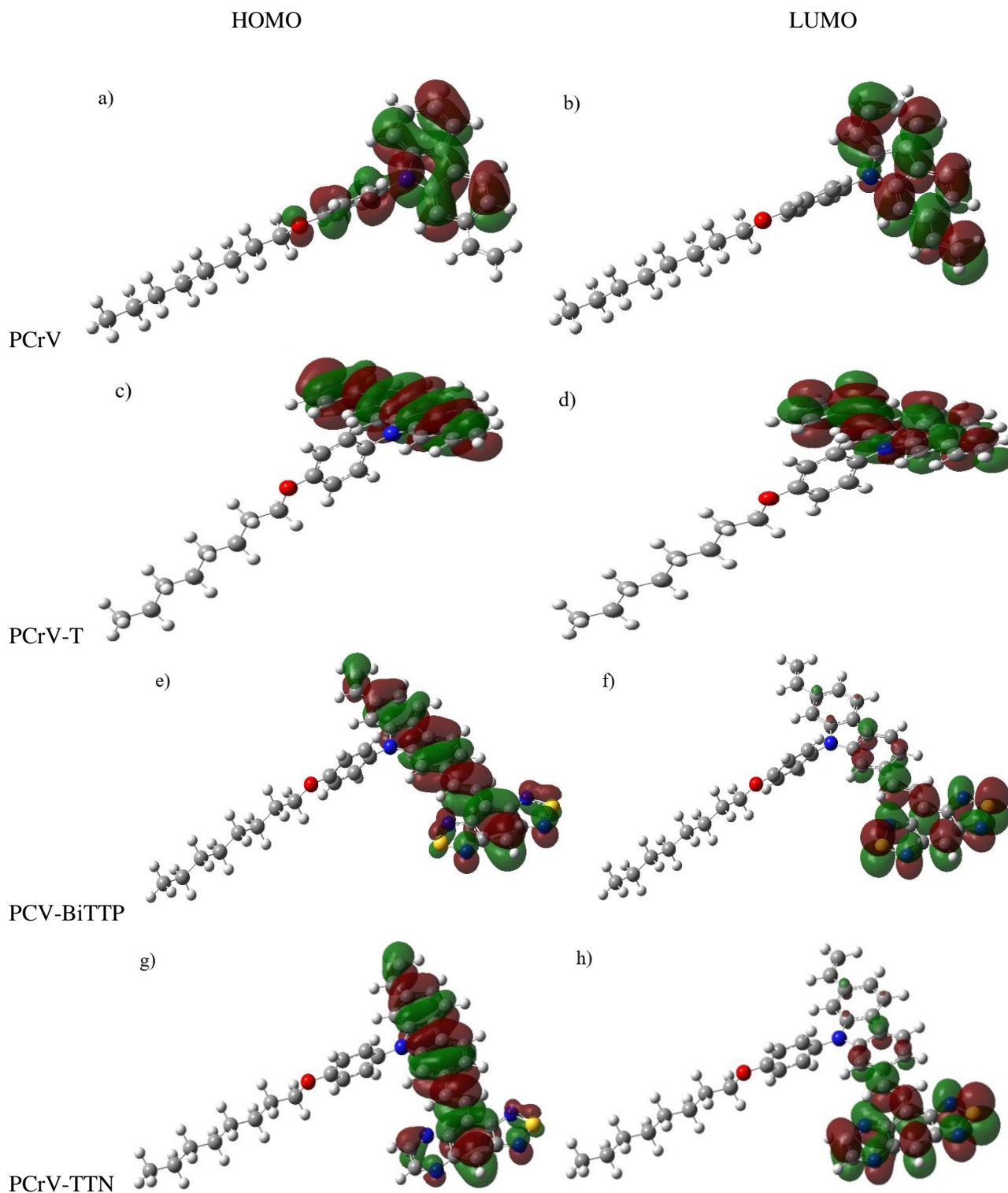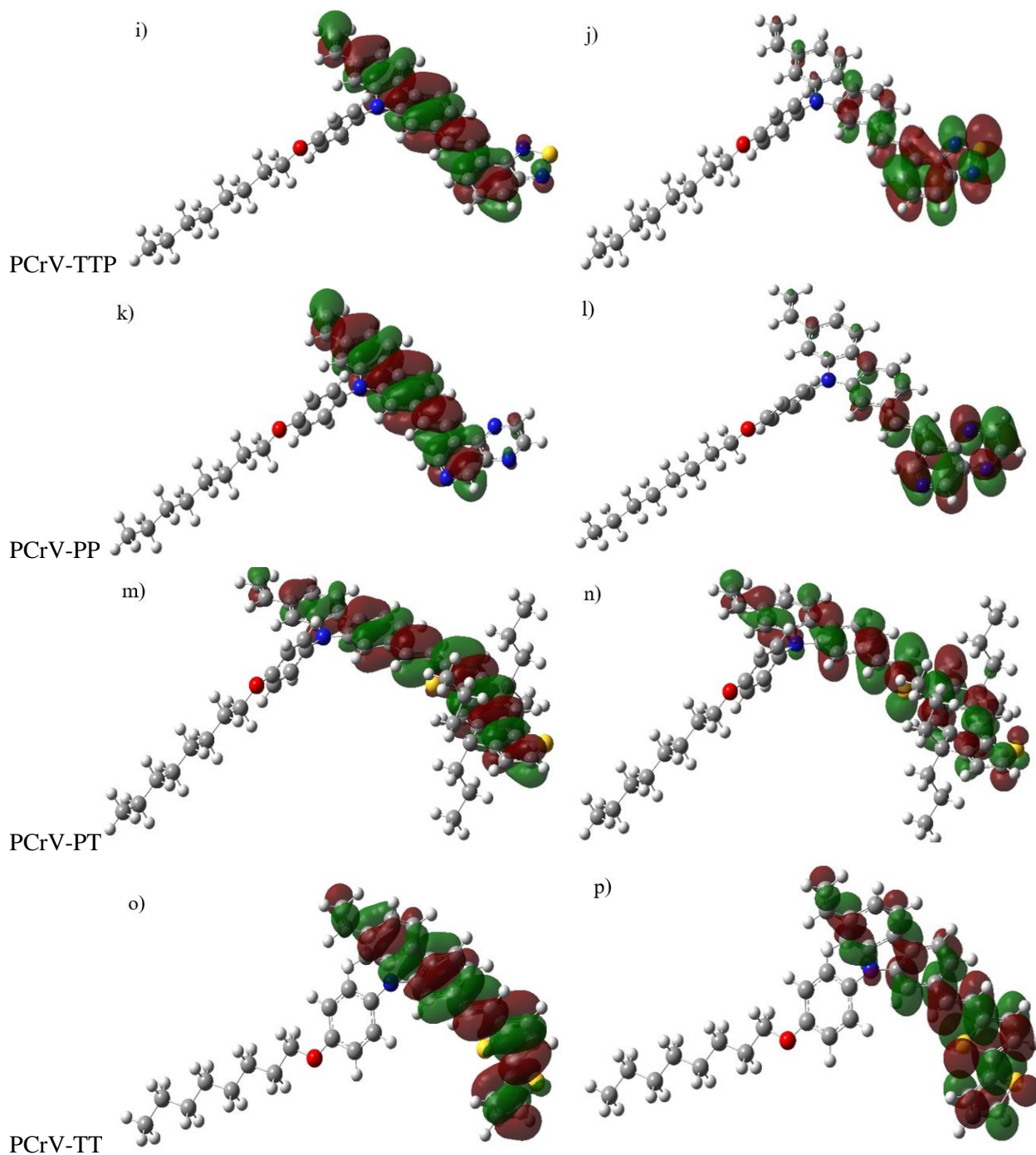
Figure 11. The contour plots of HOMO **(a, c, e, g, i, k, m, o)** and LUMO **(b, d, f, h, j, l, n, p)** orbitals of the studied compounds.

Figure 11 shows that the electron density is spread over the entire carbon skeleton at the HOMO level, and an almost complete shift towards the R group at the LUMO level. Also note the absence of electron density on the carbon chain bound to the nitrogen (N) in carbazole. Thus, this chain has no optical effect. Its main role is the solubilization and stability of the system.

3.9 Optical proprieties

Table 4 shows the values of the excitation energy E_{ex} (eV), the absorption maximum (Jabha and Abdellah, 2018; Leliège et al., 2013) λ_{max} (nm) and the oscillator strength (F_{os}) for all the molecules studied. These calculated values are obtained by the methods TD-B3LYP/6-31G(d,p) and TD-BP86/6-31G(d,p).

Table 4. Electronic transition data obtained by the TD/DFT-B3LYP/6-31G(d,p), TD-DFT/BP866-31G(d,p) calculation for all model compounds.

Compounds	DFT-B3LYP/6-31G (d.p)			DFT-BP86/6-31G (d.p)			
	E_{ex}	F_{os}	λ_{max}	E_{ex}	F_{os}	λ_{max}	λ_{max}(exp)
PCrV	3.71	0.05	334.14	3.12	0.04	397.62	
	4.14	0.44	300.00	3.52	0.02	352.49	436[9]
	4.25	0.05	291.84	3.61	0.01	343.44	
PCrV-T	3.26	1.55	380.67	2.61	0.02	474.28	
	3.31	0.04	373.97	2.82	1.22	439.74	466[9]
	3.88	0.02	319.30	3.01	0.01	411.20	
PCV-BiTTP	1.96	0.49	633.00	1.17	0.02	1062.34	
	3.32	0.03	373.75	1.35	0.37	917.77	-
	3.36	0.31	369.26	1.85	0.01	670.04	
PCrV-TTN	2.34	0.58	529.53	1.27	0.01	979.37	
	3.16	0.01	391.78	1.44	0.35	860.84	-
	3.57	0.03	347.63	2.02	0.03	613.96	
PCrV-TTP	3.21	0.99	386.55	1.82	0.01	682.07	
	3.91	0.06	317.27	1.91	0.28	649.05	-
	4.09	0.67	303.03	2.62	0.06	473.42	
PCrV-PP	3.41	1.13	364.07	1.74	0.02	712.35	
	3.63	0.01	341.23	1.83	0.22	675.59	-
	3.93	0.06	315.55	2.55	0.01	485.02	
PCrV-PT	3.19	2.21	388.36	2.21	1.91	561.02	
	3.67	0.04	337.85	2.35	0.01	526.47	-
	3.84	0.16	323.21	2.45	0.04	505.13	
PCrV-TT	3.28	1.80	378.28	2.33	0.02	531.34	
	3.97	0.06	312.48	2.41	1.44	514.55	-
	4.25	0.21	291.37	2.64	0.13	469.64	

To study the optical properties, the structures by the B3LYP/6-31G(d) method were optimized. The UV-visible spectra (Fig. 12a and b) of the studied compounds were calculated using the TD-DFT method. In Tab. 4, the calculated values of maximum absorption wavelengths (l_{max}), excitation energies (E_{ex}) and oscillator forces (F_{os}) were presented.

Molecules with an energy gap below 3.05 eV (PCrV-TT, PCrV-TP, PCrV-PP, PCrV-TTP, PCrV-TTN, PCrV-BiTTP) have absorption maxima for both computational functions (B3LP and BP86), thus reflecting the HOMO–LUMO transition. In addition, the simulated absorption spectra (Fig. 12a and b) of all compounds studied have a shoulder, which can be attributed to the intramolecular charge transfer band caused by the R group introduced into the skeleton of the structures of these molecules. This indicates that these organic materials could absorb the maximum amount of incident light radiation, in particular the molecules PCrV-BiTTP, PCrV-TTN and PCrV-TTP. This property is beneficial to increase the photoelectric conversion efficiency of the solar cell containing these types of molecules.

The excitation in the S1 state corresponds exclusively to the promotion of an electron from the HOMO to the LUMO, and to the greatest oscillation force ($F_{os} < 1$) that comes from the S0→S1 electronic transition.

The excitation in the S1 state corresponds to HOMO→LUMO + 1, and the high values of the oscillation force ($F_{os} > 1$) in these compounds comes from the S0→S2 electronic transition.
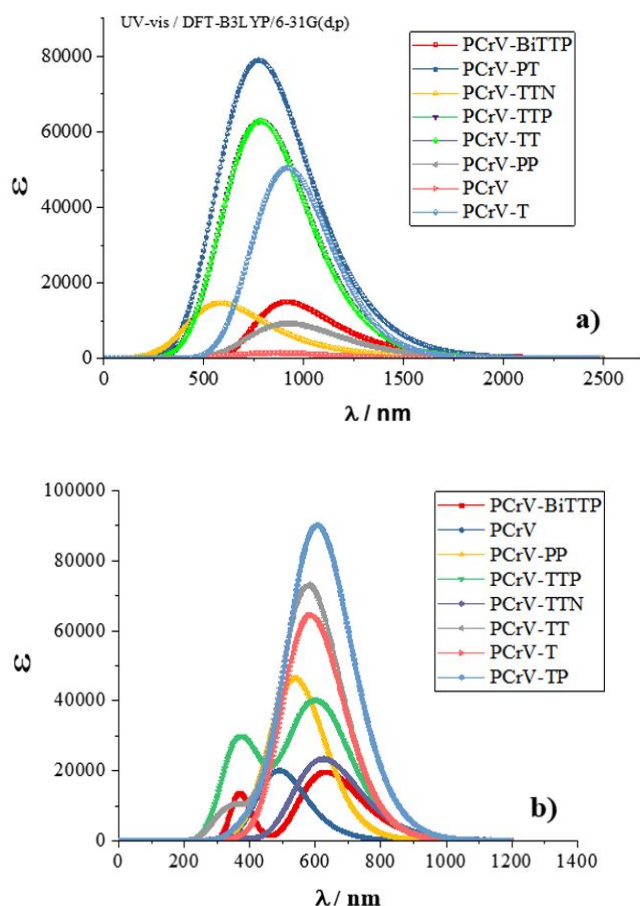
Figure 12. Data of UV-visible absorbance of all oligomers obtained at **(a)** DFT-BP86/6-31G (d,p) and **(b)** DFT-B3LYP/6-31G(d,p).

All the compounds studied show simulated wavy absorption spectra; this can be attributed to the intermolecular transfer charge in the structures of these molecules. This indicates that these organic materials could absorb the maximum of the incident light radiation. The energy range for all the structures studied is generally in the visible field.

From the absorption spectra (Fig. 12b), the electronic transitions of the double spectral band for all molecules belong to the visible field and in particular for the oligomers PCrV-BiTTP, PCrV-TTP. That is to say, the low energy radiation can excite the electrons of the system.

Concerning the energy absorption, it was found that some studied molecules absorb in the ultraviolet while others in the infrared, this factor is important for a good photovoltaic application of these molecules.

3.10 Photovoltaics proprieties

The theoretical values of the open circuit voltage, Voc, have been calculated from the following expression (Eq. 4 and Eq. 5) (Boussaidi *et al.*, 2016; Bourass *et al.*, 2017):

The energy values of LUMO (eV), HOMO (eV), E gap (eV) and the open circuit voltage Voc (eV) and α (eV) of the studied molecules are presented in Tab. 5.

$$Voc = |E\ HOMO(Donneur)| - |ELUMO\ (Accepteur)| - 0.3 \tag{4}$$

$$\alpha = |E\ LUMO\ (Accepteur)| - |ELUMO\ (Donneur) \tag{5}$$

Table 5. LUMO (eV), HOMO (eV), Voc (eV) and α (eV) obtained by B3LYP/6-31 G (d,p)

Compound	$|E_{HOMO}|$	$|E_{LUMO}|$	Voc (eV)	α
PCrV	5.25	0.95	1.15	2.84
PCrV-T	4.99	1.54	0.88	2.26
PCrV-PT	4.63	1.75	0.53	2.05
PCrV-PP	5.21	2.35	1.11	1.45
PCrV-TTN	5.10	3.06	1.01	0.74
PCrV-BiTT	5.07	3.33	0.98	0.47
Bis-PCBM	6.10	3.80	-----	------

The theoretical values of the open circuit voltage (V_{oc}) of the studied molecules range from 0.53 to 1.15 eV taking as acceptor semiconductor the Bis-PCBM within the solar cell. The molecules PCrV, PCrV-PP, PCrV-TTN and PCrV-BiTT have high V_{OC} values and low gaps, as well as small α values allowing the passage of electrons from the donor LUMO to the acceptor LUMO, especially for the PCrV-BiTT molecule (α = 0.47), with a good position of HOMO compared to that of Bis-PCBM. These arguments make these molecules good and promising candidates for photovoltaic applications.

4. Conclusions

In this paper, quantum chemical studies on the geometry and electronic properties of several compounds based on 2.7-divnyl-carbazol are carried out to show the variation effects of alkyl R groups.

The approach of increasing the conjugation length in the skeleton of these oligomers offers good optoelectronic and photovoltaic properties for the studied systems. This is clearly justified by the results obtained which show low bandgap values especially for the molecules PCrV-BiTTP, PCrV-TTP and PCrV-TTN. Add to this the high values of the absorption maxima λ_{max} as well as the good location of the HOMO and LUMO levels of these molecules. These results lead to suggest these materials as good candidates for applications in organic solar cells.

Two functionalities were used to describe the geometrical and optoelectronic properties to compare the results, and the BP86 function was found to give good results at the energy gap level, while other parameters using the B3LYP function give the best results.

Authors' contribution

Conceptualization: Jabha, M.; Elalaoui, A.
Data curation: Jabha, M.
Formal Analysis: Jabha, M.
Funding acquisition: Not applicable
Investigation: Jabha, M.; Mabrouk. E. H.
Methodology: Jabha, M.; Elalaoui, A.; Jarid, A.
Project administration: Elalaoui, A.
Resources: Not applicable
Software: Not applicable
Supervision: Elalaoui, A.; Jarid, A.
Validation: Elalaoui, A.; Mabrouk. E. H.
Visualization: Elalaoui, A.; Jarid, A.
Writing – original draft: Jabha, M.
Writing – review & editing: Jabha, M.; Mabrouk. E. H.

Data availability statement

All data sets were generated and analyzed in the current study.

Funding

Not applicable

References

Ayers, P. W. The physical basis of the hard/soft acid/base principle. *Faraday Discuss*. **2007**, *135*, 161–190. https://doi.org/10.1039/B606877D

Baek, M.-J.; Lee, S.-H.; Kim, D. H.; Lee, Y.-S. Carbazole-thieno[3,4-b]thiophene polymers: Synthesis and photovoltaic applications. *Macromol. Res.* **2012**, *20* (2), 147–154. https://doi.org/10.1007/s13233-012-0019-0

Baseden, K. A.; Tye, J. W. Introduction to Density Functional Theory: Calculations by Hand on the Helium Atom. *J. Chem. Educ.* **2014**, *91* (12), 2116–2123. https://doi.org/10.1021/ed5004788

Becke, A. D. Density-functional exchange-energy approximation with correct asymptotic behavior. *Phys. Rev. A.* **1988**, *38* (6), 3098–3100. https://doi.org/10.1103/PhysRevA.38.3098

Blouin, N.; Michaud, A.; Gendron, D.; Wakim, S.; Blair, E.; Neagu-Plesu, R.; Belletête, M.; Durocher, G.; Tao, Y.; Leclerc, M. Toward a Rational Design of Poly(2,7-Carbazole) Derivatives for Solar Cells. *J. Am. Chem. Soc.* **2008**, *130* (2), 732–742. https://doi.org/10.1021/ja0771989

Bourass M.; Benjelloun, A. T.; Benzakour, M.; Mcharfi, M.; Jhilal, F.; Serein-Spirau, F.; Sotiropoulos, J. M.; Bouachrine, M. DFT/TD-DFT characterization of conjugational electronic structures and spectral properties of materials based on thieno[3,2-b][1]benzothiophene for organic photovoltaic and solar cell applications. *J. Saudi Chem. Soc.* **2017**, *21* (5), 563–574. https://doi.org/10.1016/j.jscs.2017.01.001

Boussaidi, S., Alaoui, Y., Abderrahim, E., Fitri, A., Benjelloun, A. T., Hsaine, Z., Chaib, H., Bouachrine, M., Hamidi, M., Hadda, T. B., Theoretical study of the effect of substitution with alternating donor and acceptor groups on the optoelectronic and photovoltaic properties of some oligomers containing thiophene and phenylene. *Arab. J. Chem. Environ. Res.* **2016**, *3* (1), 51–63.

Cai, Z.-L.; Sendt, K.; Reimers, J. R. Failure of density-functional theory and time-dependent density-functional theory for large extended π systems. *J. Chem. Phys.* **2002**, *117* (12), 5543–5549. https://doi.org/10.1063/1.1501131

Chen, Q.; Zhou, H.; Hong, Z.; Luo, S.; Duan, H.-S.; Wang, H.-H.; Liu, Y.; Li, G.; Yang, Y. Planar Heterojunction Perovskite Solar Cells via Vapor-Assisted Solution Process.

J. Am. Chem. Soc. **2014**, *136* (2), 622−625. https://doi.org/10.1021/ja411509g

Cherkasov, A. R.; Galkin, V. I.; Zueva, E. M.; Cherkasov, R. A. The concept of electronegativity. The current state of the problem. *Russ. Chem. Rev*. **1998**, *67* (5), 375–392. https://doi.org/10.1070/RC1998v067n05ABEH000383

Cramer, C. J.; Truhlar, D. G. Density functional theory for transition metals and transition metal chemistry. *Phys. Chem. Chem. Phys*. **2009**, *11* (46), 10757–10816. https://doi.org/10.1039/B907148B

Davidson, C. L.; De Gee, A. J.; Feilzer, A. The Competition between the Composite-Dentin Bond Strength and the Polymerization Contraction Stress. *J. Dent. Res*. **1984**, *63* (12), 1396–1399. https://doi.org/10.1177/00220345840630121101

Francl, M. M.; Pietro, W. J.; Hehrea, W. J.; Binkley, J. S.; Gordon, M. S.; DeFrees, D. J.; Pople, J. A. Self-consistent molecular orbital methods. XXIII. A polarization-type basis set for second-row elements. *J. Chem. Phys*. **1982**, *77* (7), 3654-3665. https://doi.org/10.1063/1.444267

Fukuta, S.; Wang, Z.; Miyane, S.; Koganezawa, T.; Sano, T.; Kido, J.; Mori, H.; Ueda, M.; Higashihara, T. Synthesis of 1,3,4-thiadiazole-based donor–acceptor alternating copolymers for polymer solar cells with high open-circuit voltage. *Polym. J*. **2015**, *47* (7), 513–521. https://doi.org/10.1038/pj.2015.19

Ganji, M. D.; Tajbakhsh, M.; Kariminasab, M.; Alinezhad, H. Tuning the LUMO level of organic photovoltaic solar cells by conjugately fusing graphene flake: A DFT-B3LYP study. *Phys. E: Low-Dimens. Syst. Nanostructures*. **2016**, *81*, 108–115. https://doi.org/10.1016/j.physe.2016.03.008

Garrity, K. F.; Bennett, J. W.; Rabe, K. M.; Vanderbilt, D. Pseudopotentials for high-throughput DFT calculations. *Comput. Mater. Sci*. **2014**, *81*, 446–452. https://doi.org/10.1016/j.commatsci.2013.08.053

Gaussian 09; Gaussian, Inc.: Wallingford, 2009. https://gaussian.com/glossary/g09/ (accessed 2017-12-16).

Gill, P. M. W.; Johnson, B. G.; Pople, J. A.; Frisch, M. J. The performance of the Becke—Lee—Yang—Parr (B—LYP) density functional theory with various basis sets. *Chem. Phys. Lett*. **1992**, *197* (4–5), 499–505. https://doi.org/10.1016/0009-2614(92)85807-M

Huang, F. High-performance polymer solar cells with >10% efficiency. *Sci. China Chem*. **2015**, *58* (2), 190. https://doi.org/10.1007/s11426-014-5314-5

Jabha, M.; Abdellah, A. Study Optoelectronic and Geometric Properties of New compounds Based on Carbazole-thiophene Bridged for Solar Cells. *Orbital: Electron. J. Chem*. **2018**, *10* (7), 552-560. https://doi.org/10.17807/orbital.v10i7.1322

Jacquemin, D.; Wathelet, V.; Perpète, E. A.; Adamo, C. Extensive TD-DFT Benchmark: Singlet-Excited States of Organic Molecules. *J. Chem. Theory Comput*. **2009**, *5* (9), 2420–2435. https://doi.org/10.1021/ct900298e

Kato, S.-I.; Shimizu, S.; Kobayashi, A.; Yoshihara, T.; Tobita, S.; Nakamura, Y. Systematic Structure–Property Investigations on a Series of Alternating Carbazole–Thiophene Oligomers. *J. Org. Chem*. **2014**, *79* (2), 618–629. https://doi.org/10.1021/jo402416f

Kato, S.-I.; Yamada, Y.; Hiyoshi, H.; Umezu, K.; Nakamura, Y. Series of Carbazole–Pyrimidine Conjugates: Syntheses and Electronic, Photophysical, and Electrochemical Properties. *J. Org. Chem*. **2015**, *80* (18), 9076–9090. https://doi.org/10.1021/acs.joc.5b01409

Khalid, M.; Ali, A.; Rehman, M. F. U.; Mustaqeem, M.; Ali, S.; Khan, M. U.; Asim, S.; Ahmad, N.; Saleem, M. Exploration of Noncovalent Interactions, Chemical Reactivity, and Nonlinear Optical Properties of Piperidone Derivatives: A Concise Theoretical Approach. *ACS Omega*, **2020**, *5* (22), 13236–13249. https://doi.org/10.1021/acsomega.0c01273

Kim, Y.; Cho, H.-H.; Kim, T.; Liao, K.; Kim, B. J. Terpolymer approach for controlling the crystalline behavior of naphthalene diimide-based polymer acceptors and enhancing the performance of all-polymer solar cells. *Polym. J*. **2016**, *48* (4), 517–524. https://doi.org/10.1038/pj.2016.22

Koh, S. E.; Risko, C.; Silva Filho, D. A. da; Kwon, O.; Facchetti, A.; Brédas, J.-L.; Marks, T. J.; Ratner, M. A. Modeling Electron and Hole Transport in Fluoroarene-Oligothiopene Semiconductors: Investigation of Geometric and Electronic Structure Properties. *Adv. Funct. Mater*. **2008**, *18* (2), 332–340. https://doi.org/10.1002/adfm.200700713

Laurent, A. D.; Jacquemin, D. TD-DFT benchmarks: A review. *Int. J. Quantum Chem*. **2013**, *113* (17), 2019–2039. https://doi.org/10.1002/qua.24438

Leclerc, N.; Michaud, A.; Sirois, K.; Morin, J.-F.; Leclerc, M. Synthesis of 2,7-Carbazolenevinylene-Based Copolymers and Characterization of Their Photovoltaic Properties. *Adv. Funct. Mater*. **2006**, *16* (13), 1694–1704. https://doi.org/10.1002/adfm.200600171

Leliège, A; Grolleau, J.; Allain, M.; Blanchard, P.; Demeter, D; Rousseau, T.; Roncali, J. Small D–π–A Systems with o-Phenylene-Bridged Accepting Units as Active Materials for Organic Photovoltaics. *Chem. Eur. J*. **2013**, *19* (30), 9948–9960. https://doi.org/10.1002/chem.201301054

Miranda-Quintana, R. A.; González, M. M.; Ayers, P. W. Electronegativity and Redox Reactions. *Phys. Chem. Chem. Phys*. **2016**, *18* (32), 22235–22243. https://doi.org/10.1039/C6CP03213C

Mitin, A. V.; Baker, J.; Pulay, P. An improved 6-31G* basis set for first-row transition metals. *J. Chem. Phys*. **2003**, *118* (17), 7775–7783. https://doi.org/10.1063/1.1563619

Nazim, M.; Ameen, S.; Seo, H.-K.; Shin, H. S. Effective D-A-D type chromophore of fumaronitrile-core and terminal alkylated bithiophene for solution-processed small molecule organic solar cells. *Sci. Rep*. **2015**, *5* (1), 1–10. https://doi.org/10.1038/srep11143

Nishiyama, J.; Ellison, E. C.; Mizuno, G. R.; Chipault, J. R. Micro-determinations of α-tocopherol in tissue lipids. *J. Nutr. Sci. Vitaminol*. **1975**, *21* (5), 355–361. https://doi.org/10.3177/jnsv.21.355

Parr, R. G.; Pearson, R. G. Absolute hardness: companion parameter to absolute electronegativity. *J. Am. Chem. Soc*. **1983**, *105* (26), 7512–7516. https://doi.org/10.1021/ja00364a005

Scharber, M. C.; Sariciftci, N. S. Efficiency of bulk-heterojunction organic solar cells. *Prog. Polym. Sci*. **2013**, *38* (12), 1929–1940. https://doi.org/10.1016/j.progpolymsci.2013.05.001

Tarascon, J.-M. Le photovoltaïque: principes et filières inorganiques, organiques, hybrids. Chaire Développement durable, 2011, p. 56.

Toub, D. A Review of Photovoltaic Cells, Department of electrical and Computer engineering, University of Rochester, Rochester, New York, (2007) 1-3. http://www2.ece.rochester.edu/courses/ECE423/ECE223_423_MSC426%20Workshop06/term%20papers%2006/Toub_06.pdf (accessed 2019-11-26).

Xu, X.; Goddard, W. A. The X3LYP extended density functional for accurate descriptions of nonbond interactions, spin states, and thermochemical properties. *Proc. Natl. Acad. Sci. U.S.A*. **2004**, *101* (9), 2673–2677. https://doi.org/10.1073/pnas.0308730100

Zeyada, H. M.; EL-Nahass, M. M.; El-Shabaan, M. M. Photovoltaic properties of the 4H-pyrano[3,2-c]quinoline derivatives and their applications in organic–inorganic photodiode fabrication. *Synth. Met*. **2016**, *220*, 102–113. https://doi.org/10.1016/j.synthmet.2016.05.028

Zhao, W.; Cai, W.; Xu, R.; Yang, W.; Gong, X.; Wu, H.; Cao, Y. Novel conjugated alternating copolymer based on 2,7-carbazole and 2,1,3-benzoselenadiazole. *Polymer*. **2010**, *51* (14), 3196–3202. https://doi.org/10.1016/j.polymer.2010.04.057

Zhou, Z.; Parr, R. G. New measures of aromaticity: absolute hardness and relative hardness. *J. Am. Chem. Soc*. **1989**, *111* (19), 7371–7379. https://doi.org/10.1021/ja00201a014

Photoperoxidation of ciprofloxacin antibiotic in aqueous medium using Fe$_{3-x}$O$_{4-Y}$-TiO$_2$ particles as catalyst

Ismael Laurindo Costa Junior[1+], Kevin Augusto Ferreira[1], Cesar Augusto Kappes[1], Renata Mello Giona[1]

1. Federal Technological University of Paraná, Chemistry Department, Medianeira, Brazil.

+Corresponding author: Ismael Laurindo Costa Junior, **Phone:** +55 45999355163, **Email address:** isma_jr@hotmail.com

ABSTRACT: Conventional treatment processes are not effective in removing micropollutants such as antibiotics and other drugs present in wastewater, and degradation methods based on advanced oxidative processes become attractive. Herein, it was synthesized Fe$_{3-x}$O$_{4-y}$-TiO$_2$ particles by coprecipitation method and they were heat-treated at 100, 400, and 800 °C. The obtained solids were characterized by X-ray diffraction and thermogravimetric analysis and analytical determinations were performed using ultraviolet-visible (UV-Vis) spectrophotometry. The particles were evaluated in photoperoxidation processes on the degradation of the ciprofloxacin antimicrobial in an aqueous solution. The studies took place at pH 9; with an H$_2$O$_2$ concentration of 31 mg L^{-1} and particle mass 0.22 g L^{-1} previously defined and, in these conditions, degradation percentages between 40 and 85% were observed, with the removal in the Photo/H$_2$O$_2$/Fe$_{3-x}$O$_{4-y}$-TiO$_2$ 800 °C. The kinetic study performed for this process revealed the process adjusts to the first-order kinetics during the 120 min of reaction. The use of the catalyst can be attractive with the potential for degradation of the studied antimicrobial.
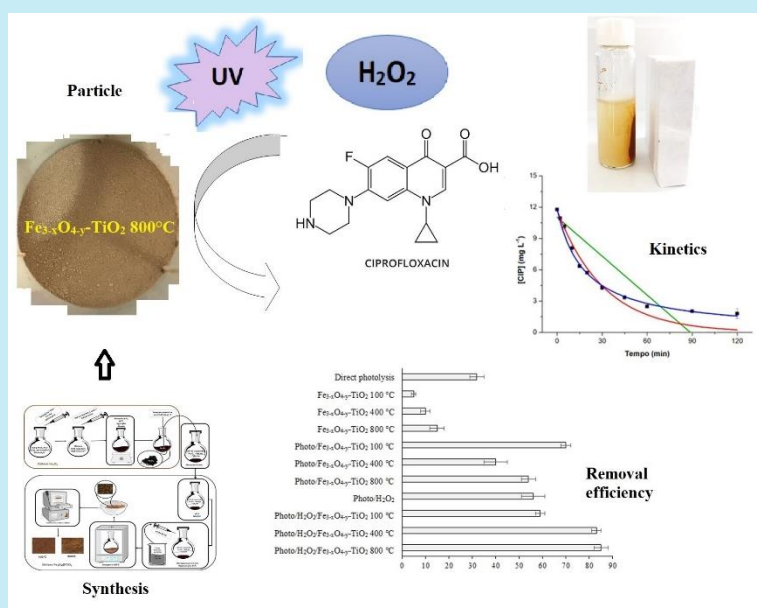
1. Introduction

Studies on residual drugs in the environment are topics of great relevance today (Costa Junior *et al.*, 2014). With the growth of the world population, the consumption of medicines has increased significantly in the last decades; as a result, these compounds are found in sewage treatment plant effluents, in water supplies, and various environmental compartments (Bound *et al.*, 2006; Luo *et al.*, 2014; Rogowska *et al.*, 2020).

One of the groups of residual drugs that attracts attention is antibiotics due to their potential effect on the development of resistant bacteria in the environment (Barancheshme and Munir, 2019; Karkman *et al.*, 2018). An example of an antimicrobial is ciprofloxacin (CIP), which belongs to the fluoroquinolone class and is widely used in human and veterinary medicine. Its excretion rate can reach 65% in urine and 25% in feces (Frade *et al.*, 2014; Halling-Sørensen *et al.*, 2000).

The discharge of domestic and industrial sewage in surface waters is one of the main routes of dispersion of emerging contaminants, especially drugs. Thus, the effective concentration of emerging pollutants, such as antibiotics, in the various environmental matrices directly depends on the efficiency of the treatment processes applied to wastewater in treatment plants (Leung *et al.*, 2012; Wu *et al.*, 2016).

The treatment methods used in sewage treatment plants are based mainly on conventional processes (physical and biochemical operations), aimed at stabilizing organic matter, removing nutrients, and disinfecting. Thus, effective degradation of these new contaminants is practically nonexistent (Oliveira *et al.*, 2020; Rajasulochana and Preethy, 2016). Some studies have suggested the removal of residual drugs in the treated sewage through the evaluation of input and output parameters in biological treatment systems (Sim *et al.*, 2010; Verlicchi *et al.*, 2012). However, other studies resulted only in the transfer of pollutants to sludge and sediments by sorption mechanisms, with no degradation or effective treatment (Barret *et al.*, 2010; Liu *et al.*, 2019; Piai *et al.*, 2020).

Considering the bioactive and persistent nature of organic micropollutants, the need for advanced treatments for their removal in wastewater is urgent. Some advanced oxidative processes (AOPs), such as ozonation, homogeneous and heterogeneous photocatalysis, are promising for pollutants degradation (Ciccotti *et al.*, 2015; Hörsing *et al.*, 2012; Hyland *et al.*, 2012; Souza *et al.*, 2018).

In heterogeneous photocatalysis, titanium dioxide (TiO_2) based catalysts have great viability and applicability to degrade a wide variety of pollutants. Its main advantages are its electronic properties, chemical stability, nontoxicity, and low cost (Rasalingam *et al.*, 2014; Yang *et al.*, 2005). Catalysts can be applied immobilized on supports or in suspension. When suspended, the separation step is a limitation of the process that involves time and costs. Magnetic particles have been extensively studied as a support for many hybrid materials, like TiO_2 (Borges *et al.*, 2015; Fabbri *et al.*, 2019; Pang *et al.*, 2012).

The association of TiO_2 photocatalytic and Fe_3O_4 magnetic properties has been explored in the proposition of core@shell particles (Ciccotti *et al.*, 2015; Noval *et al.*, 2019; Wei *et al.*, 2009). One of the advantages of using a magnetic material is that the catalyst could be easily removed from the reaction system through the application of an external magnetic field, also facilitating its recovery during the process steps (Dorigon *et al.*, 2017; Wu *et al.*, 2008).

In this work, heat-treated $Fe_{3-x}O_{4-y}$-TiO_2 magnetic particles were prepared and applied as catalysts in the degradation of the CIP antibiotic by heterogeneous photoperoxidation processes.

2. Materials and Methods

2.1 Reagents: standards and solutions

Ciprofloxacin (CIP) was purchased as an analytical standard for chromatography ($C_{17}H_{19}ClFN_3O_3$, Sigma-Aldrich) with 99.98% purity. Stock solutions of this drug were prepared at 1000 mg L^{-1}, swollen in ultrapure water and kept at 4 °C under refrigeration, protected from light. In the photocatalysis reactions, hydrogen peroxide (H_2O_2, Alphatec) was used.

Buffer solutions based on potassium phosphate (K_3PO_4, Exodus), anhydrous monobasic potassium phosphate (KH_2PO_4, Exodus), dibasic potassium phosphate (K_2HPO_4, Alphatec) and phosphoric acid were used for the reaction media 85% (H_3PO_4, Moderna). According to the pH ranges of the expeiments, adjustments were done using hydrochloric acid (HCl, Dinâmica) and sodium hydroxide (NaOH, Moderna) 0.01 mol L^{-1}. In the synthesis of particles, iron chloride III hexahydrate ($FeCl_3.6H_2O$, Dinâmica); iron chloride II ($FeCl_2$, Exodus), ammonium hydroxide (NH_4OH, Anhydrol); absolute ethyl alcohol (C_2H_6O, Dinâmica) and 97% IV titanium isopropoxide ($Ti[OCH(CH_3)_2]_4$, Sigma-Aldrich) were used.

2.2 Synthesis and characterization of $Fe_{3-x}O_{4-y}$-TiO_2 particles

The synthesis of Fe_3O_4 particles was performed using the modified coprecipitation method (Dorigon *et al.*, 2017; Wu *et al.*, 2008). Briefly, 10.8 g of $FeCl_3.6H_2O$ were added to a reaction flask containing 25 mL of 1.0 mol L^{-1} HCl aqueous solution and 50 mL of ultrapure water. In another flask, a solution of $FeCl_2$ was prepared to maintain the proportion of 2:1 in mol (Fe^{3+}/Fe^{2+}). This solution was transferred drop by drop, with the aid of a syringe, to the reaction flask containing the $FeCl_3.6H_2O$ in acidic solution, resulting in a ratio of 0.04 mol of Fe^{3+} to 0.02 mol of Fe^{2+}. Then, 250 mL of a 1.5 mol L^{-1} NaOH solution was added to the Fe^{3+}/Fe^{2+} mixture, followed by constant heating at 60 °C and stirring for 40 min under N_2 atmosphere. The black and magnetic solid obtained composed of Fe_3O_4 was thoroughly washed with ultrapure water until neutral pH, and then it was kept in suspension.

For the TiO_2 coating step, in a round-bottom flask with 250 mL capacity, 20 mL of the Fe_3O_4 suspension obtained in the previous step and 80 mL of absolute ethyl alcohol were added, followed by homogenization in an ultrasonic bath for 5 min. The pH suspension was adjusted to 9 by the addition of concentrated NH_4OH. In another flask, 24 mL of titanium isopropoxide IV 97% were added and diluted in 136 mL of ethyl alcohol, and 20 mL aliquots were added to the Fe_3O_4 suspension under homogenization for 15 min in an ultrasonic bath after each insertion.

The system remained at rest for 24 h and then it was dried in an oven at 100 °C. The solid was broken up into a mortar and divided into three parts, one set aside and the other two portions subjected to heat treatment at 400 and 800 °C, respectively, in a muffle furnace. After cooling, 1 mL of each solid was measured in a 5 mL beaker previously weighted on an analytical balance and the corresponding mass was obtained. Density was calculated by the ratio between mass and volume.

X-ray diffraction (XRD) patterns were measured using an empyrean diffractometer operating from 2 to 50° with a residence time of 2° min^{-1}.

Thermogravimetric analyzes (TGA) were performed on a Perkin Elmer STA 6000 TGA analyzer, with approximately 8 mg of the sample, which was placed on open platinum and preheated to 100 °C for 5 min. The measurements were carried out in a nitrogen atmosphere at a flow rate of 20 mL min^{-1} and a heating rate of 10 °C min^{-1}, using a heating range of up to 600 °C.

2.3 Analytical measures and photoperoxidation tests

For quantification of CIP, solutions with concentrations ranging from 1 to 25 mg L^{-1} at pH 9 were prepared for the calibration curve and were used to identify the maximum absorption band of CIP. The measurements were made by using a single beam scanning ultraviolet-visible (UV/VIS) molecular absorption spectrophotometer (PerkinElmer ™ LAMBDA XLS), in the range of 200 to 400 nm with a resolution of 2 nm. Quartz cuvettes with an optical path of 1 cm were used.

In the photoperoxidation tests, a reactor was used, consisting of a $57 \times 47 \times 47$ cm^3 metal box equipped with four low-pressure mercury lamps (15 W) (OSRAM ™ Germicidal), used as a source of UV radiation and fixed at the top about 20 cm away from the solutions. The internal temperature remained around 45 °C after 20 min of stabilization. Inside, four 250 mL glass containers were placed on four magnetic stirrers (Fisatom). The initial CIP concentration was 10 mg L^{-1}, and aliquots of the solution were taken at regular intervals over the 120 min time.

A kinetic study was performed for the best treatment observed. The determination of the rate of degradation of target molecules and their respective concentrations (order of reaction) is an important step in the study of the kinetics of chemical reactions. The order of the reaction is understood as the dependence of the speed of the reaction with the concentration, where C_0 is the initial reagent concentration, and C is the reagent concentration after a reaction time (t) (Sarkar *et al.*, 2015).

If dC/dT satisfies Eq. 1, n is the order of the reaction.

$$\frac{dC}{dt} = -k \cdot C^n \tag{1}$$

When $n = 0$ (zero order reaction), $n = 1$ (first order reaction) and $n = 2$ (second order reaction), Eq. 1 will lead to Eqs. 2–4, respectively.

$$C = C_0 - k_0 \cdot t \tag{2}$$

$$C = C_0 \cdot e^{-k1 \cdot t} \tag{3}$$

$$C = \frac{C_0}{1 + C_0 \cdot k_2 \cdot t} \tag{4}$$

In the photodegradation studies involving organic micropollutants, employed to assess persistence and susceptibility to ultraviolet radiation, the models

represented in Eqs. 2–4 are commonly applied for kinetic evaluation (Carlson *et al.*, 2015).

The experimental data obtained in the photoperoxidation tests catalyzed by the synthesized particles were evaluated in terms of the adjustments of the kinetic models (Eqs. 2–4) using the originPro 8.0 software. The decay of the CIP concentration was verified during the test and the half-life times were determined.

3. Results and discussion

3.1 Catalyst characterization

From the synthesis, it was obtained 7.9 g of $Fe_{3-x}O_{4-y}$-TiO_2 particles and they presented densities of 0.35 g mL^{-1} for the particles treated at 100 °C, 0.5 g mL^{-1} for 400 °C, and 0.6 g mL^{-1} for 800 °C (Fig. 1). This increase in density possibly resulted from the modification of the particle structure and the elimination of residual inputs from the synthesis. The magnetism of the particles was qualitatively evaluated in the presence of a neodymium magnet and, as shown in Fig. 1, $Fe_{3-x}O_{4-y}$-TiO_2 with heat treatments of 100 and 400 °C is magnetic, while the solid treated at 800 °C has lost its magnetic property upon heat treatment.
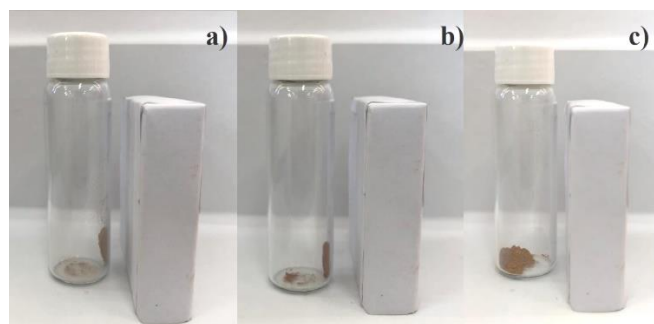
Figure 1. $Fe_{3-x}O_{4-y}$-TiO_2 being attract by a neodymium magnet. Treatments at **(a)** 100 °C **(b)** 400 °C and **(c)** 800 °C.

The crystallographic structures of the products were analyzed by powder XRD. The particles treated at 100 °C do not show peaks of a crystalline structure, suggesting an amorphous structure (Fig. 2a). Interestingly, the increase in temperature directly influenced the crystallinity of the system, with a predominance of α-Fe_2O_3 particles derived from the amorphous magnetite of the system, which is also reflected in the reduction of magnetism when heated to 800 °C (Fig. 1c).
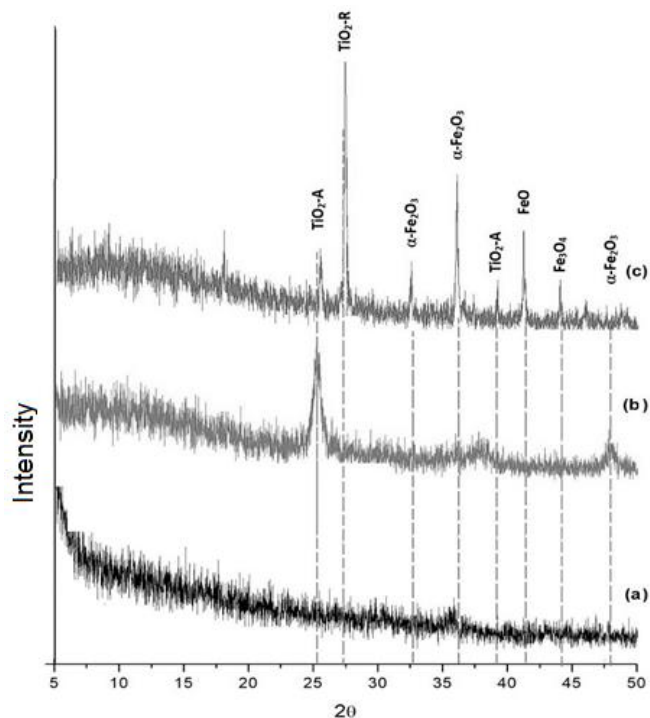

Figure 2. $Fe_{3-x}O_{4-y}$-TiO_2 XRD patterns in treatments at **(a)** 100 °C **(b)** 400 °C and **(c)** 800 °C.

In the particles treated at 400 °C (Fig. 2b), two main peaks were identified, the first referring to the TiO_2 anatase phase (25°) and the second to α-Fe_2O_3 phase (48°) (Khashan *et al.*, 2017). For the treatment at 800 °C, several peaks were observed, with the occurrence of TiO_2 anatase (25 and 39°), and rutile TiO_2 (27°), α-Fe_2O_3 (33 and 35°), FeO (42°) and Fe_3O_4 (44°) (Noval *et al.*, 2019).

The results of XRD indicate that the thermal treatments performed caused a structural modification in the synthesized particle, and the decrease in the magnetic property is due to the conversion of magnetite (Fe_3O_4) in oxides, such as α-Fe_2O_3 and FeO. Thus, it was assumed that the particles have a complex mixed composition of these compounds and, therefore, were denoted as $Fe_{3-x}O_{4-y}/TiO_2$. These hypotheses are reinforced by the TGA curves (Fig. 3).

From the TGA curves, it was determined a mass loss of approximately 25% of $Fe_{3-x}O_{4-y}$-TiO_2 particles synthesized at 100 °C. The first loss occurred between 50–150 °C and is related to the evaporation of alcohol and water residues adsorbed in the system. In the range of 150 to 350 °C, there is a loss that resulted from the decomposition of organic substances, and from 350 °C, total decomposition occurred, with crystallization beginning at high temperatures, generating a stable coating for the particles (Khashan *et al.*, 2017).

The particles treated at 400 and 800 °C did not show significant mass loss since they were previously subjected to a higher temperature. From TGA curves and XRD, it is possible to infer that the mass losses in the particles treated at 400 and 800 °C are lower than particles treated at 100 °C because the heating in the thermal treatment promoted structural changes. In addition, the TGA curves corroborate the predominance of the stable iron oxides identified in the XRD for the treatment of 800 °C.
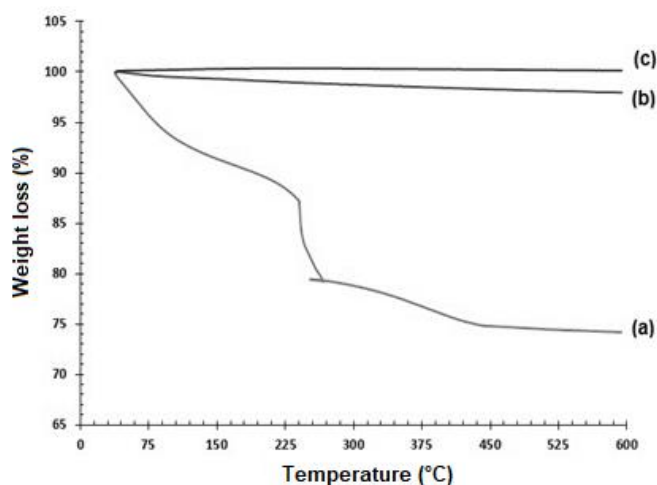

Figure 3. Thermogravimetric analyzes curves obtained for $Fe_{3-x}O_{4-y}$-TiO_2 synthesized in treatments **(a)** 100 °C **(b)** 400 °C and **(c)** 800 °C.

3.2 Application of synthesized particles in the photoperoxidation of ciprofloxacin

The absorption spectrum of the CIP drug with a concentration of 5 mg L^{-1} and pH 9 has a maximum absorption band at 278 nm, which is covered in the medium ultraviolet (Fig. 4).
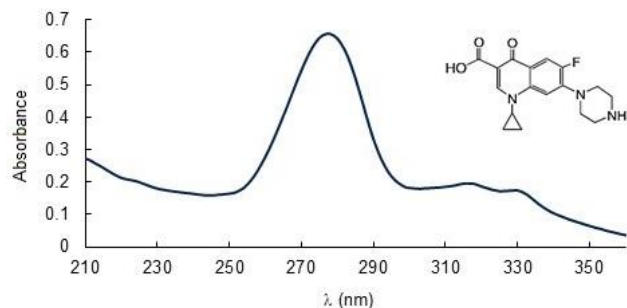

Figure 4. Ultraviolet-visible absorption spectrum in aqueous solution with a concentration of 5 mg L^{-1} of CIP and pH = 9.

Because of the molecular structure of CIP, its ionic forms depend on the pH. A cationic form is predominant in solution pH below 5.9 (up to pKa = 5.9), zwitterionic form is present in a neutral medium (5.9 < pKa < 8.9), and the anionic form is dominant at alkaline pH (pKa > 8.9) (Carabineiro *et al.*, 2012). Given that the photoperoxidation experiment was conducted at pH 9, the predominance of the anionic form of CIP is expected.

As for the surface of the photocatalyst, the pH_{PCZ} of the TiO_2 was 7.5 (Borges *et al.*, 2016). Under the conditions studied, the surface charge will also be negative, indicating that the possible removal of CIP by adsorption is unlikely, thus possibly not contributing to the results obtained through the photoperoxidation catalyzed by $Fe_{3-x}O_{4-y}$-TiO_2 particles. It is possible that, if adsorption phenomena still occur, the CIP molecules might be oxidized by reacting directly with the positive gap of the semiconductor valence layer, although this reaction is less likely (Mourão *et al.*, 2009; Nogueira and Jardim, 1998).

To evaluation the particles, the processes of direct photolysis, homogeneous photocatalysis (Photo/H_2O_2), and heterogeneous photocatalysis (Photo/$Fe_{3-x}O_{4-y}$-TiO_2 and Photo/H_2O_2/$Fe_{3-x}O_{4-y}$-TiO_2) were compared (Fig. 5). It was observed that the removal of the CIP antibiotic occurred in all tested processes.

No differences were observed between the process of direct photolysis and photocatalysis in the presence of particles without peroxidation. Thus, in these processes, the removals ranged from 36 to 56%. This behavior is possibly related to the mass of particles used (0.22 g L^{-1}) that may have impaired irradiation or also due to the need for more than 120 min for degradation.

The systems (Photo/H_2O_2/$Fe_{3-x}O_{4-y}$-TiO_2) with the heat treatments of 400 and 800 °C were the photocatalysts that presented the best performance, showing a percentage of degradation greater than 80%. This system was 30% more efficient than the direct photolysis process, indicating that the materials improved the photoperoxidation process (68%). Also, results showed that the particles with heat treatment of 100 °C presented low degradation efficiency, indicating that the absence of crystalline structures of the particles in the Photo/H_2O_2/$Fe_{3-x}O_{4-y}$-TiO_2 particle impairs the degradation of the CIP in the medium tested.
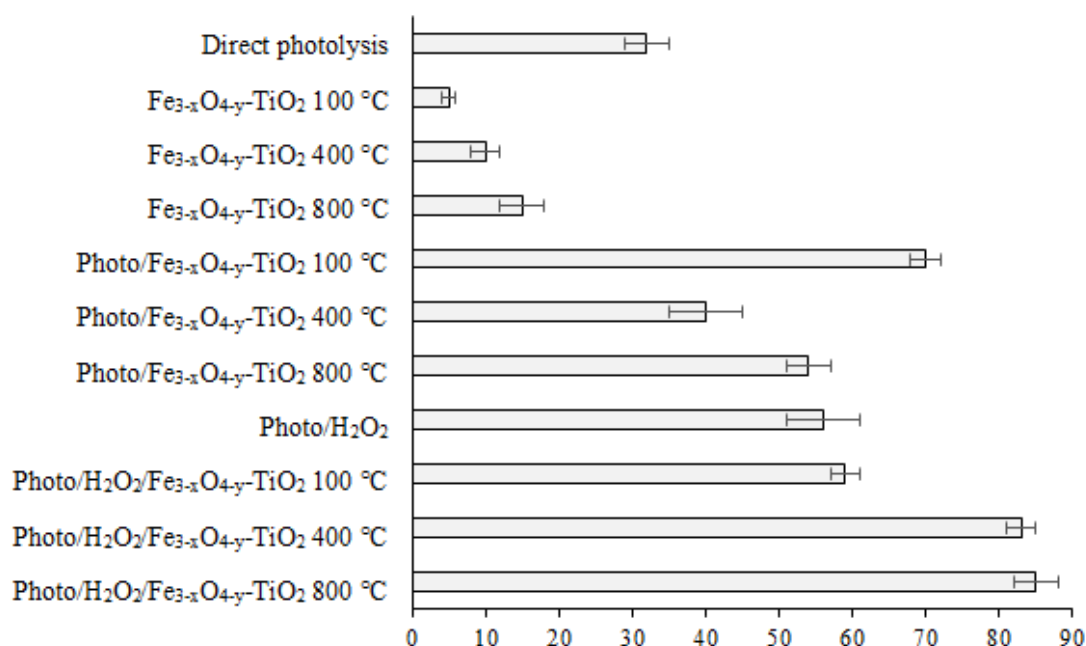
Figure 5. Ciprofloxacin removal during the tested degradation processes. Experimental condition: t = 120 min, $[CIP]_0 = 10$ mg L^{-1}, pH = 9, $H_2O_2 = 31$ mg L^{-1} and [Particles] = 0.22 g L^{-1}.

Hence, direct photolysis alone could not be used as an important procedure for the removal of CIP from aqueous solutions. As can be seen in Fig. 5, the removal of CIP via adsorption onto $Fe_{3-x}O_{4-y}$-TiO_2 (6 to 14 %) was lower in comparison to the photocatalysis process.

Fe_3O_4@SiO_2@TiO_2 particles with heat treatment of 500 and 600 °C were evaluated as a heterogeneous photocatalysis with H_2O_2 in a reactor composed of six lamps of 8 W, pH of 5.5, and CIP degradations of 83 and 95%, respectively, were reported over a test time of 90 min (Teixeira *et al.*, 2017). These results were similar to those obtained in this study.

Considering the photocatalyzed peroxidation process by the particles synthesized in the 800 °C heat treatment exhibited the best performance (Fig. 4), this system was evaluated through the kinetic study (Fig. 6).

It was observed that the most intense degradation of the CIP occurs in the first 60 min; this time interval corresponds to the dynamic range and might be related to factors such as the maximum amount of H_2O_2 favorable to the mechanism or the competition with by-products that were formed (Fioreze *et al.*, 2014). After 60 min, low degradation rates were observed, indicating that the system tends to stabilize, keeping the concentration of residual CIP constant.
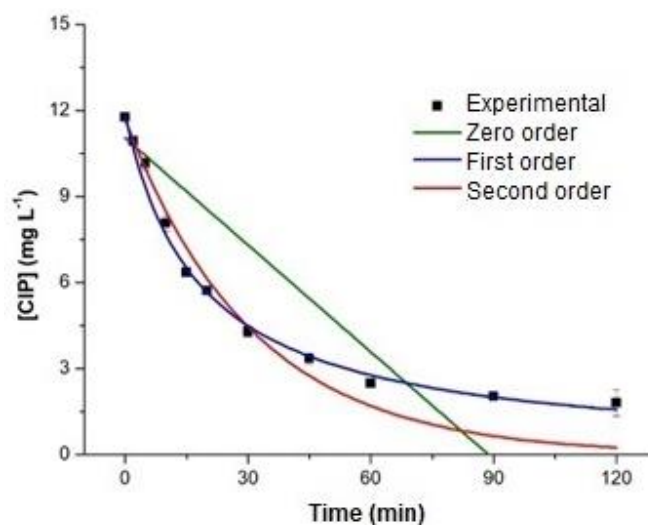

Figure 6. Kinetic study of the photo/H_2O_2/$Fe_{3-x}O_{4-y}$-TiO_2 process applied to CIP degradation. T = 120 min, $[CIP]_0 = 12$ mg L^{-1}, pH = 9, $H_2O_2 = 31$ mg L^{-1} and [Particles] = 0.22 g L^{-1}.

From the R^2 coefficients (Tab. 1), it was possible to determine that the model that presented the best fitting of experimental data was the first order with R^2 of 99.7%; such a model assumes that, in a speed reaction, it is directly dependent on the concentration of the reagents.

Table 1. Kinetic data for Photo/H_2O_2/$Fe_{3-x}O_{4-y}$-TiO_2 process. t = 120 min, $[CIP]_0$ = 12 mg L^{-1}, pH = 9, H_2O_2 = 31 mg L^{-1} and [Particles] = 0.22 g L^{-1}.

Zero order			First order			Second order		
k_0 (mg L^{-1} min^{-1})	$t_{1/2}$ (min)	R^2	k_1 (min^{-1})	$t_{1/2}$ (min)	R^2	k_2 (L mg^{-1} min^{-1})	$t_{1/2}$ (min)	R^2
0.12 (± 0.02)	44.5	80.9	0.05 (± 0.002)	16.9	99.7	0.03 (± 0.003)	23.1	97.9

Based on the first-order model, it was observed that, in 16.9 min, the CIP concentration was reduced to half of its initial value. The rate constant (k) was 0.05 min^{-1}. Similarly, a study using $Fe_3O_4@SiO_2@TiO_2$ in CIP photodegradation presented the first-order constant of 0.017 min^{-1} (Teixeira *et al.*, 2017). Also, the degradation of CIP with an initial concentration of 20 mg L^{-1} was studied by the photocatalysis process using a $Fe_3O_4@TiO_2@C$-dot particle exposed to a mercury vapor lamp. The kinetic model followed first-order with a k = 0.0154 min^{-1} during 150 min of testing (Das *et al.*, 2016).

A heterogeneous photocatalysis study using TiO_2 obtained 57% efficiency in CIP removal over 120 min of testing in a reactor equipped with 16 W UV lamps. The reported model was also first-order with a rate constant of 0.0063 min^{-1} (Hassani *et al.*, 2015).

Comparing the data obtained here for the photodegradation of CIP with studies reported in the literature, it is clear that $Fe_{3-x}O_{4-y}$-TiO_2 heat-treated at 800 °C is a promising catalyst for CIP degradation.

4. Conclusions

Here, the facile and reproducible preparation of $Fe_{3-x}O_{4-y}$-TiO_2 particles was reported, combining the use of the TiO_2 catalyst with the magnetic properties of iron oxide.

In the conditions explored, the photocatalysts showed degradation percentages between 40 and 85%, in which the Photo/H_2O_2/$Fe_{3-x}O_{4-y}$-TiO_2 process with the particles synthesized in the 800 °C heat treatment exhibited the best performance.

The kinetic study revealed that $Fe_{3-x}O_{4-y}$-TiO_2 catalyst followed first-order kinetics during the 120 min reaction. The use of a large amount of catalyst has some limitations, such as low degradation, for example, possibly because the dispersed particles interfere with the incident radiation. Despite this, the process is attractive, since it eliminates the need for a robust wastewater post-treatment step to remove the suspended catalyst.

Thus, although other factors must be evaluated for real scale usage, such as the analysis and removal of by-products formed, using, for example, chromatography liquid techniques coupled to mass spectrometry, the heterogeneous photocatalysis process using the synthesized particles is a promising treatment in the CIP degradation.

Authors' contribution

Conceptualization: Costa Junior, I. L.; Giona, R. M.; Ferreira, K. A.; Kappes, C. A.
Data curation: Costa Junior, I. L.; Giona, R. M.
Formal Analysis: Costa Junior, I. L.; Ferreira, K. A.; Kappes, C. A.
Funding acquisition: Not applicable
Investigation: Costa Junior, I. L.; Giona, R. M.; Ferreira, K. A.; Kappes, C. A.
Methodology: Costa Junior, I. L.; Giona, R. M.
Project administration: Costa Junior, I. L.
Resources: Not applicable
Software: Not applicable
Supervision: Costa Junior, I. L.
Validation: Costa Junior, I. L.; Ferreira, K. A.; Kappes, C. A.
Visualization: Giona, R. M.
Writing – original draft: Costa Junior, I. L.; Giona, R. M.; Ferreira, K. A.; Kappes, C. A.
Writing – review & editing: Costa Junior, I. L.; Giona, R. M.

Data availability statement

All data sets were generated or analyzed in the current study.

References

Barancheshme, F.; Munir, M. Development of antibiotic resistance in wastewater treatment plants. In *Antimicrobial resistance: A global threat*; IntechOpen, 2019; pp 75–91. https://doi.org/10.5772/intechopen.81538

Barret, M.; Carrère, H.; Latrille, E.; Wisniewski, C.; Patureau, D. Micropollutant and sludge characterization for modeling sorption equilibria. *Environ. Sci. Technol.* **2010**, *44* (3), 1100–1106. https://doi.org/10.1021/es902575d

Borges, E.; García, D. M.; Hernández, T.; Ruiz-Morales, J. C.; Esparza, P. Supported photocatalyst for removal of emerging contaminants from wastewater in a continuous packed-bed photoreactor configuration. *Catalysts* **2015**, *5* (1), 77–87. https://doi.org/10.3390/catal5010077

Borges, S. S.; Xavier, L. P. S.; Silva, A. C.; Aquino, S. F. Imobilização de dióxido de titânio em diferentes materiais suporte para o emprego em fotocatálise heterogênea. *Quím. Nova* **2016**, 39 (7), 836–844. https://doi.org/10.5935/0100-4042.20160106

Bound, J. P.; Kitsou, K.; Voulvoulis, N. Household disposal of pharmaceuticals and perception of risk to the environment. *Environ. Toxicol. Pharmacol.* **2006**, *21* (3), 301–307. https://doi.org/10.1016/j.etap.2005.09.006

Carabineiro, S. A. C.; Thavorn-amornsri, T.; Pereira, M. F. R.; Serp, P.; Figueiredo, J. L. Comparison between activated carbon; carbon xerogel and carbon nanotubes for the adsorption of the antibiotic ciprofloxacin. *Catal. Today* **2012**, (1), 29–34. https://doi.org/10.1016/j.cattod.2011.08.020

Carlson, J. C.; Stefan, M. I.; Parnis, J. M.; Metcalfe, C. D. Direct UV photolysis of selected pharmaceuticals, personal care products and endocrine disruptors in aqueous solution. *Water Res.* **2015**, *84*, 350–361. https://doi.org/10.1016/j.watres.2015.04.013

Ciccotti, L.; Vale, L. A. S.; Hewer, T. L. R.; Freire, R. S. Fe_3O_4@TiO_2 preparation and catalytic activity in heterogeneous photocatalytic and ozonation processes. *Catal. Sci. Technol.* **2015**, *5* (2), 1143–1152. https://doi.org/10.1039/C4CY01242A

Costa Junior, I. L.; Pletsch, A. L.; Torres, Y. R. Ocorrência de fármacos antidepressivos no meio ambiente: Revisão. *Rev. Virtual Quím.* **2014**, *6* (5), 1408–1431. https://doi.org/10.5935/1984-6835.20140092

Das, R. K.; Kar, J. P.; Mohapatra S. Enhanced photodegradation of organic pollutants by carbon quantum dot (CQD) deposited Fe_3O_4@$mTiO_2$ nano-pom-pom balls. *Ind. Eng. Chem. Res.* **2016**, *55* (20), 5902–5910. https://doi.org/10.1021/acs.iecr.6b00792

Dorigon, L.; Frota, J. P. R. A.; Kreutz, J. C.; Giona R. M.; Moisés, M. P.; Bail, A. Synthesis and characterization of mesoporous silica-coated magnetite containing cetyltrimethylammonium bromide and evaluation on the adsorption of sodium dodecylbenzenesulfonate. *Appl. Surf. Sci.* **2017**, *420*, 954–962. https://doi.org/10.1016/j.apsusc.2017.05.249

Fabbri, D.; López-Muñoz, M. J.; Daniele, A.; Medana, C.; Calza, P. Photocatalytic abatement of emerging pollutants in pure water and wastewater effluent by TiO_2 and Ce-ZnO: Degradation kinetics and assessment of transformation products. *Photochem. Photobiol. Sci.* **2019**, *18* (4), 845–852. https://doi.org/10.1039/C8PP00311D

Fioreze, M.; Santos, E. P.; Schmachtenberg, N. Processos oxidativos avançados: Fundamentos e aplicação ambiental. *Revista Eletrônica em Gestão; Educação e Tecnologia Ambiental* **2014**, *18* (1), 79–91. https://doi.org/10.5902/2236117010662

Frade, V. M. F; Dias, M.; Teixeira, A. C. S. C.; Palma, M. S. A. Environmental contamination by fluoroquinolones. *Braz. J. Pharm. Sci.* **2014**, *50* (1), 41–54. https://doi.org/10.1590/S1984-82502011000100004

Halling-Sørensen, B.; Holten Lützhøft, H.-C.; Andersen, H. R.; Ingerslev, F. Environmental risk assessment of antibiotics: Comparison of mecillinam; trimethoprim and ciprofloxacin. *J. Antimicrob. Chemother.* **2000**, *46* (Sippl.1), 53–58. https://doi.org/10.1093/jac/46.suppl_1.53

Hassani, A.; Khataee, A.; Karaca, S. Photocatalytic degradation of ciprofloxacin by synthesized TiO_2 nanoparticles on montmorillonite: Effect of operation parameters and artificial neural network modeling. *J. Mol. Catal. A Chem.* **2015**, *409*, 149–161. https://doi.org/10.1016/j.molcata.2015.08.020

Hörsing, M.; Kosjek, T.; Andersen, H. R.; Heath, E.; Ledin, A. Fate of citalopram during water treatment with O_3, ClO_2, UV and fenton oxidation. *Chemosphere* **2012**, *89* (2), 129–135. https://doi.org/10.1016/j.chemosphere.2012.05.024

Hyland, K. C.; Dickenson, E. R. V.; Drewes, J. E.; Higgins, C. P. Sorption of ionized and neutral emerging trace organic compounds onto activated sludge from different wastewater treatment configurations. *Water Res.* **2012**, *46* (6), 1958–1968. https://doi.org/10.1016/j.watres.2012.01.012

Karkman, A.; Do, T. T.; Walsh, F.; Virta, M. P. J. Antibiotic-resistance genes in waste water. *Trends Microbiol.* **2018**, *26* (3), 220–228. https://doi.org/10.1016/j.tim.2017.09.005

Khashan, S; Dagher S; Tit N; Alazzam A; Obaidat I. Novel method for synthesis of Fe_3O_4@TiO_2 core/shell nanoparticles. *Surf. Coat. Technol.* **2017**, *322*, 92–98. https://doi.org/10.1016/j.surfcoat.2017.05.045

Leung, H. W.; Minh, T. B.; Murphy, M. B.; Lam, J. C. W.; So, M. K.; Martin, M.; Lam, P. K. S.; Richardson, B. J. Distribution; fate and risk assessment of antibiotics in sewage treatment plants in Hong Kong, South China. *Environ. Int.* **2012**, *42*, 1–9. https://doi.org/10.1016/j.envint.2011.03.004

Liu, F.; Nielsen, A. H.; Vollertsen, J. Sorption and degradation potential of pharmaceuticals in sediments from a stormwater retention pond. *Water* **2019**, *11* (3), 526. https://doi.org/10.3390/w11030526

Luo, Y.; Guo, W.; Ngo, H. H.; Nghiem, L. D.; Hai, F. I.; Zhang, J.; Liang, S.; Wang, X. C. A review on the occurrence of micropollutants in the aquatic environment and their fate and removal during wastewater treatment. *Sci. Total Environ.* **2014**, *473–474*, 619–641. https://doi.org/10.1016/j.scitotenv.2013.12.065

Mourão, H. A. J. L.; Mendonça, V. R; Malagutti, A. R.; Ribeiro, C. Nanoestruturas em fotocatálise: Uma revisão sobre estratégias de síntese de fotocatalisadores em escala nanométrica. *Quím. Nova* **2009**, *32* (8), 2181–2190. https://doi.org/10.1590/S0100-40422009000800032

Nogueira, R. F. P.; Jardim, W. F. A fotocatálise heterogênea e sua aplicação ambiental. *Quím. Nova* **1998**, *21* (1), 69–72. https://doi.org/10.1590/S0100-40421998000100011

Noval, V. E.; Carriazo, J. G. Fe_3O_4-TiO_2 and Fe_3O_4-SiO_2 core-shell powders synthesized from industrially processed magnetite (Fe_3O_4) microparticles. *Mat. Res.* **2019**, *22* (3), e20180660. https://doi.org/10.1590/1980-5373-mr-2018-0660

Oliveira, M.; Frihling, B. E. F.; Velasques, J.; Magalhães Filho, F. J. C.; Cavalheri, P. S; Migliolo, L. Pharmaceuticals residues and xenobiotics contaminants: Occurrence; analytical techniques and sustainable alternatives for wastewater treatment. *Sci. Total Environ.* **2020**, *705*, 135568. https://doi.org/10.1016/j.scitotenv.2019.135568

Pang, S. C.; Kho, S. Y.; Chin, S. F. Fabrication of magnetite/silica/titania core-shell nanoparticles. *J. Nanomater.* **2012**, *2012*, 427310. https://doi.org/10.1155/2012/427310

Piai, L; Blokland, M; van der Wal, A.; Langenhoff, A. Biodegradation and adsorption of micropollutants by biological activated carbon from a drinking water production plant. *J. Hazard. Mater.* **2020**, *388*, 122028. https://doi.org/10.1016/j.jhazmat.2020.122028

Rajasulochana, P.; Preethy, V. Comparison on efficiency of various techniques in treatment of waste and sewage water: A comprehensive review. *Resource-Efficient Technologies* **2016**, *2* (4), 175–184. https://doi.org/10.1016/j.reffit.2016.09.004

Rasalingam, S.; Peng, R.; Koodali, R. T. Removal of hazardous pollutants from wastewaters: Applications of TiO_2-SiO_2 mixed oxide materials. *J. Nanomater.* **2014**, *2014*, 617405. https://doi.org/10.1155/2014/617405

Rogowska, J.; Cieszynska-Semenowicz, M.; Ratajczyk, W.; Wolska, L. Micropollutants in treated wastewater. *Ambio* **2020**, *49*, 487–503. https://doi.org/10.1007/s13280-019-01219-5

Sarkar, S.; Chakraborty, S.; Bhattacharjee, C. Photocatalytic degradation of pharmaceutical wastes by alginate supported TiO_2 nanoparticles in packed bed photo reactor (PBPR). *Ecotoxicol. Environ. Saf.* **2015**, *121*, 263–270. https://doi.org/10.1016/j.ecoenv.2015.02.035

Sim, W.-J.; Lee, J.-W.; Oh, J.-E. Occurrence and fate of pharmaceuticals in wastewater treatment plants and rivers in Korea. *Environ. Pollut.* **2010**, *158* (5), 1938–1947. https://doi.org/10.1016/j.envpol.2009.10.036

Souza, F. S.; Silva, V. V.; Rosin, C. K.; Hainzenreder, L.; Arenzon, A.; Féris, L. A. Comparison of different advanced oxidation processes for the removal of amoxicillin in aqueous solution. *Environ. Technol.* **2018**, *39* (5), 549–557. https://doi.org/10.1080/09593330.2017.1306116

Teixeira, S.; Mora, H.; Blasse, L.-M.; Martins, P. M.; Carabineiro, S. A. C; Lanceros-Méndez, S.; Kühn, K.; Cuniberti, G. Photocatalytic degradation of recalcitrant micropollutants by reusable Fe_3O_4/SiO_2/TiO_2 particles. *J. Photochem. Photobiol. A Chem.* **2017**, *345*, 27–35. https://doi.org/10.1016/j.jphotochem.2017.05.024

Verlicchi, P.; Al Aukidy, M.; Zambello, E. Occurrence of pharmaceutical compounds in urban wastewater: Removal, mass load and environmental risk after a secondary treatment—A review. *Sci. Total Environ.* **2012**, *429*, 123–155. https://doi.org/10.1016/j.scitotenv.2012.04.028

Wei, J. H.; Leng, C. J.; Zhang, X. Z.; Li, W. H.; Liu, Z. Y.; Shi, J. Synthesis and magnetorheological effect of Fe_3O_4-TiO_2 nanocomposite. *J. Phys.: Conf. Ser.* **2009**, *149*, 012083. https://doi.org/10.1088/1742-6596/149/1/012083

Wu, W.; He, Q.; Jiang, C. Magnetic iron oxide nanoparticles: Synthesis and surface functionalization strategies. *Nanoscale Res. Lett.* **2008**, *3*, 397. https://doi.org/10.1007/s11671-008-9174-9

Wu, M.-H.; Que, C.-J.; Xu, G.; Sun, Y.-F.; Ma, J.; Xu, H.; Sun, R.; Tang, L. Occurrence; fate and interrelation of selected antibiotics in sewage treatment plants and their receiving surface water. *Ecotoxicol. Environ. Saf.* **2016**, *132*, 132–139. https://doi.org/10.1016/j.ecoenv.2016.06.006

Yang, J.; Chen, C.; Ji, H.; Ma, W.; Zhao, J. Mechanism of TiO_2-assisted photocatalytic degradation of dyes under visible irradiation: Photoelectrocatalytic study by TiO_2-film electrodes. *J. Phys. Chem. B* **2005**, *109* (46), 21900–21907. https://doi.org/10.1021/jp0540914

Screening of coformers for quercetin cocrystals through mechanochemical methods

Fayene Zeferino Ribeiro de Souza[1] , Amanda Cosmo de Almeida[1] , Patrícia Osorio Ferreira[1] , Richard Perosa Fernandes[2] , Flávio Junior Caires[1+]

1. São Paulo State University, School of Science, Bauru, Brazil.
2. São Paulo State University, Institute of Chemistry, Araraquara, Brazil.

+**Corresponding author:** Flávio Junior Caires, **Phone:** +55 14 3103-9830, **Email address:** flavio.caires@unesp.br

ABSTRACT: Quercetin (QUE) is a nutraceutical compound that exhibits pharmacological properties such as antioxidant, cardioprotective, anti-ulcer, and anti-inflammatory effects. Although QUE is well-known for its benefits, its efficacy is limited due to low solubility. Thus, cocrystallization acts as an interesting approach to improve the solubility—among other properties—of this compound. In this work, cocrystallization screening was applied through neat grinding (NG) and liquid-assisted grinding (LAG), in which QUE and four cocrystal formers (benzamide, picolinamide, isonicotinamide,

and pyrazinoic acid) were tested. The precursors and QUE-coformer systems were characterized using thermoanalytical techniques (TG-DTA), X-ray powder diffraction (XRPD), and Fourier transform infrared (FTIR) spectroscopy. The results showed the formation of QUE cocrystals with picolinamide and isonicotinamide coformers in a 1:1 stoichiometric ratio. Furthermore, although coformers are isomers, spectroscopic and thermal data suggest that the supramolecular synthons involved in cocrystallization are different.
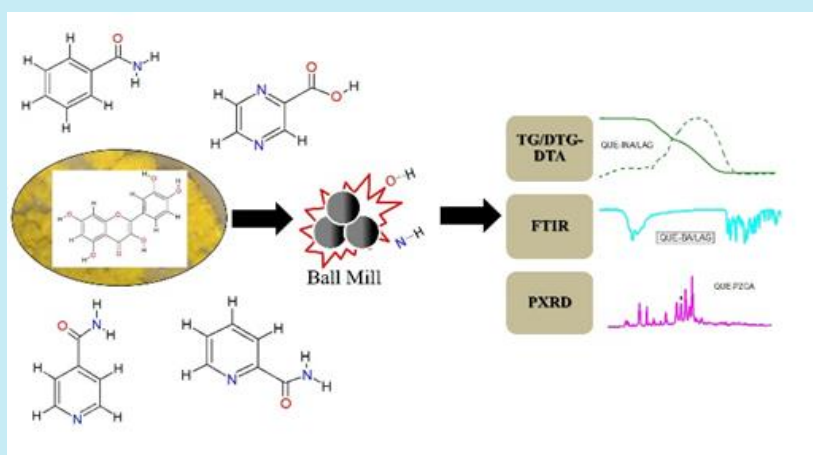
1. Introduction

Nutraceuticals are chemical compounds present in functional foods with medicinal benefits, which aid in the prevention and treatment of diseases. Among them are vast natural products such as phenolic acids, coumarins, vitamins, and compounds from the flavonoid class, including quercetin (QUE) (Madaan *et al.*, 2016; Sinha *et al.*, 2015; Thakuria and Sarma, 2018).

Quercetin is a polyphenol flavonoid commonly found in many types of fruits, vegetables, and teas, being more abundant in onions (Tang *et al.*, 2016). This important flavonol shows biological properties, including antioxidant, cardioprotective, anti-ulcer, and anti-inflammatory effects (Madaan *et al.*, 2016; Varzakas *et al.*, 2016; Vasisht *et al.*, 2016). Although QUE is well-known for its therapeutic bioactivity, this substance is classified as class II in Biopharmaceutical Classification System (BCS), with low aqueous solubility and high permeability, which limits its efficacy (Sinha *et al.*, 2015). Given this context, approaches such as cocrystallization have been employed aiming at the improvement of physical-chemical properties, like solubility, stability, bioavailability, and others, without changing therapeutic properties (Aakeröy *et al.*, 2009; Madaan *et al.*, 2016; Su *et al.*, 2015).

Cocrystal is a crystalline material formed through non-covalent intermolecular interactions, as Van der Waals forces, hydrogen bonding, π-π interactions, halogen bonding, and others without proton transfer. In terms of applicability in the pharmaceutical field, the cocrystal could be designed by an active pharmaceutical ingredient (API) and a nontoxic and safe substance for consumption, known as coformer (Panzade *et al.*, 2017; Yadav *et al.*, 2009).

The QUE molecule can form intermolecular interactions through its five hydroxyl groups that provide several different conformations, making it possible to establish supramolecular synthons (Dubey and Desiraju, 2015). Thus, the coformers of benzamide (BA), picolinamide (PA), isonicotinamide (INA), and pyrazinoic acid (PZCA) were selected based on safety and the possibility of their functional groups interacting with quercetin. Although the INA coformer has been reported to form a QUE–INA cocrystal synthesized via the slurry method (Smith *et al.*, 2011), here the preparation of this cocrystal was investigated through grinding methods. The structural formulas of quercetin and coformers are shown in Fig. 1.
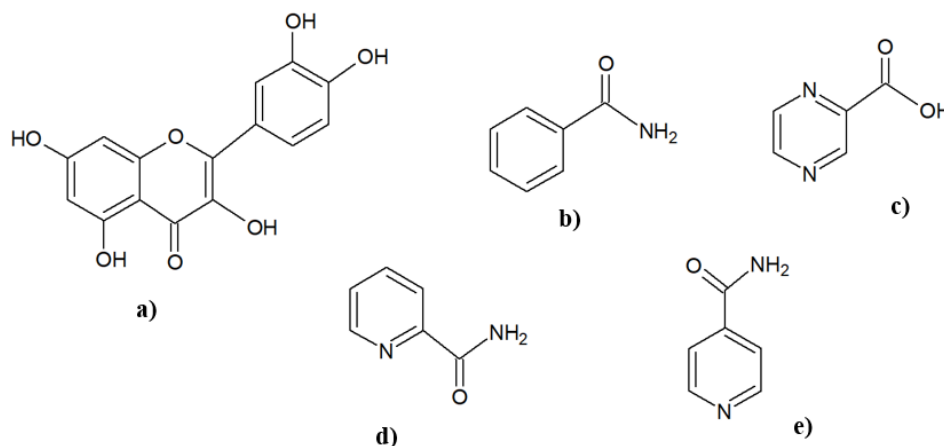

Figure 1.Structural formula of quercetin (**a**) and the coformers benzamide (**b**), pyrazinoic acid (**c**), picolinamide (**d**), isonicotinamide (**e**).

Many APIs that have problems related to their physicochemical properties highlight the importance of the cocrystals approach by the pharmaceutical industry. Moreover, the new crystal form resulting from the interaction between an API and another molecule could be patented, as in the already marketed Entresto, Steglatro, Depakote, Lexapro, and others (Karagianni *et al.*, 2018; Karimi-Jafari *et al.*, 2018; Kavanagh *et al.*, 2019; Patel *et al.*, 2019; Qiao *et al.*, 2011; Rajput *et al.*, 2013; Sathisaran and Dalvi, 2018; Yousef and Vangala, 2019).

Given the context, this work describes cocrystal screening for QUE employing four coformers by two different mechanochemical methods, neat grinding (NG) and liquid-assisted grinding (LAG), performing spectroscopic and diffractometric characterization, and thermoanalytical studies.

2. Experimental part

2.1 Materials

Benzamide, PA, INA, and PZCA (all with >99% purity) were purchased from Sigma Aldrich, QUE (95.0% dry extract) was purchased from a local drugstore. The liquid used during the LAG method was ethanol (99.5% purity), purchased from Dinâmica. All reactants were used without further purification.

2.2 Methods

The mechanochemical synthesis was performed using two solid-state based methods, LAG and NG grindings were performed in a ball mill (Retsch, MM 400 model) using 10 mL stainless steel jars and 7 mm stainless steel balls, under a grinding frequency of 30 Hz for 30 min. The total mass of the milled sample was 500 mg in the molar ratio of 1:1 between the drug and each coformer. The amount of liquid (ethanol) added in the LAG synthesis was 0.25 μL mg^{-1} ratio (volume/total sample mass), based on studies by Friščić et al. (2009).

Simultaneous thermogravimetry-differential thermal analysis (TG-DTA) curves were obtained on a thermogravimetric analyzer (NETZCH, STA449 F3). The TG-DTA analyses, in the range of 30 to 800 °C, were performed with a heating rate of 10 °C min^{-1}, using an α-Al$_2$O$_3$ (70 μL) crucible under dynamic air atmosphere with a flow rate of 50 mL min^{-1}. The sample mass was approximately 5.0 mg.

X-ray powder diffraction (XRPD) analyzes were performed on the Rigaku MiniFlex 600 diffractometer, employing Cu Kα radiation (λ=1.54056 Å) in a 2θ range of 5° up to 50°, under continuous scan mode, with a rate of 4° min^{-1} and operating settings of 40 kV voltage and 15 mA current.

Infrared (FTIR) spectra were obtained using Nicolet iS10 FTIR spectrophotometer, Thermo Scientific, through an attenuated total reflectance method equipped with a germanium crystal, within a range of 675 to 4000 cm^{-1}, 32 scans per spectrum, 4 cm^{-1} of resolution.

To determine the solubility of the drug, the critical step is the quantification of the drug dissolved in the medium, since it is necessary to use a validated analytical method. It was already tried to quantify the drug using UV-visible spectrophotometric method, but the developed method did not show selectivity, the coformer interfered in the drug quantification. Furthermore, as reported by Ramešová et al. (2012),

QUE is unstable in aqueous solution, which would make its quantification difficult.

3. Results and discussion

3.1 Quercetin–isonicotinamide (1:1) system

3.1.1 X-ray powder diffraction and FTIR

The first system prepared in this work was an alternative approach to that reported by Smith et al.(2011). Their work showed the synthesis of a QUE–INA cocrystal prepared through slurry crystallization, a solution-based method dissolving the starting materials in 5–6 mL of methanol. Given the context, the cocrystal was prepared using mechanochemical synthesis as it is a greener, less solvent, faster and reproducible approach. Therefore, the XRPD diffractograms and FTIR spectra of QUE, INA, and the QUE–INA systems are shown in Fig. 2.
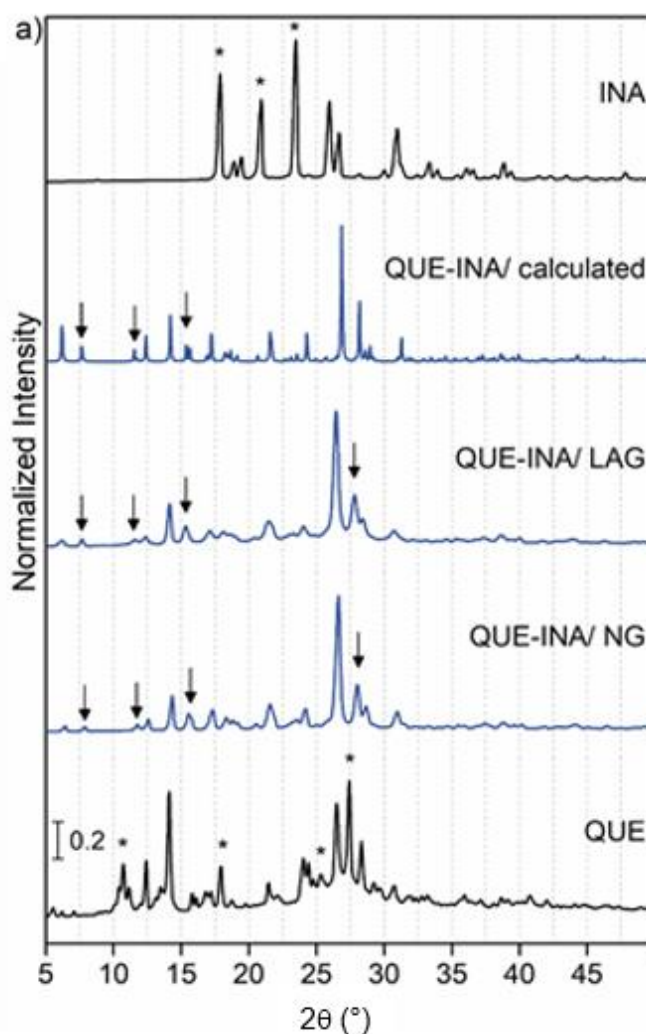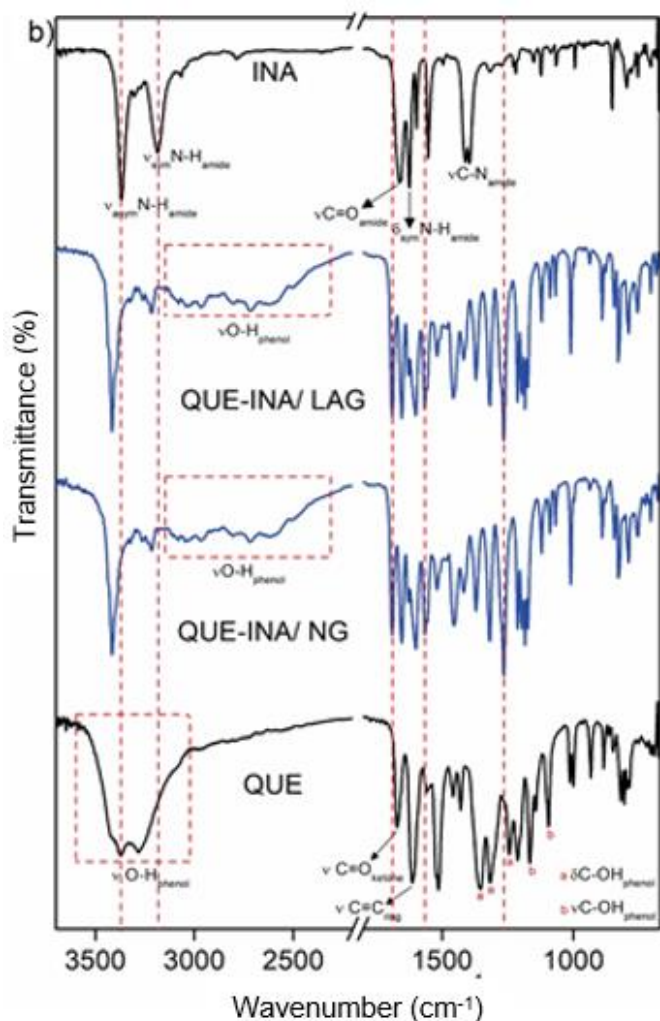
Figure 2. X-ray powder diffraction diffractograms **(a)** and FTIR spectra **(b)** of QUE, INA, and the QUE–INA (1:1) systems. (XRPD diffractogram calculated from the QUE–INA cocrystal was obtained using the Mercury program from the CIF file (CCDC Deposition Number: 1428198 of the crystalline structure reported by Smith *et al.* [2011])

The QUE–INA/NG and QUE–INA/LAG systems have the same diffraction pattern, with new diffraction peaks at 2θ equal to 7.9, 11.8, 15.5 and 28.0° and absence of diffraction peaks associated with the INA (17.9, 20.9 and 23.5°) and the QUE (5.5, 10.7, 17.9, 25.3 and 27.4°), confirming the formation of cocrystal. The diffractograms of these systems show the same diffraction pattern of the QUE–INA cocrystal reported in the literature that was obtained by the slurry method (Smith *et al.*, 2011), confirming that the synthesis method does not influence the crystalline phase formed and that the mechanochemical method is efficient in obtaining this cocrystal.

Regarding the FTIR data, the QUE spectrum shows the presence of strong broad bands with peaks at 3373 and 3281 cm^{-1} attributed to the O–H stretching vibrations (νO–H$_{phenol}$) of the phenol groups, a band at 1670 cm^{-1} attributed to the C=O stretching vibrations (νC=O$_{ketone}$) of the ketone carbonyl group, the bands at 1612 and 1212 cm^{-1} are attributed to the stretching vibrations of the aromatic ring (νC=C$_{ring}$) and the ether group (νC–O–C), respectively. The bands at 1355, 1316, and 1245 cm^{-1} are attributed to the C–OH bending vibrations of the phenol groups (δC–OH$_{phenol}$), and the bands at 1168 and 1097 cm^{-1} are attributed to the C–OH stretching vibrations of the phenol groups (νC–OH$_{phenol}$) (Nguyen and Jeong, 2018; Refat *et al.*, 2021).

The FTIR spectrum of INA shows bands at 3370 and 3185 cm^{-1} attributed to the asymmetric and symmetrical N–H stretching vibrations (ν_{asym}N–H$_{amide}$ *and* ν_{sym}N–H$_{amide}$), a band at 1661 cm^{-1} attributed to C=O stretching vibrations (νC=O$_{amide}$), a band at 1625 cm^{-1} attributed to N–H bending vibrations (δN–H$_{amide}$) and a band at 1403 cm^{-1} attributed to C–N stretching vibrations (νC–N$_{amide}$) (Yurdakul and Ataç, 2004).

The FTIR spectra of the QUE–INA/LAG and QUE–INA/NG systems are similar to each other and present significant changes in relation to the spectra of isolated precursors, suggesting the establishment of new supramolecular synthons in the solid-state. The ν_{asym}N–H and ν_{sym}N–H bands are shifted to higher absorption frequency values, and the intensity of ν_{sym}N–H band decreased significantly. Another significant change is associated with the νO–H$_{phenol}$ band, its intensity decreases, it became wider and shifted to a region of frequencies between 2316 and 3115 cm^{-1}, indicating the presence of hydrogen bonds of OH$_{(phenol)}$···N$_{(aromatic)}$ between the molecules (Rautenberg *et al.*, 2020; Ravikumar *et al.*, 2013), in accordance with the data of crystal structure reported by Smith *et al.* (2011). The bands associated with the vibrations of the carbonyl groups also undergo small displacements, the νC=O$_{ketone}$ of QUE was shifted to 1690 cm^{-1}, and that of the νC=O$_{amide}$ of INA was shifted to 1651 cm^{-1}. Finally, the bands associated with νC–N$_{amide}$, δC–OH$_{phenol}$, and νC–OH$_{phenol}$ shifted to higher absorption frequency values.

3.1.2 Simultaneous thermogravimetry-differential thermal analysis

The thermoanalytical curves of the QUE, INA and the QUE–INA/NG and QUE–INA/LAG systems are shown in Fig. 3. The TG curve of QUE shows that it is

thermally stable up to 290 °C and undergoes mass loss in at least three steps. The first step of mass loss between 30–120 °C (Δm_{QUE} = 4.96%), without a thermal event in the DTA curve, is associated with dehydration of the compound since QUE is marketed in its hydrated form (Ravikumar *et al.*, 2013). The second and third steps, corresponding to exothermic events in the DTA curve, are attributed to thermal degradation and oxidation of QUE, respectively (Borghetti *et al.*, 2012; Costa *et al.*, 2002). The endothermic event at 310 °C in the DTA curve is associated with the melting followed by decomposition (Δm= 3.08%), as already reported in the literature (Borghetti *et al.*, 2012; Costa *et al.*, 2002).
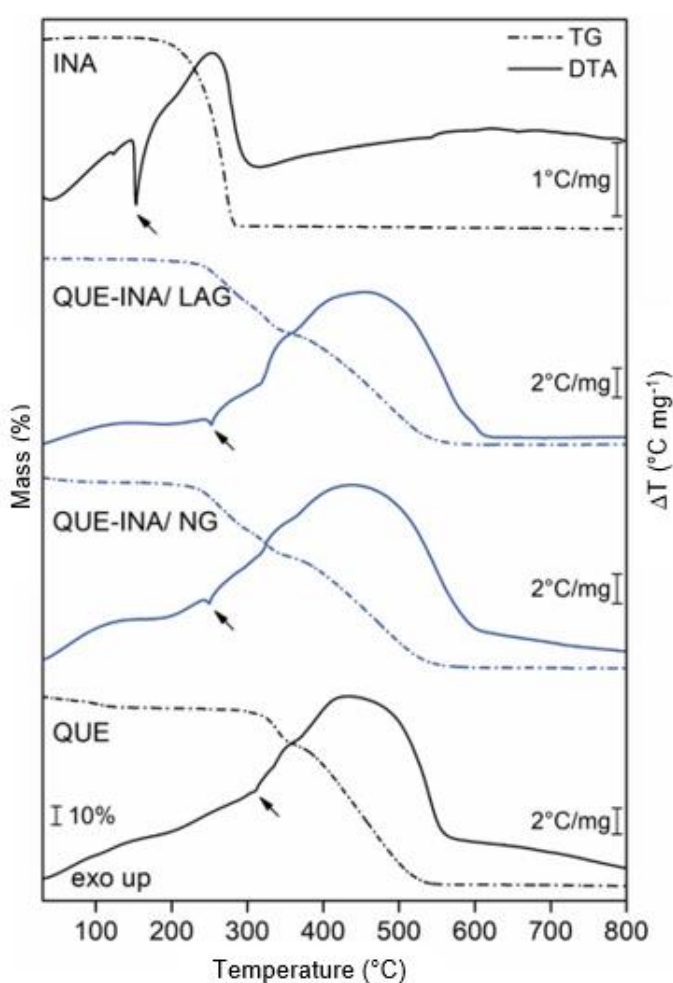

Figure 3. Simultaneous thermogravimetry-differential thermal analysis curves of QUE, INA, and the QUE–INA (1:1) systems (arrow: melting endothermic event).

The TG curve of INA shows a loss of mass in a single step between 175 and 285 °C, attributed to the evaporation of the compound. The two endothermic peaks at 123 and 153 °C in the DTA curve, without loss of mass on the TG curve, are associated with a phase transition (form II to form I) and the melting of the compound, respectively (Holanda *et al.*, 2019).

The thermoanalytical curves of the QUE–INA/NG and QUE–INA/LAG systems are similar, suggesting that the synthesis condition used does not significantly influence the formation of the multicomponent system, as already evidenced in the FTIR and XRPD data. These thermoanalytical curves show that the systems are thermally stable up to approximately 220 °C and undergo thermal decomposition in at least three overlapping mass loss steps, corresponding to endothermic and exothermic events in the DTA curve. The first step of mass loss, corresponding to an endotherm in the DTA curve, is attributed to the thermal decomposition of the QUE–INA system with the release of the INA coformer. The last two steps, corresponding to exothermic events in the DTA curve, are attributed to the thermal degradation of the remaining drug. The small endothermic peak at 252 °C in the DTA curve, already with a small mass loss in the TG curve, is attributed to the melting of the QUE–INA cocrystal, which has not yet undergone thermal degradation.

The thermal behavior presented by QUE–INA systems is quite different from that observed for isolated precursor compounds, which confirms the formation of the multicomponent solid form, according to the FTIR and XRPD results.

3.2 Quercetin–picolinamide (1:1) system

3.2.1 X-ray powder diffraction and FTIR

The XRPD diffractograms and FTIR spectra of the QUE, PA, and QUE–PA systems are shown in Fig. 4a and b, respectively.

The diffractograms of the QUE–PA/NG and QUE–PA/LAG systems present new diffraction peaks in 2θ equal to 5.1, 15.1, 20.1, 22.9, 25.7 and 36.7° and absence of peaks in 2θ equal to 5.5, 10.7, 14.1 and 17.9° (QUE) and 20.7 and 25.4° (PA), not being the combination of the diffractograms of its isolated precursors, which confirms the formation of the cocrystal. Furthermore, these results suggest that the addition of liquid in the mechanochemical synthesis does not significantly influence the formation of the new crystalline phase.

The FTIR spectrum of PA shows the spectral pattern reported for polymorph II of this compound (Akalin and Akyuz, 2006), which is the commonly marketed crystalline form. The main bands are observed at

3416 cm^{-1} attributed to asymmetric NH$_2$ stretching vibrations (ν_{asym}NH$_2$), two bands at 3275 and 3170 cm^{-1} attributed to symmetric NH$_2$ stretching vibrations (ν_{sym}NH$_2$), a band at 1660 cm^{-1} attributed to C=O stretching vibrations (νC=O$_{amide}$), a band at 1603 cm^{-1} attributed to NH$_2$ bending (scissoring) vibrations (δNH$_2$ scissoring) and a band at 1391 cm^{-1} attributed to C–N stretching vibrations of the amide group (νC–N$_{amide}$) (Akalin and Akyuz, 2006; Évora *et al.*, 2012).
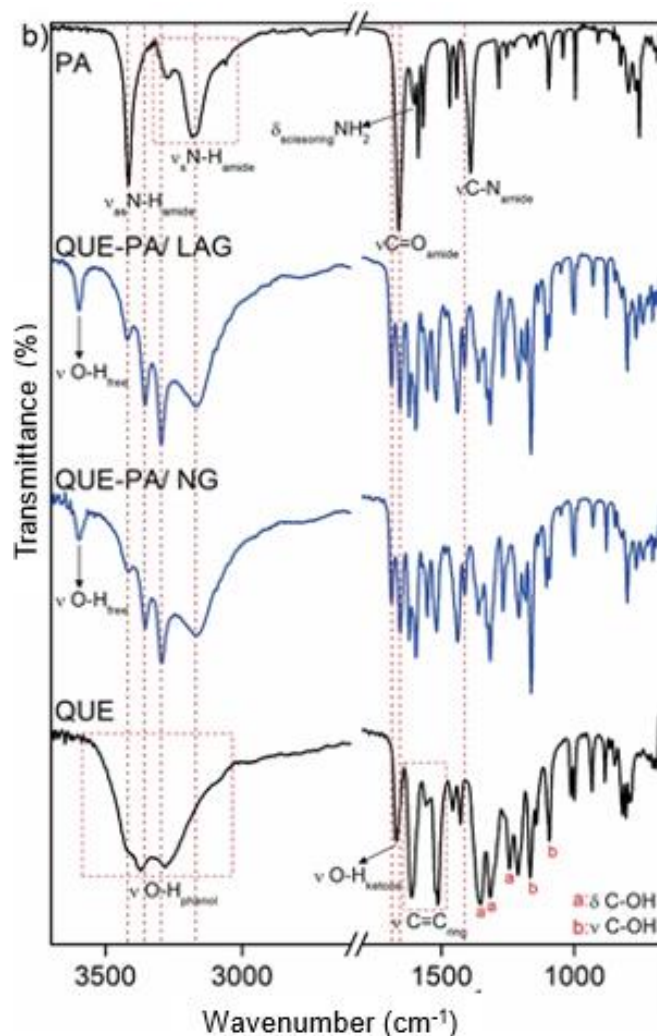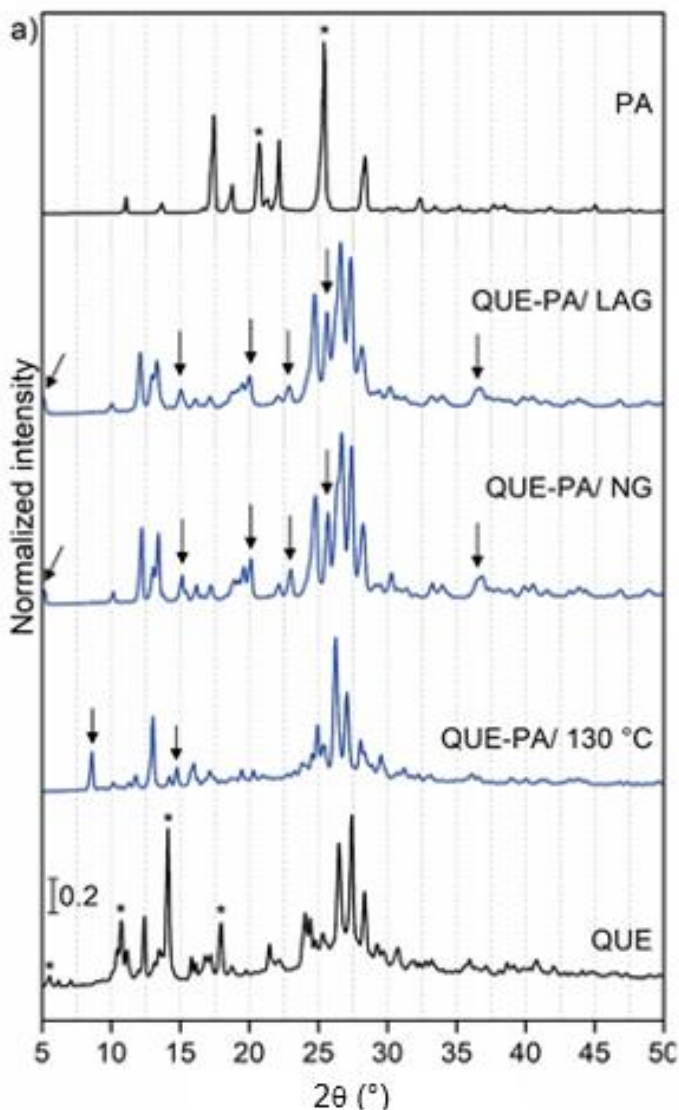

Figure 4. X-ray powder diffraction diffractograms **(a)** and FTIR spectra **(b)** of QUE, PA, and the QUE–PA (1:1) system**s**.

For the FTIR spectrum of the QUE–PA cocrystal, only small shifts in the bands associated with the functional groups of the precursors are observed, quite differently from the pronounced changes observed in the FTIR spectrum of the QUE–INA cocrystal. These results suggest that the supramolecular synthons established in the QUE–PA cocrystal are different from those present in the QUE–INA cocrystal, mainly due to the absence of changes in the spectra associated with the formation of the OH$_{(phenol)}$···N$_{(aromatic)}$ synthon, probably the ortho position of the aromatic nitrogen in the PA molecule prevents the formation of this intermolecular interaction. This is also supported by the appearance of a weak band at 3599 cm^{-1} attributed to O–H stretching vibrations of the free hydroxyl group (νO–H).

3.2.2 Simultaneous thermogravimetry-differential thermal analysis

The TG–DTA curves of QUE, PA, and QUE–PA systems are shown in Fig. 5. The TG curve of PA shows loss of mass in a single step between 130 and 235 °C, associated with a significant change in the baseline in the DTA curve, attributed to the vaporization of the compound. The endothermic peak at 105 °C in the DTA curve, without loss of mass in the TG curve, is attributed to the melting of the compound.
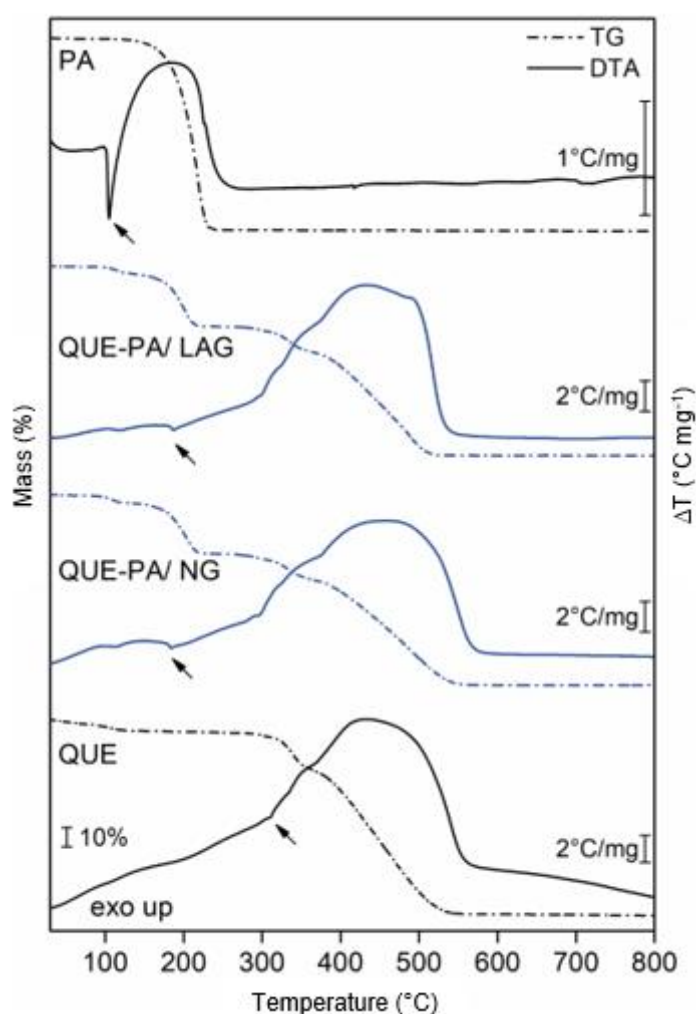

Figure 5. Simultaneous thermogravimetry-differential thermal analysis curves of QUE, PA, and the QUE–PA (1:1) systems (arrow: melting endothermic event).

The TG-DTA curves of the QUE–PA/NG and QUE–PA/LAG systems are very similar, suggesting that the condition of synthesis employed does not significantly influence the formation of the cocrystal, as already evidenced in the FTIR and XRPD data. These thermoanalytical curves show four steps of mass loss, corresponding to endothermic and exothermic events in the DTA curve. The first step, between 104 and 125 °C ($\Delta m_{\text{QUE-PA/ NG}}$ = 4.02%; $\Delta m_{\text{QUE-PA/ LAG}}$ = 3.16%), corresponding to a small endothermic event around 117 °C in the DTA curves, is attributed to the loss of a hydroxyl group ($\Delta m_{\text{calc.}}$ = 4.01%), probably free hydroxyl group, as indicated by the FTIR data. The XRPD diffractogram obtained from the sample heated to 130 °C, temperature above the first mass loss step, shows a new diffraction pattern, with a significant reduction in the number of diffraction peaks associated with cocrystal formation, decreased intensity, and displacement of other peaks and the appearance of two new peaks (2θ = 8.6 and 14.8°), suggesting that mass loss is associated with thermal degradation of the systems, as indicated by the calculated mass loss value.

After this first step, the remaining material is thermally stable up to 155 °C and undergoes thermal decomposition in three steps, between 155 and 525 °C. The second step, between 155 and 217 °C, is attributed to the thermal decomposition of the intermediate formed in the previous step with the release of PA (Δm_{TG} = 28.12%; $\Delta m_{\text{Calc.}}$ = 28.77%). The last two steps, between 281 and 525 °C, are associated with thermal degradation of the remaining degraded QUE. The endothermic peak at 185 °C in the DTA curve, with a slight loss of mass in the TG curve, is attributed to the melting of the material. The thermal behavior presented by QUE–PA systems is quite different from that observed for isolated compounds, which confirms the formation of a cocrystal, according to the FTIR and XRPD results.

3.3 Quercetin–pyrazinoic acid (1:1) system

3.3.1 X-ray powder diffraction and FTIR

The XRPD diffractograms and FTIR spectra of the QUE–PZCA systems (Fig. 6) are just a combination of the diffractograms and spectra of the precursors, since no new diffraction peaks and band shifts are observed, suggesting that these systems are simple physical mixtures or eutectic mixtures.
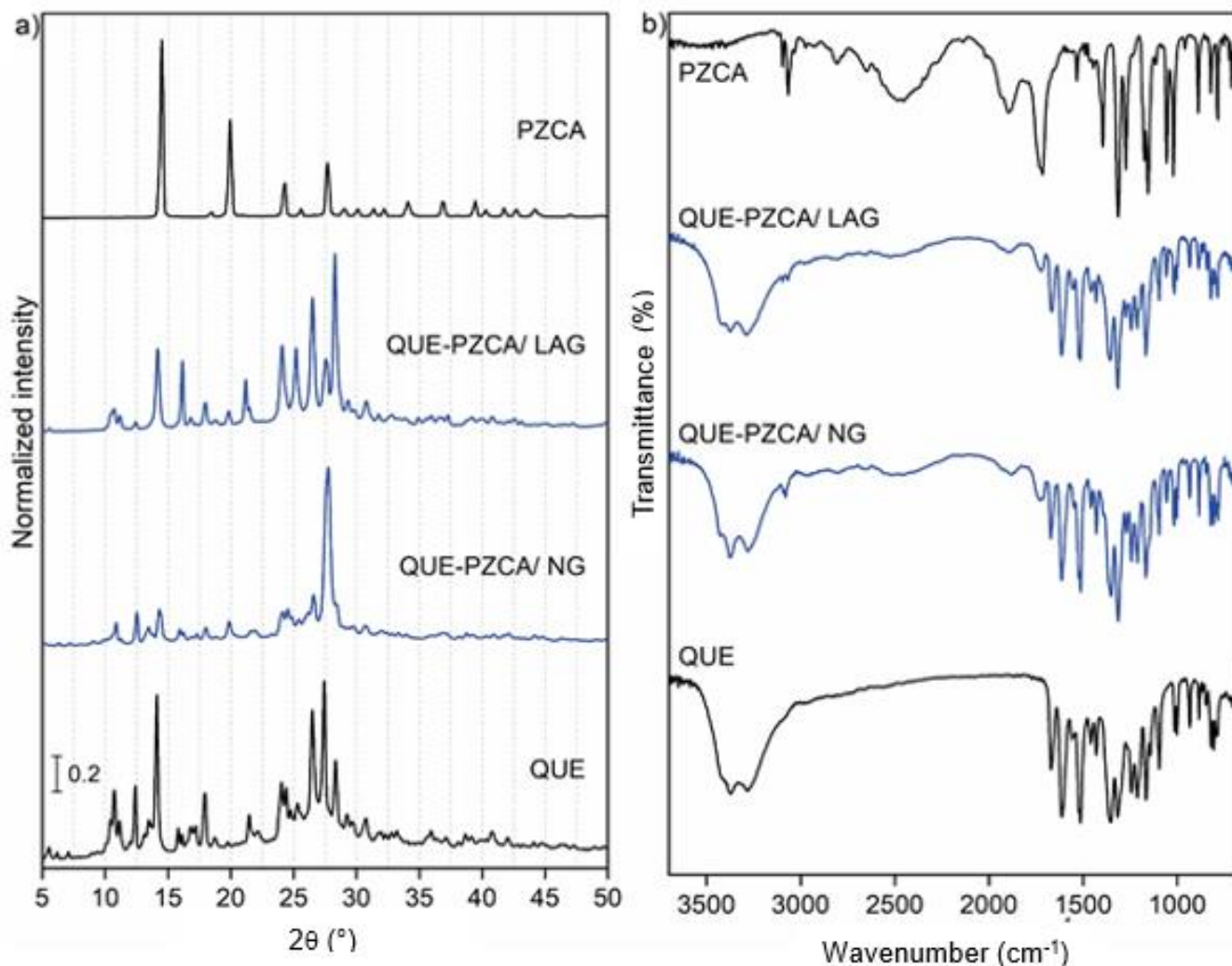
Figure 6. X-ray powder diffraction diffractograms (**a**) and FTIR spectra (**b**) of QUE, PZCA, and the QUE–PZCA (1:1) systems.

3.3.2 Simultaneous thermogravimetry-differential thermal analysis

The TG–DTA curves of the QUE, PZCA and the systems QUE–PZCA are shown in Fig. 7.

The TG–DTA curves of the PZCA show loss of mass in a single step between 160 and 229 °C, corresponding to partial sublimation and vaporization of the compound. The endothermic peak at 223 °C in the DTA curve is attributed to the melting of the compound (Almeida *et al.*, 2020).

The TG-DTA curves of the QUE–PZCA/LAG and QUE–PZCA/NG systems have similar thermal stability and the same three steps of mass loss. The first step, corresponding to a small endothermic peak at 207 °C in the DTA curve, is attributed to the sublimation and vaporization of PZCA. The second and third steps, associated with endothermic and exothermic events in the DTA curve, respectively, are associated with the

thermal degradation of QUE. In addition, the thermal profile and mass loss temperatures observed in the TG-DTA curves of the QUE–PZCA systems are similar to those observed in the TG-DTA curves of the isolated precursors, being the combination of the thermoanalytical curves of the isolated precursors. On the other hand, the thermal melting events of the precursors are not observed in the DTA curves of the systems, which may be related to the sensitivity of the DTA measurement and the lower amount of compound present in the QUE–PZCA systems.

The observed thermal behavior, together with the FTIR and XRPD data, confirm that QUE–PZCA systems are just simple physical mixtures.
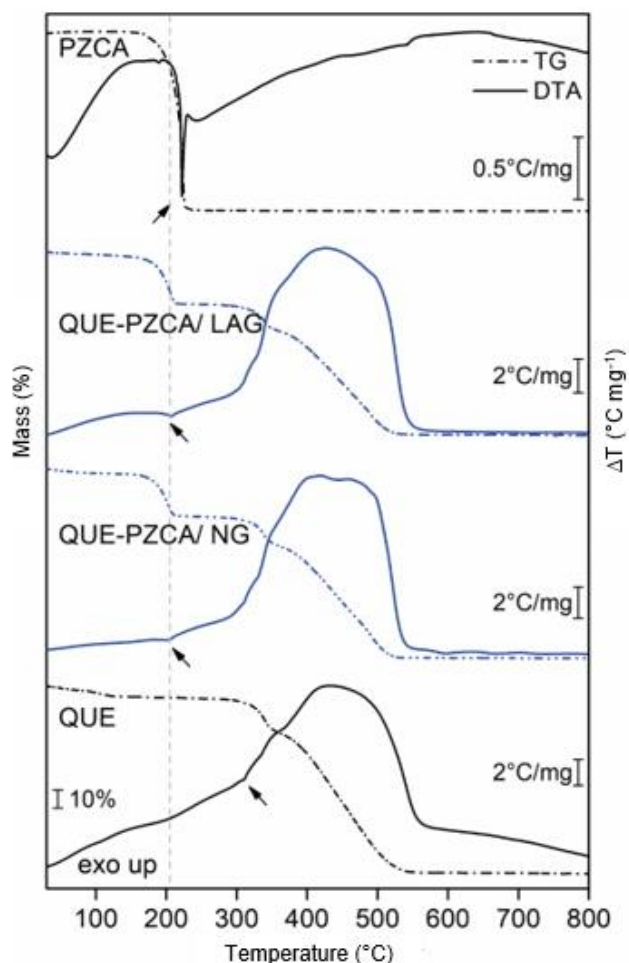
Figure 7. Simultaneous thermogravimetry-differential thermal analysis curves of QUE, PZCA, and the QUE–PZCA (1:1) systems.

3.4 Quercetin–benzamide (1:1) system

3.4.1 X-ray powder diffraction and FTIR

The XRPD diffractograms and FTIR spectra of the QUE–BA systems and their precursors are shown in Fig. 8.

As can be seen, both systems have similar diffraction and spectral patterns, corresponding to the combination of diffractograms and spectra of the starting materials, since no new diffraction peaks and band shifts are observed. This suggests that no new crystalline phases were formed, nor supramolecular synthons were established, which indicates that these systems are simple physical mixtures or eutectic mixtures.
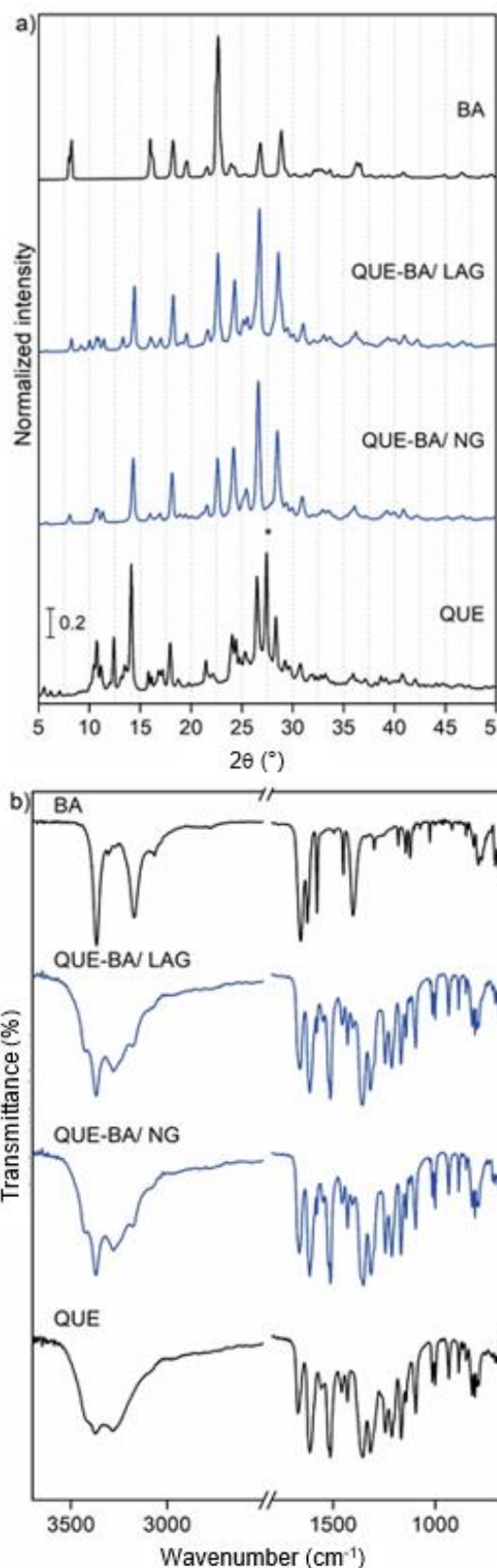

Figure 8. X-ray powder diffraction diffractograms **(a)** and FTIR spectra **(b)** of QUE, BA, and the QUE–BA (1:1) systems.

3.4.2 Simultaneous thermogravimetry-differential thermal analysis

The TG-DTA curves of the QUE, BA and the systems QUE–BA are shown in Fig. 9.

The TG-DTA curves of benzamide show mass loss in a single step between 155 and 255 °C, corresponding to a subtle endothermic event at 196 °C in the DTA curve, associated with the vaporization of the compound. The DTA curve shows an endothermic peak at 128 °C associated with the melting of the compound (Perpétuo *et al.*, 2014).

The TG curves of the QUE–BA systems show three stages of mass loss, corresponding to endothermic and exothermic events in the DTA curve. The first stage, between 150 and 230 °C, is attributed to the vaporization of BA. The last two steps, corresponding to endo and exothermic events in the DTA curve, are attributed to the thermal degradation of QUE. Furthermore, the DTA curves of both systems present two endothermic peaks at 115 and 305 °C, attributed to the melting of the precursors. The thermal behavior of this system is similar to that observed in the TG-DTA curves of the isolated compounds, suggesting that it is only the combination of the thermoanalytical curves. These thermoanalytical results, along with XRPD and FTIR data, suggest that the systems are just physical mixtures.

4. Conclusions

Although all coformers studied in this work have functional groups capable of forming supramolecular synthons with QUE, it was only possible to obtain cocrystals through the mechanochemical method with INA and PA isomers.

The FTIR data suggest that the supramolecular synthons formed in the QUE–INA and QUE–PA cocrystals are different, mainly regarding the presence of the $OH_{(phenol)} \cdots N_{(aromatic\ ring)}$ synthon present in the QUE–INA cocrystal, as already determined by data of crystalline structure and absent in the QUE-PA cocrystal. This is also suggested by the thermoanalytical data, since the thermal stability of the QUE–PA cocrystal is lower than that of the QUE–INA cocrystal, being associated with the loss of free hydroxyl groups (not participating in hydrogen bonds) present in the QUE–PA system.

In addition, the QUE–INA cocrystal, previously reported by the slurry method, could be obtained through a greener method.
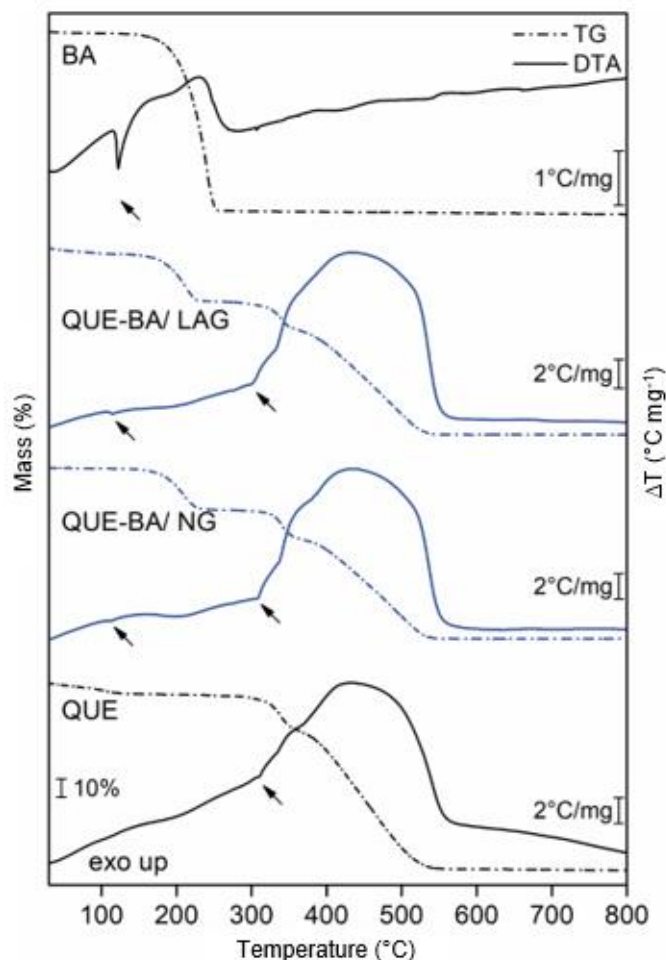

Figure 9. Simultaneous thermogravimetry-differential thermal analysis curves of QUE, BA, and the QUE–BA (1:1) systems (arrow: melting endothermic event).

Authors' contribution

Conceptualization: Souza, F. Z. R.; Almeida, A. C.; Caires, F. J.
Data curation: Souza, F. Z. R.; Almeida, A. C.
Formal Analysis: Souza, F. Z. R.
Funding acquisition: Caires, F. J.
Investigation: Souza, F. Z. R.; Almeida, A. C.; Ferreira, P. O.; Fernandes, R. P.
Methodology: Not applicable
Project administration: Caires, F. J.
Resources: Caires, F. J.
Software: Not applicable
Supervision: Caires, F. J.
Validation: Almeida, A. C.; Ferreira, P. O.
Visualization: Souza, F. Z. R.; Almeida, A. C.; Ferreira, P. O.; Caires, F. J.
Writing – original draft: Souza, F. Z. R.; Almeida, A. C.

References

Aakeröy, C.B.; Forbes, S.; Desper, J. Using Cocrystals To Systematically Modulate Aqueous Solubility and Melting Behavior of an Anticancer Drug. *J. Am. Chem. Soc.* **2009**, *131* (47), 17048–17049. https://doi.org/10.1021/ja907674c

Akalin, E.; Akyuz, S. Vibrational analysis of free and hydrogen bonded complexes of nicotinamide and picolinamide. *Vib. Spectrosc*. **2006**, *42* (2), 333–340. https://doi.org/10.1016/j.vibspec.2006.05.015

Almeida, A. C. de; Ferreira, P. O.; Torquetti, C.; Ekawa, B.; Carvalho, A. C. S.; Santos, E. C. dos; Caires, F. J. Mechanochemical synthesis, characterization and thermal study of new cocrystals of ciprofloxacin with pyrazinoic acid and p-aminobenzoic acid. *J. Therm. Anal. Calorim.* **2020**, *140* (5), 2293–2303. https://doi.org/10.1007/s10973-019-08958-3

Borghetti, G. S.; Carini, J. P.; Honorato, S. B.; Ayala, A. P.; Moreira, J. C. F.; Bassani, V. L. Physicochemical properties and thermal stability of quercetin hydrates in the solid state. *Thermochim. Acta*. **2012**, *539*, 109–114. https://doi.org/10.1016/j.tca.2012.04.015

Costa, E. M. da; Barbosa Filho, J. M.; Nascimento, T. G. do; Macêdo, R. O. Thermal characterization of the quercetin and rutin flavonoids. *Thermochim. Acta*. **2002**, *392–393*, 79–84. https://doi.org/10.1016/S0040-6031(02)00087-4

Dubey, R.; Desiraju, G. R. Combinatorial selection of molecular conformations and supramolecular synthons in quercetin cocrystal landscapes: a route to ternary solids. *IUCrJ*. **2015**, *2*(Part 4), 402–408. https://doi.org/10.1107/S2052252515009884

Évora, A. O. L.; Castro, R. A. E.; Maria, T. M. R.; Rosado, M. T. S.; Silva, M. R.; Canotilho, J.; Eusébio, M. E. S. Resolved structures of two picolinamide polymorphs. Investigation of the dimorphic system behaviour under conditions relevant to co-crystal synthesis. *CrystEngComm*. **2012**, *14* (24), 8649–8657. https://doi.org/10.1039/c2ce26244d

Friščić, T.; Childs, S. L.; Rizvi, S. A. A.; Jones, W. The role of solvent in mechanochemical and sonochemical cocrystal formation: a solubility-based approach for predicting cocrystallisation outcome. *CrystEngComm*. **2009**, *11* (3), 418–426. https://doi.org/10.1039/B815174A

Holanda, B. B. C.; Alarcon, R. T.; Gaglieri, C.; Souza, A. R. de; Castro, R. A. E.; Rosa, P. C. P.; Tangerino, D. J. A.; Bannach, G. Thermal studies, degradation kinetic, equilibrium solubility, DFT, MIR, and XRPD analyses of a new cocrystal of gemfibrozil and isonicotinamide. *J. Therm. Anal. Calorim*. **2019**, *136* (5), 2049–2062. https://doi.org/10.1007/s10973-018-7873-8

Karagianni, A.; Malamatari, M.; Kachrimanis, K. Pharmaceutical Cocrystals: New Solid Phase Modification Approaches for the Formulation of APIs. *Pharmaceutics*. **2018**, *10* (1), 18. https://doi.org/10.3390/pharmaceutics10010018

Karimi-Jafari, M.; Padrela, L.; Walker, G. M.; Croker, D. M. Creating Cocrystals: A Review of Pharmaceutical Cocrystal Preparation Routes and Applications. *Cryst. Growth Des*. **2018**, *18* (10), 6370–6387. https://doi.org/10.1021/acs.cgd.8b00933

Kavanagh, O. N.; Croker, D. M.; Walker, G. M.; Zaworotko, M. J. Pharmaceutical cocrystals: from serendipity to design to application. *Drug Discov. Today*. **2019**, *24* (3), 796–804. https://doi.org/10.1016/j.drudis.2018.11.023

Madaan, K.; Lather, V.; Pandita, D. Evaluation of polyamidoamine dendrimers as potential carriers for quercetin, a versatile flavonoid. *Drug Deliv*. **2016**, *23* (1), 254–262. https://doi.org/10.3109/10717544.2014.910564

Nguyen, T. T.; Jeong, J.-H. Development of a single-jet electrospray method for producing quercetin-loaded poly (lactic-co-glycolic acid) microspheres with prolonged-

release patterns. *J. Drug Deliv. Sci. Technol*. **2018**, *47*, 268–274. https://doi.org/10.1016/j.jddst.2018.07.005

Panzade, P.; Shendarkar, G.; Shaikh, S.; Rathi, P. B. Pharmaceutical Cocrystal of Piroxicam: Design, Formulation and Evaluation. *Adv. Pharm. Bull*. **2017**, *7* (3), 399–408. https://doi.org/10.15171/apb.2017.048

Patel, R. D.; Raval, M. K.; Bagathariya, A. A.; Sheth, N. R. Functionality improvement of Nimesulide by eutectic formation with nicotinamide: Exploration using temperature-composition phase diagram. *Adv. Powder Technol*. **2019**, *30* (5), 961–973. https://doi.org/10.1016/j.apt.2019.02.010

Perpétuo, G. L.; Gálico, D. A.; Guerra, R. B.; Moreira, R.; Chierice, G. O.; Bannach, G. Thermal, spectroscopic and DFT studies of solid benzamide. *Braz. J. Therm. Anal.* **2014**, *3* (1–2), 5–10. https://doi.org/10.18362/bjta.v3i1-2.23

Qiao, N.; Li, M.; Schlindwein, W.; Malek, N.; Davies, A.; Trappitt, G. Pharmaceutical cocrystals: An overview. *Int. J. Pharm.* **2011**, *419* (1–2), 1–11. https://doi.org/10.1016/j.ijpharm.2011.07.037

Rajput, L.; Sanphui, P.; Desiraju, G. R. New Solid Forms of the Anti-HIV Drug Etravirine: Salts, Cocrystals, and Solubility. *Cryst. Growth Des*. **2013**, *13* (8), 3681–3690. https://doi.org/10.1021/cg4007058

Ramešová, Š.; Sokolová, R.; Degano, I.; Bulíčková, J.; Žabka, J.; Gál, M. On the stability of the bioactive flavonoids quercetin and luteolin under oxygen-free conditions. *Anal. Bioanal. Chem*. **2012**, *402* (2), 975–982. https://doi.org/10.1007/s00216-011-5504-3

Rautenberg, M.; Bhattacharya, B.; Akhmetova, I.; Emmerling, F. Mechanochemical and solution syntheses of two novel cocrystals of orcinol with two N,N′-Dipyridines: Structural diversity with varying ligand flexibility. *J. Mol. Struct*. **2020**, *1217*, 128303. https://doi.org/10.1016/j.molstruc.2020.128303

Ravikumar, N.; Gaddamanugu, G.; Solomon, K. A. Structural, spectroscopic (FT-IR, FT-Raman) and theoretical studies of the 1:1 cocrystal of isoniazid with p-coumaric acid. *J. Mol. Struct*. **2013**, *1033*, 272–279. https://doi.org/10.1016/j.molstruc.2012.10.029

Refat, M. S.; Hamza, R. Z.; Adam, A. M. A.; Saad, H. A.; Gobouri, A. A.; Al-Harbi, F. S.; Al-Salmi, F. A.; Altalhi, T.; El-Megharbel, S. M. Quercetin/Zinc complex and stem cells: A new drug therapy to ameliorate glycometabolic control and pulmonary dysfunction in diabetes mellitus: Structural characterization and genetic studies. *PLoS One*. **2021**, *16* (3), e0246265. https://doi.org/10.1371/journal.pone.0246265

Sathisaran, I.; Dalvi, S. V. Engineering Cocrystals of Poorly Water-Soluble Drugs to Enhance Dissolution in Aqueous

Medium. *Pharmaceutics*. **2018**, *10* (3), 108. https://doi.org/10.3390/pharmaceutics10030108

Sinha, A. S.; Maguire, A. R.; Lawrence, S. E. Cocrystallization of Nutraceuticals. *Cryst. Growth Des*. **2015**, *15* (2), 984–1009. https://doi.org/10.1021/cg501009c

Smith, A. J.; Kavuru, P.; Wojtas, L.; Zaworotko, M. J.; Shytle, R. D. Cocrystals of Quercetin with Improved Solubility and Oral Bioavailability. *Mol. Pharm*. **2011**, *8* (5), 1867-1876. https://doi.org/10.1021/mp200209j

Su, H.; He, H.; Tian, Y.; Zhao, N.; Sun, F.; Zhang, X.; Jiang, Q.; Zhu, G. Syntheses and characterizations of two curcumin-based cocrystals. *Inorg. Chem. Commun.* **2015**, *55*, 92–95. https://doi.org/10.1016/j.inoche.2015.03.027

Tang, Y.; Nakashima, S.; Saiki, S.; Myoi, Y.; Abe, N.; Kuwazuru, S.; Zhu, B.; Ashida, H.; Murata, Y.; Nakamura, Y. 3,4-Dihydroxyphenylacetic acid is a predominant biologically-active catabolite of quercetin glycosides. *Food Res. Int*. **2016**, *89* (1), 716–723. https://doi.org/10.1016/j.foodres.2016.09.034

Thakuria, R.; Sarma, B. Drug-Drug and Drug-Nutraceutical Cocrystal/Salt as Alternative Medicine for Combination Therapy: A Crystal Engineering Approach. *Crystals*. **2018**, *8* (2), 101. https://doi.org/10.3390/cryst8020101

Varzakas, T.; Zakynthinos, G.; Verpoort, F. Plant Food Residues as a Source of Nutraceuticals and Functional Foods. *Foods*. **2016**, *5* (4), 88. https://doi.org/10.3390/foods5040088

Vasisht, K.; Chadha, K.; Karan, M.; Bhalla, Y.; Jena, A.K.; Chadha, R. Enhancing biopharmaceutical parameters of bioflavonoid quercetin by cocrystallization. *CrystEngComm*. **2016**, *18* (8), 1403–1415. https://doi.org/10.1039/C5CE01899D

Yadav, A. V.; Shete, A. S.; Dabke, A. P.; Kulkarni, P. V.; Sakhare, S.S. Co-crystals: A novel approach to modify physicochemical properties of active pharmaceutical ingredients. *Indian J. Pharm. Sci*. **2009**, *71* (4), 359–370. https://doi.org/10.4103/0250-474X.57283

Yousef, M.A.E.; Vangala, V.R. Pharmaceutical Cocrystals: Molecules, Crystals, Formulations, Medicines. *Cryst. Growth Des*. **2019**, *19* (12), 7420–7438. https://doi.org/10.1021/acs.cgd.8b01898

Yurdakul, Ş.; Ataç, A. Fourier Transform-Infrared Spectroscopic Study of IsonicotinamideMetal(II) Tetracyanonickelate and Halide Complexes. *Spectrosc. Lett.* **2004**, *37* (1), 33–42. https://doi.org/10.1081/SL-120028421